Karlsruher Institut für Technologie

ETP-KA/2019-17

Assembly and qualification procedures of 2S modules and high rate tests of the CMS Binary Chip for the Phase 2 Upgrade of the CMS Outer Tracker

Stefan Maier

Zur Erlangung des akademischen Grades eines
DOKTORS DER NATURWISSENSCHAFTEN
von der KIT-Fakultät für Physik des
Karlsruher Instituts für Technologie (KIT)

genehmigte

Dissertation

von

M.Sc. Stefan Maier
aus Kronau

Tag der mündlichen Prüfung: 13.12.2019

Referent:	Prof. Dr. Ulrich Husemann	Institut für Experimentelle Teilchenphysik
Korreferent:	Prof. Dr. Thomas Müller	Institut für Experimentelle Teilchenphysik

Stefan Maier:
Assembly and qualification procedures
of 2S modules and high rate tests of the
CMS Binary Chip for the Phase 2 Upgrade
of the CMS Outer Tracker
December 2019

Contents

Part I.

Introduction and Basics

1

Introduction

Scientists all over the world work together in many types of particle physics experiments to get a deeper insight in the fundamental components of matter. Some of these experiments are located at powerful accelerators. They investigate the interactions of known particle types or search for new, so far unknown, particles. The most powerful accelerator today is the Large Hadron Collider (LHC) at the European Organization for Nuclear Research (CERN) near Geneva, which accelerates particles in opposite directions to almost the speed of light and collides them within particle detectors. With the signals generated by the resulting fragments traversing the detector, the initial interaction and possible production of particles can be investigated in detail.

The Standard Model describes the known elementary particles and their interactions and was developed during last decades. It is a theory that successfully describes most of the experimental observations but fails to give answers on the origin of gravitation or dark energy and dark matter. Some extensions of the Standard Model, such as Supersymmetry, could resolve several of the open questions. Experiments with large samples of collection data and advanced analysis concepts are inevitable to investigate such theories beyond the Standard Model.

To increase the number of events and therefore the probability to discover physics beyond the Standard Model the LHC will enter a new phase, called the High Luminosity LHC (HL-LHC), in 2026. It is planned to increase the luminosity, a measure of the rate of particle collisions, by a factor of five beyond the LHC's nominal design value. This is achieved by improving several parts of the accelerator chain.

The Compact Muon Solenoid (CMS) experiment is one of the two general purpose detectors at the LHC and contributed to the discovery of the Higgs boson in 2012 [CMS12b] [ATL12]. In preparation for the HL-LHC most of the sub-detectors of CMS undergo major upgrades to cope with the increased luminosity, which results in a higher particle flux through the experiment, demanding higher radiation tolerances and an improved event filtering.

The current silicon tracker of the CMS experiment will reach its end of operation life time after 2023. For the HL-LHC it will be fully replaced with a new, enhanced version within the Phase 2 Upgrade of the CMS detector. The new tracker is divided in a high resolution pixel detector in the inner region and the Outer Tracker consisting of two module types. For the first time, the Outer Tracker will provide tracking information to the Level 1 trigger decision using p_T-trigger modules, with which it is possible to keep the trigger rates at a maximum of 750 kHz [CMS17c].

The new p_T-trigger module concept uses two closely spaced silicon sensors to perform an on-module filtering of charged particles regarding their transverse momentum, exploiting the bend of their trajectory in the magnetic field. High-p_T particles have a smaller bend than low-p_T particles and thus their signals in the two silicon sensors will be almost superimposed, which is detected with a dedicated logic on the readout chips. The hit information of high-p_T particles is sent to the detector back-end at 40 MHz.

The two module types are the PS module, which uses one silicon sensor with $1.5\,\mathrm{mm}\times 100\,\mu\mathrm{m}$ sized pixels and one sensor segmented in strips of 2.5 cm, and the 2S module, which is made of two sensors segmented in strips of 5 cm. The 2S modules are located in the outermost region of the future CMS tracker. The production of about 7000 2S modules is spread over several institutes all around the world and follows a strict assembly procedure using precise mechanical tools. The Institute of Experimental Particle Physics (ETP) at the Karlsruhe Institute of Technology (KIT) pledged to build 2000 2S modules by 2023. The on-module $\mathrm{p_T}$-discrimination and the operation bias voltage of the silicon sensors of up to 800 V puts high requirements on the mechanical assembly precision of the modules. In addition to this, the assembly has to be reliable and of high quality to cope with the harsh radiation levels of up to $1 \times 10^{15}\,\frac{\mathrm{n_{eq}}}{\mathrm{cm}^2}$ and an operation temperature of down to $-35\,°\mathrm{C}$. Tests after each assembly step are mandatory to keep the module quality high and the failure rate low. Therefore, the production centres have to develop reliable assembly and qualification procedures in the ongoing prototyping phase for the upcoming large scale module production.

In the scope of this thesis several assembly steps and qualification procedures of 2S modules were developed. They are discussed in detail in Chapter 4 after introducing the LHC, CMS and their upgrades in the chapters 2 and 3. Several test stations were developed, programmed and commissioned to guarantee a high assembly quality. This includes test stations that verify the functionality of the sensors and final modules as well as their assembly precision. In further investigations the radiation hardness of the wire-bond encapsulation material, which is applied on the readout wire-bonds for protection, was tested. The ETP was the first production site to build a functional 2S module outside the pilot centre CERN in 2018. A second module followed in 2019. The assembly and qualification results of those two functional 2S module prototypes built at ETP are summarized in Chapter 4.

The 2S modules in the future CMS Outer Tracker have to cope with track densities of up to $15\,\mathrm{MHz/cm^2}$ resulting in a maximum occupancy, the probability of a readout channel to detect a hit, of about 1 %. In addition to this, the expected trigger rate can reach up to 750 kHz. Usual tests to characterize the operability of silicon detectors involve beam lines on accelerators or radioactive sources, which cannot deliver track densities and trigger rates comparable to the environment in the future CMS Outer Tracker.

In the scope of this thesis a system was developed to test the high rate operability of the 2S module readout chain. Chapter 5 introduces the KARATE (KArlsruher high RAte TEst) system. With a combination of LEDs and silicon photodiodes charge patterns with varying pulse heights and hit rates are injected into the front-end of the 2S module readout chip, called CMS Binary Chip, to emulate silicon sensor signals with the expected hit occupancy and trigger rate. Several scenarios validate the functionality of the CMS Binary Chip at high hit and trigger rates.

The track trigger concept is a key element in the design of the future CMS experiment. With the track input to the level 1 trigger decision by filtering the tracks of high-$\mathrm{p_T}$ particles on the level of the modules, it will be possible to keep the readout data rate at a reasonable value. This will help in the search for new physics beyond the standard model and to get new insights into the fundamental components of matter.

2

The Large Hadron Collider and the CMS experiment

The Large Hadron Collider (LHC) is the most powerful particle accelerator ever built. It is located at the European Organization for Nuclear Research (CERN) near Geneva and accelerates protons within two beam pipes in counter-rotating directions up to an energy of 6.5 TeV. The beams are brought to collision at four interaction points, one for each main experiment: A Toroidal LHC ApparatuS (ATLAS), LHC beauty (LHCb), A Large Ion Collider Experiment (ALICE) and the Compact Muon Solenoid (CMS). This chapter describes the LHC together with CMS in more detail [CER17].

2.1. The Large Hadron Collider (LHC)

The LHC is 26.7 km long and designed to generate proton-proton collisions with a center-of-mass energy of 14 TeV. Figure 2.1 shows a schematic of the accelerator complex at CERN. The magnetic dipoles of an accelerator have an limited operating range. Therefore, the LHC is part of a large accelerator chain in which the energy of the hadrons is successively increased to 450 GeV before they are injected into the LHC and finally brought to an energy of 6.5 TeV. Within the LHC the hadrons are kept on a circular track by 1232 superconducting niobium titanium dipole magnets with a field strength of up to 8.3 T, cooled with liquid helium at a temperature of 1.9 K. Additional quadrupol, sextupol and octupol magnets are deployed for beam focusing [EB08].

The beam energy in synchrotrons is increased using cavity resonators. Depending on the phase particles arriving earlier in the cavities with respect to the alternating electric field are decelerated, later ones are accelerated. This divides the structure of the beam in particle packets called bunches. To increase the particles energy the magnetic field in the dipoles in most of the accelerators in the chain is ramped up narrowing the circular track. Having the matching phase setting, the bunches enter the cavities earlier and thus pick up energy. As soon as the maximum magnetic field strength of the current accelerator in the chain is achieved the beam is passed to the next stage until they reach their highest energy in the LHC.

When fully filled, the LHC beam consists of 2808 bunches and each bunch contains up to 1.2×10^{11} protons. Once the beams are fully accelerated, kicker magnets right in front of the experiments deflect the beams so that they cross each other inside the detectors. For a high particle density within the bunch and therefore a higher probability of particle interactions at the interaction points it is crucial to minimize the bunch cross section A with focusing magnets before the beam enters the detectors. This increases the number of simultaneous interactions, called pile-up, within one bunch crossing. The LHC generates collisions with a mean pile-up of about 40. While the studies of rare processes profits from larger datasets it is very challenging for the experiments to distinguish the simultaneous collision events from each other. One of the most important characteristics of particle colliders is the instantaneous luminosity which is

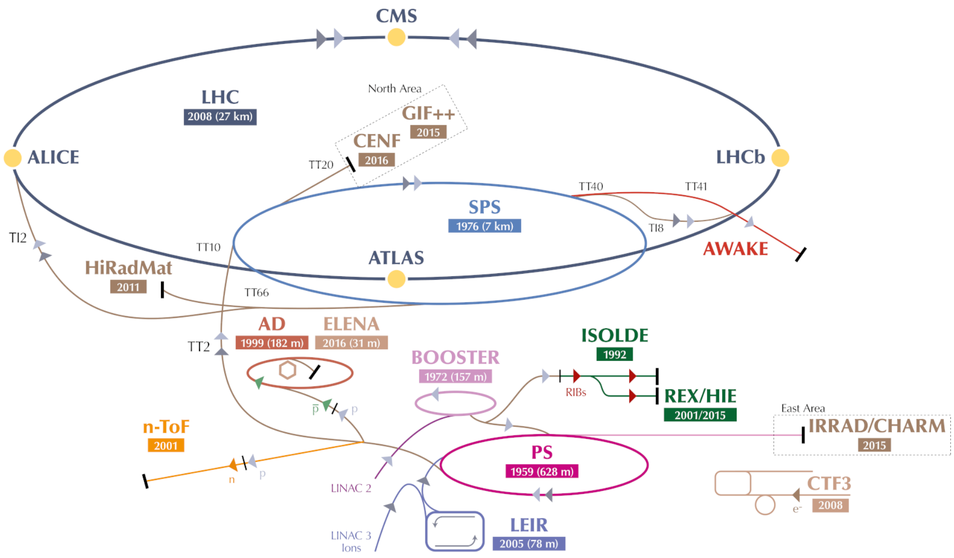

Figure 2.1.: The CERN accelerator complex. After starting at the LINAC 2 accelerator protons are injected into the Proton Synchrotron Booster (Booster) followed by the Proton Synchrotron (PS). With an energy of 25 GeV they are injected into the Super Proton Synchrotron (SPS) where they reach the LHC injection energy of 450 GeV. The LHC then increases the proton energy to 6.5TeV [Mob16] [EB08].

given by

$$\mathcal{L} = \frac{n \cdot N_1 \cdot N_2 \cdot f}{A}, \tag{2.1}$$

where n is the number of bunches per beam, N_1 and N_2 are the number of particles in them, f is their revolution frequency, and A is their geometric cross section. It is the proportionality factor between the number of events per second dN/dt and the cross section σ_e for any given process:

$$\frac{dN}{dt} = \mathcal{L} \cdot \sigma_e. \tag{2.2}$$

The LHC was designed to run at a luminosity of $\mathcal{L} = 1 \times 10^{34}\,\mathrm{cm}^{-2}\mathrm{s}^{-1}$ and has exceeded this value by a factor of 2 since May 2018 due to improvements in the beam and injection lines [HM06] [CER18]. The increased number of events for a certain process in a finite time explains the significance of the luminosity for the experiments and why the machine engineers are constantly trying to keep it as high as possible. The integrated luminosity

$$\mathcal{L}_{\text{int}} = \int_0^T \mathcal{L}(t)\,\mathrm{d}t \tag{2.3}$$

gives the number of interactions the accelerator is capable to produce in a given time. Its unit is given in inverse femtobarns fb^{-1}. By now the LHC has produced almost $200\,\mathrm{fb}^{-1}$ of data during the last 9 years [HM06] [CMS19c].

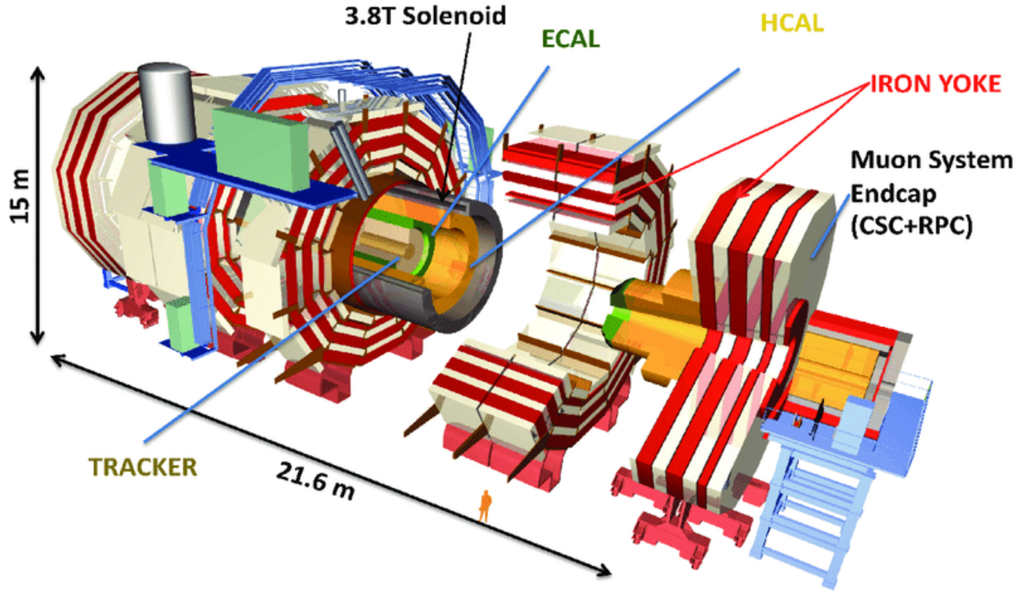

Figure 2.2.: Illustration of the Compact Muon Solenoid (CMS) experiment with its sub-detectors. The silicon tracker divided in a pixel and strip detector and is surrounded by the electromagnetic and hadronic calorimeters. The superconducting niobium-titanium solenoid is located between the hadronic calorimeter and the muon system on the outer part, which is embedded in the iron return yoke [Axe19].

2.2. The Compact Muon Solenoid (CMS) experiment

The CMS experiment was completed in 2008 and contributed, together with the ATLAS experiment, to the discovery of the Higgs boson in 2012. More than 5000 people related to almost 230 institutes in over 50 countries participate in the experiment. This large number of people is needed for the development, construction, operation, maintenance and future improvements of CMS, such as the Phase 2 Upgrade as introduced in Chapter 3. The enormous amount of data generated by the experiment is analysed by scientists all around the world [CMS19b].

As most high energy physics detectors CMS is built in a cylindrical shape with a barrel and two end-cap regions, which is also shown in Figure 2.2. It is 21 m long, 14 m wide and weighs about 14 000 t. To meet its physics goals the detector design and all sub-detectors have to meet several requirements for best possible event reconstruction. This includes a solid angle coverage of nearly 4π, a high time resolution of the front-end electronics and a sophisticated trigger concept to reduce the data output to an offline data storage rate of up to 1 kHz. The trigger system is based on information coming from both calorimeters and the muon system. The usage of one of the most powerful solenoid magnets in the world is reflected in CMS's name as well as the good muon detection performance. Most of the sub-detectors are placed very compactly within this magnet, which explains the first letter of the experiment name [CMS08].

2.2.1. Sub-detectors

Only the combination of several sub-detectors ensures CMS to be a multi purpose detector. Each sub-detector is a sophisticated system on its own, fulfilling unique tasks, while the requirements and therefore the technologies used, differ.

Silicon Tracker Detector

With almost 200 m^2 of silicon surface the tracker of the CMS experiment is the largest silicon tracker ever built [Kar+97]. It is divided in an inner detector based on modules made from pixel sensors and an outer system assembled with modules made from strip sensors. Due to the magnetic field of 3.8 T generated by the solenoid, charged particles cross the silicon tracker on a helix-shaped trajectory. Reconstructing the bending direction and radius perpendicular to the magnetic field lines provides charge and transverse momentum of the particles.

Due to extensive radiation damage and the increase of instantaneous luminosity of LHC the initial pixel detector was already replaced by an enhanced successor in the scope of the Phase 1 Upgrade in beginning of 2017. Instead of three, the new pixel detector consists of four layers in the barrel region and three layers instead of two in the end-caps. Overall there are nearly 1900 modules deployed. Within each layer the modules are mounted on a light-weight carbon fibre structure which also guides the new CO_2 cooling system operating at $-20\,^\circ$ C. The inner-most layer in the barrel is placed as close as possible to the beam pipe, resulting in a minimal distance to the interaction point of about 4 cm. To cope with the high particle flux the silicon sensors are segmented in 67 000 pixels with a size of $100\,\mu\text{m} \times 150\,\mu\text{m}$ each. The hit data is amplified and processed by 16 readout chips connected via bump bonds to the sensors. Each chip is wire-bonded to a flexible printed circuit glued on the sensor-chip package, whose electronics gathers the hit information of all chips and sends them out once the module is triggered [CMS12a].

Since the need for high granularity becomes less important with increasing distance to the interaction point the outer part of the silicon tracker is made of strip sensors. It contains 15200 modules having different designs depending on their location. Each module is made of a mechanical support, a set of sensors and the readout electronics. Wire-bonds connect the silicon sensors via pitch adapters to the readout chips. After processing the data it is send out via optical fibres [CMS08].

With its overall 124 million readout channels in the pixel and 10 million in the strip section, the CMS tracker is able to reconstruct vertices of charged particles with a precision of 10 to 12 µm in the longitudinal direction parallel to the beam axis [CMS12a].

Electromagnetic Calorimenter (ECAL)

To measure the energy of electromagnetically interacting particles such as photons, electrons and positrons the silicon tracker is completely surrounded by almost 76 000 lead-tungstate crystals ($PbWO_4$) - called electromagnetic calorimeter (ECAL) - which weigh about 90 t. Lead-tungstate is transparent and has a high density of $\rho = 8.28\,\text{g}\,\text{cm}^{-3}$, which results in a radiation length of only 0.89 cm and a Molière radius, the transverse dimension of an electromagnetic shower, of $R_M = 2.1\,\text{cm}$. Therefore, lead-tungstate is an ideal substrate to absorb and transform the particles energy via scintillation in detectable light. Each crystal is about 23 cm long resulting in an overall radiation length of the ECAL of $26\,X_0$. The light is detected by avalanche photo diodes and vacuum phototriodes especially designed to operate in a high magnetic field environment. More information about the ECAL can be found in [Col97]

Hadronic Calorimeter (HCAL)

The ECAL is encased by the hadronic calorimeter (HCAL). The HCAL absorbs and measures the energy of hadronically interacting particles. Within brass absorber plates the hadrons generate showers. The electromagnetic part of these showers scales with the initial hadron energy and generates light in alternating deployed plastic scintillators read out by photodiodes. This combination, called sampling calorimeter, ensures that almost all hadronic particles are stopped inside the HCAL and do not penetrate the solenoid or muon system. The nuclear interaction length is $\lambda_I = 9$. Further information about the HCAL is given in [CMS97a]

Solenoid Magnet and Iron Return Yoke

A key element for particle identification within CMS is the magnetic field enabling the determination of sign and momentum of traversing charged particles. With a field strength of 3.8 T and a diameter of 6 m the CMS magnet system is one of the most powerful solenoids ever built. It stores an energy of about 2.6 GJ while a current of 18 kA flows in four layers of superconducting niobium-titanium which is cooled with liquid helium down to 4.2 K. A 12 500 t iron yoke guides the magnetic field lines on the outer parts of the solenoid [CMS08].

Muon Chambers

Since high-energy muons can only be absorbed reliably within kilometres of matter, they are not stopped inside CMS. Therefore, the muon system is located on the outer regions of the experiment embedded within the iron return yoke, which is used as absorber material for all other particles than muons and neutrinos. Three different gaseous-based detector technologies are used to reconstruct the trajectory of traversing muons: Cathode Strip Chambers, Drift Tubes and Resistive Plate Chambers. Further details of the muon system can be found in [CMS97b].

2.2.2. Particle Identification in CMS

With its various sub-detectors CMS can distinguish very well between most of the generated particles types emerging from an interaction at the interaction point.

Figure 2.3 shows the principle of the particle identification at CMS. Photons do not carry charge but interact electromagnetically and therefore they pass the tracker unnoticed and are stopped in the ECAL by producing an electro-magnetic shower. If a photon creates a pair of electron and positron a secondary vertex is visible inside the tracking volume. Neutral hadrons are also solely detected by their shower generation in the HCAL. Charged hadrons also pass the ECAL largely undetected and are stopped in the HCAL but leave a measurable trajectory in the tracker. The particle flow algorithm combines the information across multiple sub-detectors to optimally reconstruct all physics objects. If a jet traverses the detector the energy information of its electromagnetic component can be linked to the trajectories measured in the tracker, improving the energy measurement. Electrons or positrons interact with the tracker and can also produce Bremsstrahlung which has to be taken into account once their energy is measured in the ECAL. Solely muons pass all sub-detectors and generate signals in the tracker and in the muon system before they leave CMS. As neutrinos hardly interact with matter CMS does not measure them directly. By adding up the transverse momenta of all particles in an event a deficit is calculated which is attributed to neutrinos or other undetected weakly interacting particles [CMS17a].

2.2.3. Trigger Concept of CMS

With nearly 140 million readout channels each event generates approximately 17 MB of raw data. Running at a bunch crossing frequency of 40 MHz CMS therefore produces theoretically nearly 700 TB/s. Because it is not possible to record and store this amount of data in real time a data reduction with zero suppression and dedicated readout procedures called trigger rules is applied. The trigger rules are implemented in a two staged algorithm.

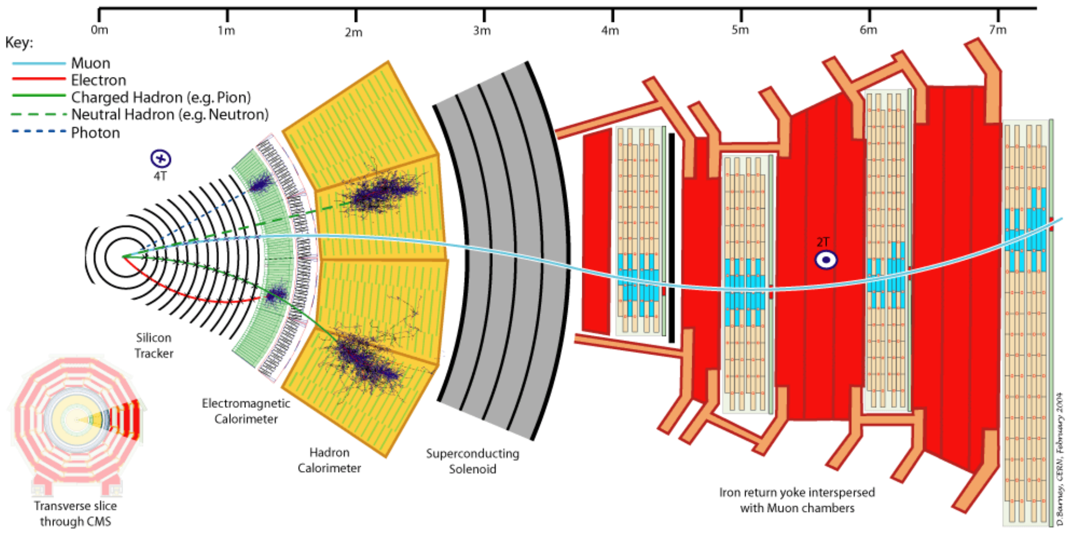

Figure 2.3.: Slice of the CMS detector. Depending on their type most particles are detected in one or more sub-detectors [Dav16].

The first stage is called Level 1 (L1) trigger and combines information from the calorimeters and muon system. Within 3.4 µs it decides whether a trigger signal is sent to the front-end readout electronics. For this time interval the readout ASICs [1] of all channels in each sub-detector have to buffer the events to avoid data loss. The L1 trigger is implemented in FPGAs[2] and additional custom made ASICs. This preselection reduces the readout rate from 40 MHz down to 100 kHz. The triggered events are passed to the second stage, which is a software based selection algorithm. It is called High Level Trigger (HLT) and has access to the information of all sub-detectors. The trigger rules can be adjusted manually to certain physics objects. The HLT further reduces the readout rate to 1 kHz which is acceptable to store the data on disk [CMS17b].

---

[1] Application Specific Integrated Circuits

[2] Field Programmable Gate Arrays

Part II.

Main

3

The Phase 2 Upgrade of the CMS Outer Tracker

Due to constant improvements on the accelerator chain during the last 10 years LHC reached a center of mass energy of $\sqrt{s} = 13\,\text{TeV}$ and has achieved an instantaneous luminosity of $2 \times 10^{34}\,\text{cm}^{-2}\text{s}^{-1}$, which is twice as high as its design value. The mechanical modifications take place in Extended Year End Technical Stops (EYETS) or Long Shutdowns (LS). As shown in Figure 3.1 after LS2 during Run 3 the LHC will operate at its design center of mass energy of 14 TeV and a further increased luminosity of $2.5 \times 10^{34}\,\text{cm}^{-2}\text{s}^{-1}$. After Run 3 the LHC will shut down and enter LS3 to prepare for the High Luminosity runs [CER19].

3.1. The High Luminosity LHC Project

The search for physics beyond the standard model relies on high statistics to make very rare events visible. An option to increase statistics is to prolongate an experiment's runtime, which is in many cases unfeasible. Therefore, the LHC performance will be increased with major improvements and the accelerator complex enters a new phase called High Luminosity LHC (HL-LHC) in 2026.

The High Luminosity project will improve various magnets on the beam line as well as the beam injection for a better beam focusing. A crucial improvement is to use crab cavities in front of the experiments. As given in Equation (2.1) the instantaneous luminosity and thus the performance of the accelerator is linked to the cross section of the interacting bunches. Bunches entering a detector are deflected by kicker magnets to point them towards each other. Since they are elliptically shaped clouds their effective cross section is decreased due to the deflection angle while penetrating each other. The crab cavities installed in front of the detectors apply a shape changing torque on each bunch in such a way that the effective cross section at the interaction point is maximized.

As shown in Figure 3.1 the HL-LHC will start operating in 2026 after the two year long LS3 in which most of the systems will be improved. The HL-LHC will run at an instantaneous luminosity of $5 \times 10^{34}\,\text{cm}^{-2}\text{s}^{-1}$, which is five times higher compared to the initial LHC design value. CERN decided to run the HL-LHC at least until 2037 yielding in approximately $3000\,\text{fb}^{-1}$ of data, which would take about 60 years to accumulate at nominal LHC conditions. The enormous increase of particle interactions puts high demands on the experiments located at the LHC and thus they need to be upgraded [Apo+17].

3.2. The Phase 2 Upgrade of the CMS Tracker

This section is based on the Technical Design Report (TDR) of the Phase 2 Upgrade of the CMS tracker [CMS18].

After ten years of operation the present tracker, including the already upgraded pixel detector, reaches the end of its life time due to radiation damage. In addition to this the tracker does

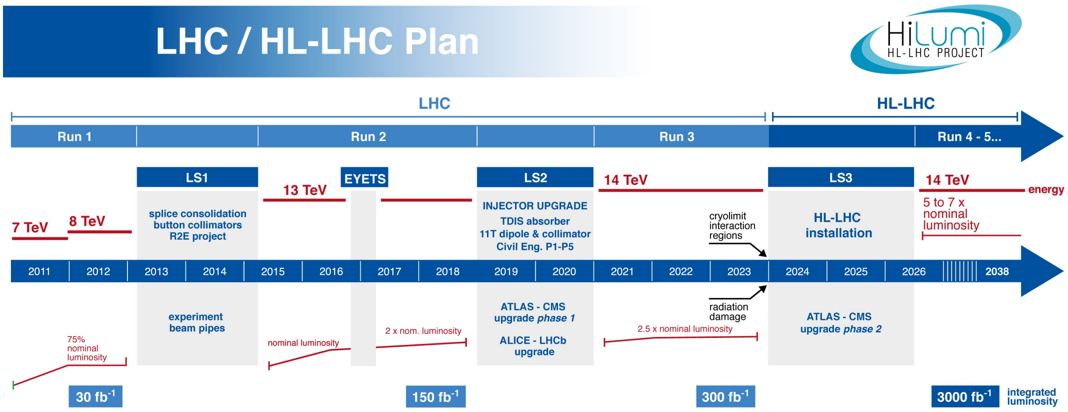

Figure 3.1.: The High Luminosity LHC project schedule. To enter the High Luminostiy phase the accelerator complex and the experiments will be upgraded during LS3 to cope with the increased instantaneous luminosity from 2026 [CER19].

not cope with the demanding challenges of the HL-LHC environment and lacks essential functionalities. Therefore, it was decided to completely replace the tracker within LS3.

With the increased instantaneous luminosity of the HL-LHC the CMS experiment will record about $3000\,\mathrm{fb}^{-1}$ of data. In an ultimate scenario this number will be boosted to up to $4000\,\mathrm{fb}^{-1}$. The high interaction rate results in a higher track density and thus radiation damage within the experiment. To cope with the track density it is necessary to increase the granularity of the tracker to keep the occupancy, the probability of a channel to be hit by a crossing particle per bunch crossing, below a few percent in the Outer Tracker and permille in the Inner Tracker. This is an important requirement for the track reconstruction because a low occupancy yields in less combinatorics in the track finding.

The current selection algorithms of the CMS trigger will become less inefficient with increasing pile-up. Therefore, a new key element in the phase 2 CMS detector is the contribution of tracking information to the first trigger stage, called Level 1 (L1), keeping the readout rate below an average of 750 kHz [CMS17c]. Therefore, the modules deployed in the Outer Tracker are able to discriminate particles based on their transverse momentum, because high p_T particles hint at events of interest and it is not possible to readout all tracks at 40 MHz. With this, about 98 % of the tracks are suppressed, and only the filtered, high p_T part is sent out to the back-end. A special design was introduced to be able to read out two closely spaced silicon sensors with one ASIC. The information of high-p_T particles is sent to an FPGA based track finder at a rate of 40 MHz, which further processes the data until it is passed to the L1 trigger stage. The decision has to be taken within 12.5 µs, which requires the readout ASICs in the Outer Tracker to store data of 512 bunch crossings. More details about these so called p_T trigger modules are given in Section 3.3 [Agg+17].

3.2.1. Tracker Layout

The layout and composition of the new tracker of CMS has been optimized for the track trigger concept and is shown in Figure 3.2. The pixel detector is elongated to the very end of the tracker volume. By moving it very close to the beam pipe the acceptance is increased from $|\eta| < 2.5$ to $|\eta| < 4$, where η is the pseudorapidity defined by

$$\eta = -\ln\left[\tan\left(\frac{\theta}{2}\right)\right], \tag{3.1}$$

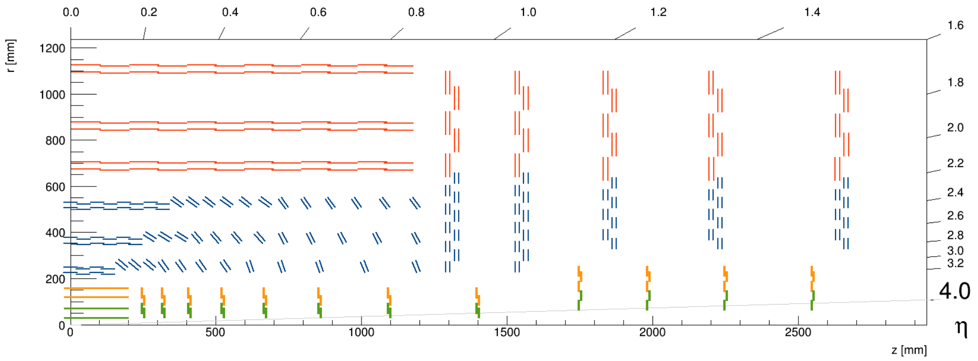

Figure 3.2.: Schematic of one quarter of the Phase 2 tracker. The pixel detector made of modules with two (green lines) and four (orange lines) readout chips per module. Compared to the current pixel detector it has an increased granularity and is elongated to the end of the tracker volume achieving a coverage of up to $|\eta| = 4$. Double blue lines represent PS modules deployed in a barrel and endcap. On the outer region the 2S modules (double red lines) are located in the barrel and on the endcaps [CMS18].

in which θ is the angle between the particle three-momentum $\mathbf{p}$ and the positive direction of the beam axis. The pixel detector will instrument a silicon surface of almost $5\,\mathrm{m}^2$ with about 3.8 billion readout channels. The Outer Tracker consists of almost $200\,\mathrm{m}^2$ of silicon with almost 200 million readout channels.

The pixel detector consists of two types of modules. Each module is read out by either two or four readout ASICs, whereas the first module type is located on the most inner regions. Each sensor is segmented in $50\,\mu\mathrm{m} \times 50\,\mu\mathrm{m}$ or $25\,\mu\mathrm{m} \times 100\,\mu\mathrm{m}$ sized pixels. The decision about the pixel's dimensions is still pending. The modules are placed on four layers in the barrel region and twelve discs on each side in the forward region.

The Outer Tracker is composed of modules of two different types. The PS modules are located in the inner part of the Outer Tracker. They have a higher granularity compared to the 2S modules which are located on the outer regions. Further details on these modules are given in Section 3.3 and Chapter 4.

Geometrically the Outer Tracker is divided in three regions. The tracker barrel with PS modules (TBPS), the tracker barrel with 2S modules (TB2S) and the tracker-end-cap double discs (TEDD). The barrel section consists of six layers while the end-caps will have four discs each. To keep the material budget as low as possible the tracker is mostly built of light-weight carbon fibre structures. These structures serve as the mechanical fixture for all the modules and the CO_2 cooling which is routed through them. The tracker is going to be operated with a coolant temperature of $-33\,^{\circ}\mathrm{C}$, which affirms the usage of carbon fibre material due to their low coefficient of thermal expansion (CTE). A part of the TBPS is tilted. This minimizes the number of modules and thus material and readout data as well as inefficiencies in detection high-p_{T} particles. With the tilted geometry the number of PS modules is reduced from about 7000 to 5600 [Con+15] [CMS18].

3.2.2. Radiation Environment

The HL-LHC operation requires high radiation hardness of the components developed. The radiation damage within the detector directly scales with the luminosity delivered by the HL-LHC. As shown in Figure 3.3 the tracker will have to sustain severe radiation levels of

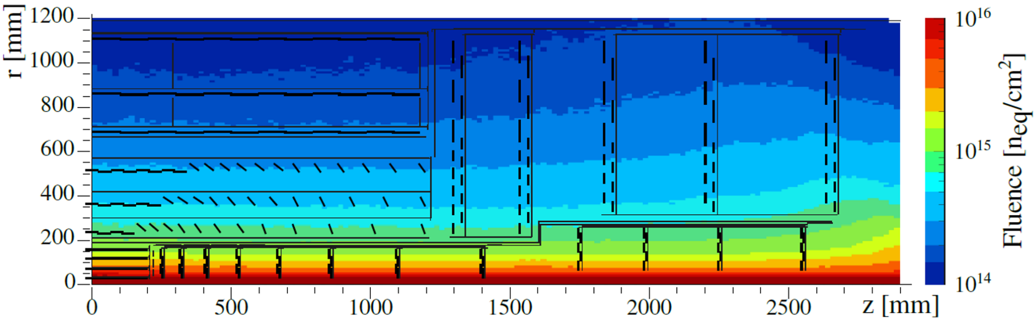

Figure 3.3.: Fluences of the phase 2 tracker. The radiation levels within the pixel detector reach $1 \times 10^{16}\,\frac{n_{eq}}{cm^2}$. This requires a replacement of parts of the pixel detector in a following LS. The PS modules have to be radiation tolerant to up to $1 \times 10^{15}\,\frac{n_{eq}}{cm^2}$, while the 2S modules will only sustain $3 \times 10^{14}\,\frac{n_{eq}}{cm^2}$ [CMS18].

up to $\Phi_{eq} = 1 \times 10^{16}\,\frac{n_{eq}}{cm^2}$[1] during its life time of about 10 years collecting $3000\,fb^{-1}$ of data. Because the track density increases towards the interaction point, the pixel detector will suffer most under irradiation. Therefore, it is planned to replace parts of the pixel detector again in a following LS similar to the replacement during the Phase 1 Upgrade in 2017.

The Outer Tracker will stay in the experiment until the very end. The PS module region in the inner parts of the Outer Tracker will have to sustain a fluence of $1 \times 10^{15}\,\frac{n_{eq}}{cm^2}$ equivalent to a total ionizing dose of 5×10^5 Gy. This puts high requirements on the selection of the silicon sensor material and readout ASICs as well as the mechanical components and glues used for construction. Because both module types use identical components the radiation tests are referring to the worst case scenario present for the PS modules located on the inner-most layer.

For a higher radiation hardness of the silicon sensors compared to the current tracker, the chosen silicon sensors have an n-doped implant in a p-doped bulk (n-in-p) instead of p-in-n. This material has become affordable within the last decade and has the advantage that the electron readout yields a higher signal after the expected fluence [Ada+17] [CMS18].

3.3. p_T Trigger Modules

The new p_T trigger module concept introduced in the Phase 2 Upgrade of the Outer Tracker uses two closely spaced silicon sensors. Adjacent channels on both sensors are read out with the same ASIC. As shown in Figure 3.4, this enables an on-module transverse momentum discrimination of the passing particles. Particles with a high transverse momentum pass both sensor layers in a straight line since their trajectories are less bent in the magnetic field compared to charged particles with low transverse momentum. The two silicon layers are treated as a seed and a correlation layer, while the seed layers faces towards the interaction point. The position of the seed cluster defines an adjustable window of channels on the correlation layer. If the corresponding correlation cluster lies within this window the chip logic defines a so called stub, which is then further processed and sent to the back-end data processing system of the tracker [PH10].

The two module types are shown in Figure 3.5. The major difference between the PS and 2S module is their granularity. While the 2S module consists of two silicon strip sensors with 4064 readout channels instrumenting about 10 cm × 10 cm, the PS module exceeds this ratio by far by combining a strip sensor with a macro-pixel sensor having 32128 channels instrumenting about 5 cm × 10 cm. The usage of pixel sensors in the Outer Tracker allows to reconstruct the

---

[1] Neutron equivalent per cm^2: The equivalent damage caused by 1 MeV neutrons

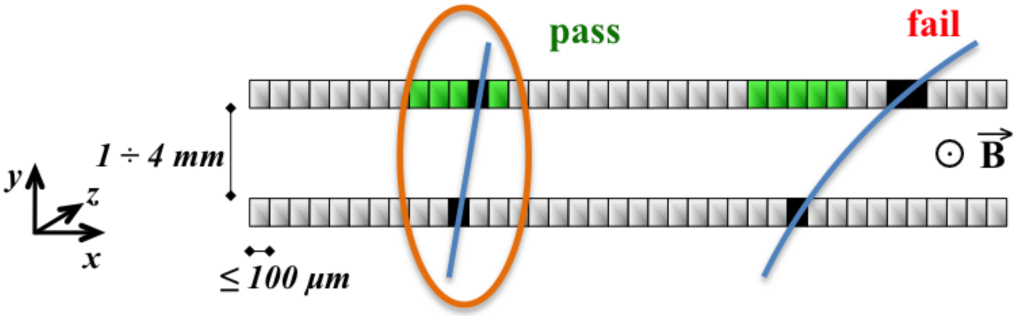

Figure 3.4.: Concept of p_T -trigger modules. The position of the cluster signal in the lower seed layer defines a window in the upper correlation layer. Particles crossing the correlation layer within this window are detected as stubs in the front-end logic. A stub contains the information of its signal position in the seed layer and its bend value, which corresponds to the offset between the seed position and the signal position of the correlation layer [CMS18].

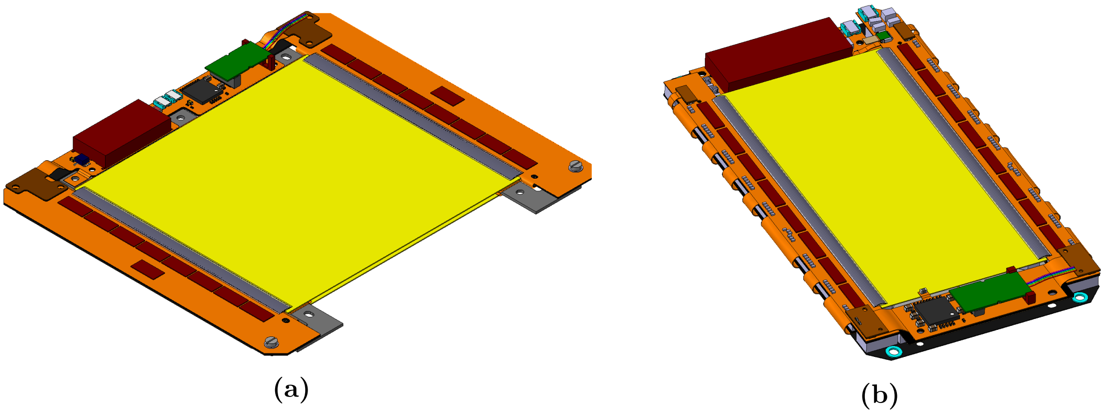
(a)
(b)

Figure 3.5.: The 2S module (a) and PS module (b) deployed in the CMS phase 2 Outer Tracker. The PS module, consisting of one strip and one macro-pixel sensor, is located on the inner regions of the Outer Tracker while the larger 2S modules, made of two silicon strip sensors, are used in the outer layers [CMS18].

interaction point of the trajectory on L1 trigger basis. Both modules will come with different sensor spacings depending on their location inside the tracker. Towards the inner part of the tracker the particles cross the modules with a lower incidence angle than in the outer regions. To still be able to distinguish between high and low p_T particles, the sensor spacing, and therefore the offset depending on the incidence angle within the modules, is increased towards the inner layers of the Outer Tracker. The PS module will be built in a 4.0 mm, 2.6 mm and 1.8 mm version while the 2S modules has two flavours with spacings of 4.0 mm and 1.8 mm. As far as possible it was tried to share the developed designs, techniques and parts between both module types to reduce the number of needed chips, parts, developments and suppliers. The following sections describe the components and concepts of p_T trigger modules on the basis of the 2S module [CMS18].

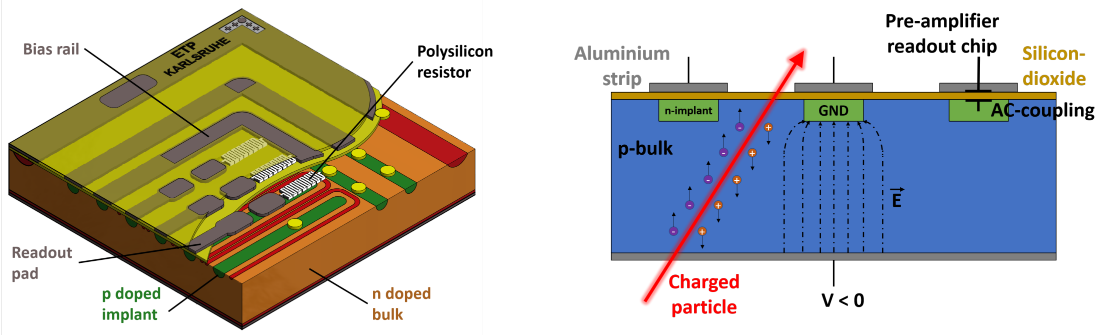

(a) (b)

Figure 3.6.: Functionality of a silicon strip sensor. (a) All positively doped strip implants of the sensor are connected to the bias rail via polysilicon resistors. The sensor backside is on a high negative potential. Ramping up the reverse bias voltage depletes the negatively doped bulk in between. The readout electronics is connected to the AC-coupled aluminium pads on top of the implant. (b) Charged particles generate electron-hole pairs inside the silicon lattice. Due to the presence of an electric field they drift apart from each other, and the signal can be detected on the overlying aluminium strips [Har17].

3.3.1. Silicon Sensors

The 2S module contains two identical silicon strip sensors for the detection of charged particles. Silicon belongs to the group IV of the periodic table and is an indirect semiconductor. Doping the material with negative or positive impurities generates energy states near the conduction and valence band, increasing the number of free charge carriers. Combining negatively and positively doped semiconductors creates a p-n junction, widely used in conventional diodes and transistors. At the contact area a non-conductive volume arises. This volume can be increased by applying a voltage in reverse-bias direction. Charged particles crossing such a depleted volume create electron-hole pairs by ionization. The amount of generated charge is Landau-distributed and a Minimal Ionizing Particle (MIP) creates on average about 76 electron-hole pairs per micro-meter in depleted silicon [Har17].

To operate a silicon strip sensor the reverse-bias voltage has to be applied between the strip implants and the sensor backside. As shown in Figure 3.6, each strip implant on the top side of the sensor is attached via a polysilicon resistor of about $1.5\,\mathrm{M\Omega}$ to the bias rail which is connected with a wire-bond to the ground of the front-end electronics. The backside is electrically connected with a flex circuit tail to the module's high voltage supply. Once the volume in between, called bulk, is depleted, electron-hole pairs generated by charged particles drift to the implant and sensor backside. The signal is read out via the AC-coupled aluminium strip on top of the implant. The coupling capacitance between the implant and the aluminium strip is about $30\,\mathrm{pF/cm}$.

The sensors of the 2S modules are segmented in two rows of $5\,\mathrm{cm}$ long strips arranged with a pitch of $90\,\mathrm{\mu m}$. The active sensor volume is $290\,\mathrm{\mu m}$ thick while the physical thickness is $320\,\mathrm{\mu m}$. A voltage of about $240\,\mathrm{V}$ is needed to reach full depletion of an unirradiated 2S sensor. In such a volume, the signal generated by a MIP is approximately $22\,000\,\mathrm{e}^-$. Depending on the position, incidence angle and presence of the magnetic field the charge spreads on multiple strips generating a cluster.

Due to its p-n junction the sensor draws a voltage-dependent leakage current which results in heat dissipation P according to $P = U \cdot I$, where U is the applied bias voltage and I is

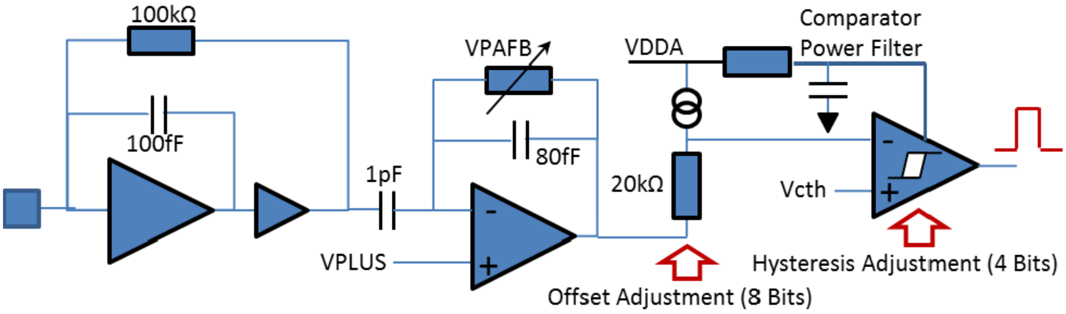

Figure 3.7.: Front-end of an input channel of the CBC. After a two-staged amplification the analogue signal can be adjusted with an offset before it is fed to the comparator, leaving only binary hit information. V_{Plus} is the bias voltage of the post-amplifier and V_{PAFB} controls its feedback bias current. VDDA is the supply voltage for the analogue circuitry [Col19b].

the leakage current. Additionally, the leakage current is depending on the temperature of the sensor. Therefore it is crucial to cool the sensor either by the surrounding air or with a dedicated cooling structure to avoid a so called thermal runaway in which an increasing leakage current heats up the sensor, which in return results in an even a higher leakage current.

In addition to thermally induced leakage current, irradiation worsens the sensor performance dramatically by introducing new defects in the lattice. Extensive irradiation studies showed that the leakage current increases linearly with the fluence $\Delta I/V = \alpha \cdot \Phi_{\text{eq}}$ [Mol99]. To reduce the heat dissipated inside the detector volume, the future Outer Tracker of the Phase 2 Upgrade is going to be operated with a sensor temperature of about $-20\,°\text{C}$ [CMS18].

3.3.2. On-module Electronics

To meet the demanding requirements and include new functionalities, most of the electronic components used in the p_T trigger modules are custom designed objects. The 2S module contains two front-end (FEH) [Gad+18] and one service (SEH) hybrid [Fel+18]. The FEH is developed at CERN, the SEH at the RWTH Aachen. The two FEHs house eight CMS Binary Chips (CBC) [Uch+18], developed at the Imperial College London, and one Concentrator Integrated Circuit (CIC), developed at CERN and IPN Lyon [Nod+18]. The two FEHs are connected with plugs to the SEH, which is responsible for the data transmission and powering of the module. The FEH is a flexible printed circuit board folded around a stiffener made out of aluminium nitrate and carbon fibre reinforced polymers (CFRP). With the fold over every second channel is routed downwards to be able to also connect the bottom sensor via wire-bonds like the top sensor. The SEH is also attached to a CFRP stiffener and has additional connections to the sensor backsides to apply the high voltage for depletion.

The CMS Binary Chip

Each of the 4064 silicon sensor strips is connected to a front-end channel of a CBC. One CBC handles 127 channels of the top sensor and 127 channels of the bottom sensor. The CBC outputs two data streams. The stub data directly contributes to the L1 trigger decision at 40 MHz. The trigger data is only sent out after an L1 trigger decision was made and the chip receives the signal from the back-end.

As shown in Figure 3.7 each channel of the CBC has an analogue front-end with a charge sensitive pre-amplifier followed by an adjustable gain amplifier. Afterwards an offset can be

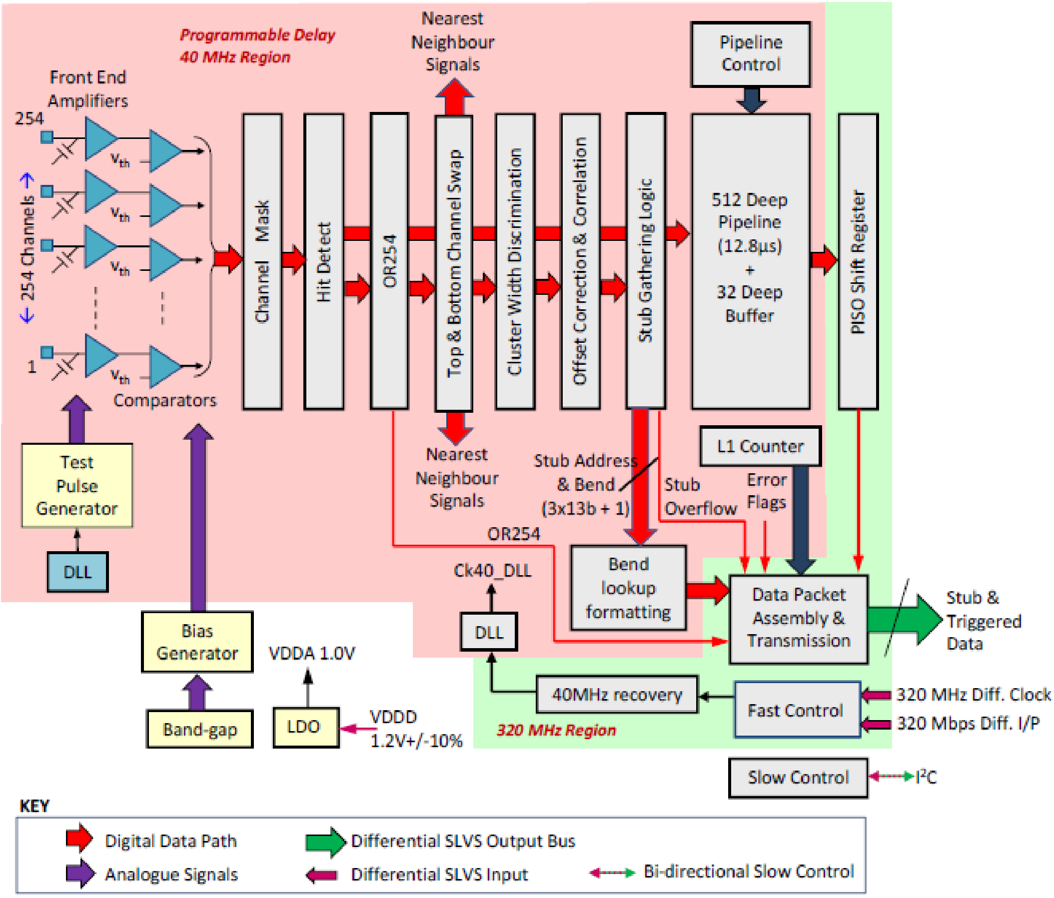

Figure 3.8.: Block diagram of the CMS Binary Chip. Connected to 2 × 127 sensor strips each CBC generates a trigger and stub data output on six Low Voltage Differential Signal (LVDS) lines. Each CBC is directly connected to its neighbours, sharing hit information to avoid stub inefficiencies between two chips [Uch+18].

added to the signal before it is processed by a comparator. The load capacitance of a strip in a 2S module is about 9 pF, resulting in a front-end noise of roughly 1000 e^-. Because the CBC is a binary chip the information about the amplitude of the pulse is lost and only a positive (1) or negative (0) hit bit representing the result of the comparator is further processed in the chip.

To quantify the responsiveness of the front-end, a test pulse calibration can be performed, injecting charge from a capacitance directly into the channel's front-end. Due to the manufacturing process the size of this capacitance is known with a variation of about 20 %. The threshold voltage of the comparator can be adjusted stepwise in Digital Analogue Counts (DAC) counts called V_{Cth}. Depending on the chip version the precision is 4 or 1 mV. By injecting a known amount of electrons while increasing the threshold it is possible to reconstruct the test pulse amplitude despite the binary readout. Repeating the measurement with a different test pulse height a correlation between the V_{Cth} and the input charge in electrons can be extracted with a precision given by the variation of the stated capacitance. Due to the electron readout and thus negative signal a lower DAC value sets a higher threshold.

As shown in Figure 3.8 the CBC is operating on two clock domains. While the 40 MHz clock domain is responsible for processing the hit detection, the 320 MHz domain takes care of data transfer and fast control commands. The 40 MHz clock signal has a programmable delay in steps of one nanosecond. With this it is possible to shift the hit detection logic to the most efficient time slice within one bunch crossing and to compensate effects of differing time of flight in different layers throughout the Outer Tracker.

Binary information received from the 254 channels is processes in several stages until it is stored in a buffer. First, possible faulty channels are masked by setting their hit information to 0. The CBC offers different hit detection modes. The default mode samples the comparator result with the 40 MHz clock. If the comparator result is positive during a rising clock edge the hit detect logic stays positive for one complete clock cycle. Highly Ionizing Particles (HIP) can generate very large pulses yielding in positive comparator results over multiple clock cycles and thus increase the occupancy. Therefore, a HIP suppression mode is implemented which forces the comparator result to be zero after an adjustable number of clock cycles. After the hit detection block the data is stored in a 512 frames deep ring-buffer to keep hit information of 12.5 µs on the chip. Within this time window a trigger signal has to be sent coming from the back-end to the readout electronics before data loss is encountered.

The generation of the stub data is done in parallel in the stub logic. Each chip shares hit information with neighbouring CBCs to avoid inefficiencies between two chips due to the possibility of particles crossing the module not perpendicular to the sensor planes and thus create hits in two neighbouring CBCs. Cluster signals above an adjustable cluster size are dropped for stub finding since they hint to low p_T particles crossing the sensor at high angles with respect to the sensor's normal. Depending on the module's location inside the tracker, an offset between the seed and correlation layer compensates geometrical effects. Afterwards the seed and bend information is gathered with a half strip resolution. To reduce the data output the initial 5-bit bend value is reduced to a 4-bit bend code given by an adjustable lookup table stored in one of the CBC registers.

The CBC has six LVDS data output lines, one for the asynchronously triggered L1 data and five for continuous stub data output. The triggered data frames are stored in a 32 frames deep buffer before they are serialised and sent out at 320 MHz. The full hit vector is sent out without zero suppression, which takes 38 bunch crossings. One CBC can detect and forward a maximum of three stubs per bunch crossing. Each stub has a certain seed position and bend value. This results in 40 bits of information which is split on five LVDS lines and sent out at 320 MHz permanently. An I2C line is used to change settings on the chip such as threshold, latency, phase delay and hit detection modes [Uch+18] [CMS18].

There are different versions of the CBC due to an iterative optimization process by the developers at Imperial College London. The first module prototypes introduced in Chapter 4 have readout hybrids housing eight CBCs of the second version called CBC2. The successor CBC3 and a version with minor corrections called CBC3.1 are used for the high rate tests described in Chapter 5.

The Concentrator ASIC

Each FEH houses eight CBCs connected to one CIC via 8 × 6 LVDS lines. The CIC acts as a data hub before the data is sent to the SEH. As a first step, each data line coming from the CBCs is phase aligned to compensate the different distances between each CBC and the CIC. The L1 data can be handled in two modes. The first is a debug mode in which the CBC's raw input is serialised and sent to the SEH. In this mode the trigger rate is limited to about 100 kHz. The default mode performs a clustering of the hit data storing only the cluster's position and width. With this, the maximum trigger rate depends on the occupancy and will be coping with an expected maximum of up to 750 kHz.

The received stub information of eight consecutive bunch crossings is sorted in a parallel sorting network according to the lowest bend values and thus highest p_T particles. Then, a maximum of 16 stubs per eight bunch crossings can be sent out by the CIC. This smooths the statistical distribution of hits in time and space and ensures optimal usage of the limited bandwidth [Cap+18] [Nod+18] [CMS18].

The Service Hybrid

The SEH houses the components for powering, monitoring and data communication of the module. Connected to both FEH the Low power Gigabit Transreceiver (LpGBT) receives the zero-suppressed L1 and trigger data coming from the two CICs. It serialises the data before it is sent out optically with a Versatile Link Transceiver Plus (VTRx+) at 5.12 Gb/s [Tea18] [Tro+17].

The LpGBT forwards the I2C commands to a Slow Control Asic (SCA). It is used to configure all FEH chips and the VTRx+ on the SEH. The LpGBT distributes the 320 MHz clock out of which the FEH chips recover their 40 MHz clock signal and fast commands. For monitoring the module conditions such as sensor temperature or the supply voltage and currents, five analogue and three digital signals can be measured by the LpGBT.

The SEH also houses a DC-DC converter which generates the necessary voltages for the FEH and SEH components. Since electrical power losses scale with I^2 the voltage applied on the power lines is 11 V and then converted to 1.25 and 1.0 V in the DC-DC converter reducing the dissipated heat inside the tracker significantly. Alternatively the cross-section of the power cables could be increased reducing the resistance, but this is not a feasible option in terms of the material budget [CMS18].

3.3.3. Module Mechanics

The p_T-trigger module mechanics has to meet several contradicting requirements challenging the design and assembly procedure. To avoid multiple scattering inside the tracker all deployed components should contribute as low mass as possible to the material budget. On the other hand, the power dissipated by the electronics needs to be cooled efficiently, which calls for short and low thermal resistance cooling paths. Therefore, light-weight materials with a high thermal conductivity are preferred. As shown in Figure 3.9, all module components are attached to bridges made of carbon-fibre reinforced aluminium (Al-CF), a unique material fulfilling several requirements such has high thermal conductivity and a low CTE. The CTE of the silicon sensors is 2.6×10^{-6}, requiring the mechanical fixation to have a similar value to avoid mechanical stress induced by cooling the detector down from 20 °C to -33 °C. The additional chopped carbon fibres in the material are not impairing the thermal conductivity but reduce the CTE of aluminium from 23.1×10^{-6} down to 4×10^{-6} very close to the CTE from silicon. A negative property of the material is its brittleness, requiring very careful machining and handling during module assembly.

The Al-CF bridge design is optimized to introduce as little material as possible while having a sufficient thermal performance. It is planned to keep the sensor temperature around -20 °C, while a fully irradiated module will generate about 7 W of heat. With a CO_2 temperature of -33 °C the temperature drop along the cooling services and modules needs to be less than 13 K. The thermal performance was simulated using finite element analysis and verified with measurements on thermal dummy modules. Due to the asymmetric heat deposition caused by the SEH, the 2S module has additionally to the 4 cooling joints on the long Al-CF bridges a fifth cooling joint on a small Al-CF piece, called stump bridge, below the SEH.

For sensor depletion the sensor backside is equipped with high voltage tails, which are electrically connected with wire-bonds to the backside aluminium surface. Polyimide strips serve as isolation between the sensor backside and the Al-CF bridges connected to ground via the cooling circuit. For a well-working stub detection a precise positioning of the two silicon strip sensors is mandatory. While a shift in respect to each other does not impair the stub

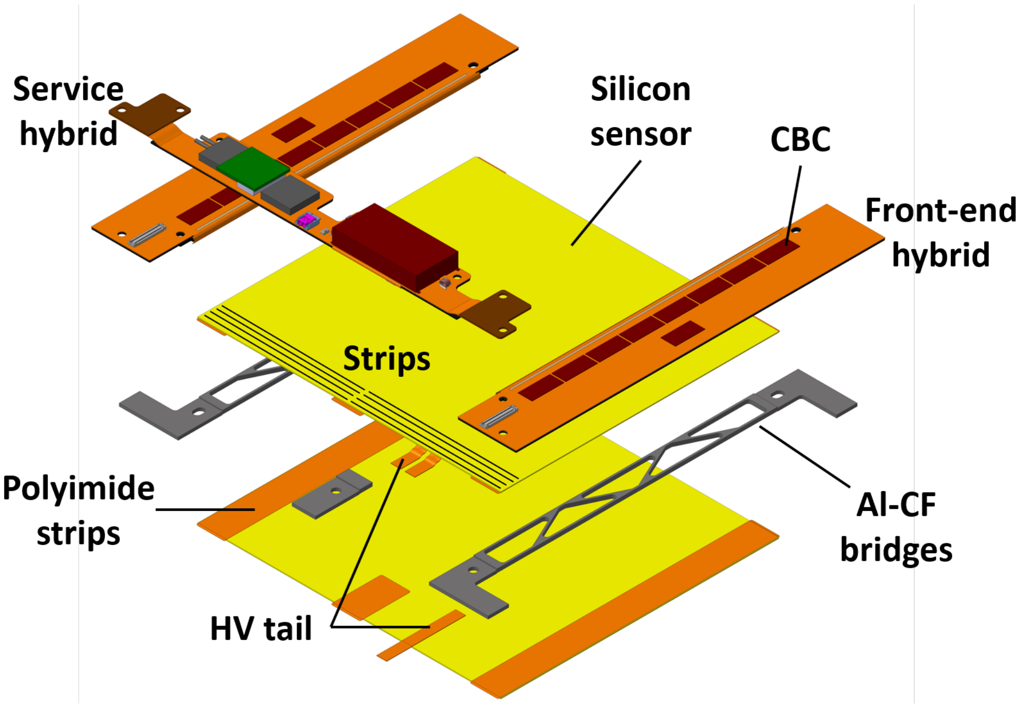

Figure 3.9.: Exploded view of a 2S module. All components of the module are attached to Al-CF bridges which are used as main cooling path and mounting structure in the detector. The hybrid flex circuits are folded around CFRP stiffeners glued on the Al-CF bridges. The sensor backside is on high voltage while the bridges are connected to ground. Therefore, additional polyimide strips glued to the sensor backside serve as isolation.

finding, a tilt between the two overlaying strips results in a degradation of the stub detection efficiency. Therefore, the maximum allowed rotation is half a pitch length along the sensor edge resulting in a maximal allowed misalignment angle of 400 µrad.

The hybrids are glued to the extensions of the Al-CF bridges. The FEHs are pushed towards the sensors assuring the alignment of the wire-bond pads. The SEH is placed precisely using alignment pins. Flexible plugs connect the SEH with the FEHs and the HV tails. 4064 wire-bonds link each CBC readout channel with a strip of the sensor. Additional 8×3 wire-bonds connect the bias rail of the sensor on each sensor corner with the ground potential of the FEH. For mechanical protection the wire-bonds are covered with a silicone-based encapsulation material [CMS18].

4

Assembly and Qualification Procedures of 2S Modules

The future CMS Outer Tracker will consist of 13 000 PS and 2S modules, which will be produced all over the world and integrated into larger scale structures in assembly sites in Europe and North America before the tracker will be installed in CMS at CERN. The challenging requirements for building modules described in Section 3.3.3 call for a highly controlled assembly process to keep the module quality high and failure rate low. As shown in Figure 4.1, each assembly site follows a detailed 2S module assembly procedure. Due to the differences in the infrastructures already available some testing approaches may differ among the assembly sites. The baseline procedure is based on mechanical fixtures called assembly jigs. This makes the crucial production steps reliable and of the same quality on each module independent from its assembly location.

KIT pledged to build 2000 2S modules between 2021 and 2023. Therefore, the production period is about 400 working days resulting in an average production rate of five modules per day. To compensate below-average production days it is planned to have a possible peak production of eight modules per day. Therefore, an eightfold assembly line has to be set up calling for a proper clean room arrangement. After reception tests most of the assembly steps are done in one large clean room, reducing the logistical effort and keeping the feedback loop as short as possible. Each test station should be automatised as far as possible to minimize the required time and numbers of trained staff. Together with this, it is planned to track the assembly process in a construction database which will give an overview of the current production status and parts request.

During the prototyping period the test procedures are even more detailed to reveal possible flaws in the assembly process or material problems and their origin. KIT was the first production site that has built a functional module outside the pilot center CERN. So far two functional prototype 2S modules have been built at KIT. Due to the ongoing development of the components used in the p_T-trigger modules the first prototypes do not have the final geometry and electrical functionality. To practice the assembly steps, substitute materials such as glass plates with the exact size of 2S sensors and bridges out of aluminium instead of Al-CF are used.

During this thesis several assembly jigs and test stations have been designed and commissioned to ensure a reliable production process. This chapter describes in detail the assembly and test procedures used for the first two KIT 2S modules and their results. While the first module was assembled successfully, it took two trials to build the second module because in the first iteration the module was damaged beyond repair during the wire-bonding process. The undamaged components were removed and reused to build a new module.

4.1. Assembly Procedure at KIT

Figure 4.1 shows the assembly and test procedures to build a 2S module. At the beginning, each silicon strip sensor is checked for its dicing precision with a dedicated metrology station.

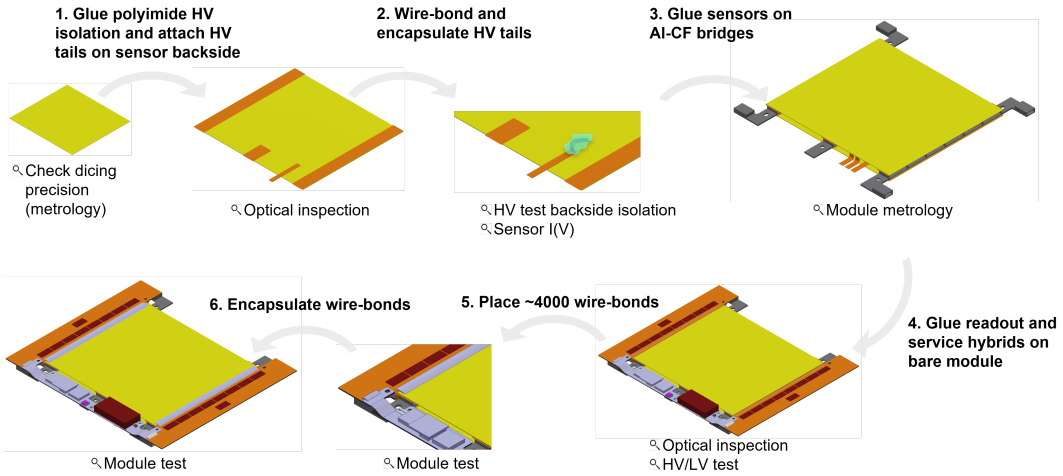

Figure 4.1.: Steps of the 2S module assembly. After each step tests are performed to keep track of the modules quality. Starting with a check on the sensors dicing precision their backside is isolated with polyimide strips. Simultaneously the HV tails are attached, which are then electrically connected with wire-bonds. After the wire-bond encapsulation a pair of two silicon sensors is glued to the Al-CF bridges forming a bare module. The sensor alignment is then checked in a custom-made metrology station. Afterwards the hybrids are attached to the bare module. Once the module is wire-bonded it is tested in a dedicated station. The test is repeated after applying the wire-bond encapsulation.

Afterwards each sensor's backside is isolated with polyimide strips. In the same step the high voltage (HV) tails are attached to the backside. The HV tail differs depending whether the sensor will be assembled as a top or bottom sensor in the module. After a visual inspection of the gluing quality the HV tail is wire-bonded to the sensor backside and the wire-bonds are encapsulated with a drop of silicone elastomere for proper protection. In the following, each sensor assembly is tested for the high voltage stability of the polyimide strips and an $I(V)$ curve of the sensor is measured to test its electric functionality. Two sensors are glued to a set of Al-CF bridges containing two long and one short bridge. The short bridge, called stump bridge, was introduced to compensate for the asymmetric heat dissipation in the module ensuring a similar heat flow through all 5 cooling joints. The bare module assembly has to meet a parallel alignment between the strips of the two sensors of 400 µrad. The alignment between the two sensor edges is validated in the same metrology station used to check on the dicing precision of the sensors. The combination of the edge alignment and dicing precisions of the two sensors yield the final strip-to-strip alignment. In a subsequent gluing step, the readout and service hybrids are attached to the bare module. A total of 4064 readout and 24 bias wire-bonds have to be placed on the module to connect each sensor strip to the readout channel of a CBC and to deplete the silicon sensors. If the following module test confirms the functionality of the module its wire-bonds are encapsulated with a silicon elastomere. The last step in the assembly process is an additional module test.

Each module is protected with an aluminium carrier on which it is placed and fixated after the bare module assembly. The module does not leave its carrier until it is integrated on larger structures.

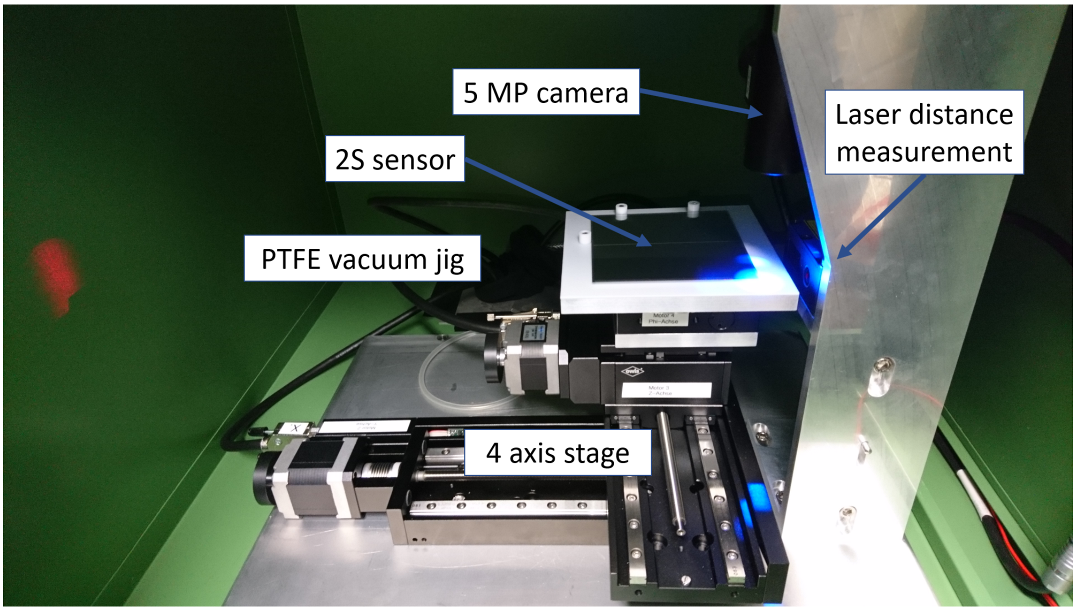

Figure 4.2.: Metrology station for the 2S module assembly. The station can either be used to measure the dicing alignment of single sensors or to check the sensor alignment of a bare module. The first is done with a 5 megapixel camera mounted above the stage while the second is realised with a laser-based distance measurement. The four-axis stage moves the sensor or module edge below the camera or besides the laser. Once an edge is measured the table turns by 90 degrees and proceeds with the next edge. Details on the measurement procedures are given in Appendix A.

4.2. Sensor Dicing Alignment

Key element to ensure the p_T filtering functionality of the p_T-trigger modules is the strip-to-strip alignment between both sensors. During the assembly, this is ensured by a precise jig using alignment pins as described in Section 4.4. Therefore, the dicing line of the sensor edge should be as parallel as possible with respect to the strip implants. The manufacturer is constrained to cut the sensors within a 10 µm wide dicing window resulting in a maximum allowed tilt of about 100 µrad.

There are two techniques, called blade and stealth dicing, to cut a silicon wafer into smaller pieces. The first one uses a thin blade cutting through the silicon lattice. Due to the mechanical abrasion the dicing precision may vary over time and the sensor edges show chippings. The second and preferred technique uses a pulsed laser causing defects within the silicon lattice along the dicing line. Due to the weakened lattice structure the wafer breaks easily by applying a small pull force to it [Ham19].

In the scope of this thesis a semi-automatic test station, called metrology station, was developed to measure the dicing angle of silicon sensors using a 5 megapixel camera. It is mounted above a four-axis stage, which has a phi-rotation table placed on a XYZ translation table. A vacuum jig made out of polytetrafluoroethylene (PTFE) is mounted on the phi table to fixate a 2S sensor. As shown in Figure 4.2, the station sits in a light-tight housing for steady conditions. The station is operated with a custom LabView-based application while the generated measurement data is analysed and visualized with a dedicated Python script. Further details on how the measurement procedure is implemented in the software are given in Appendix A.

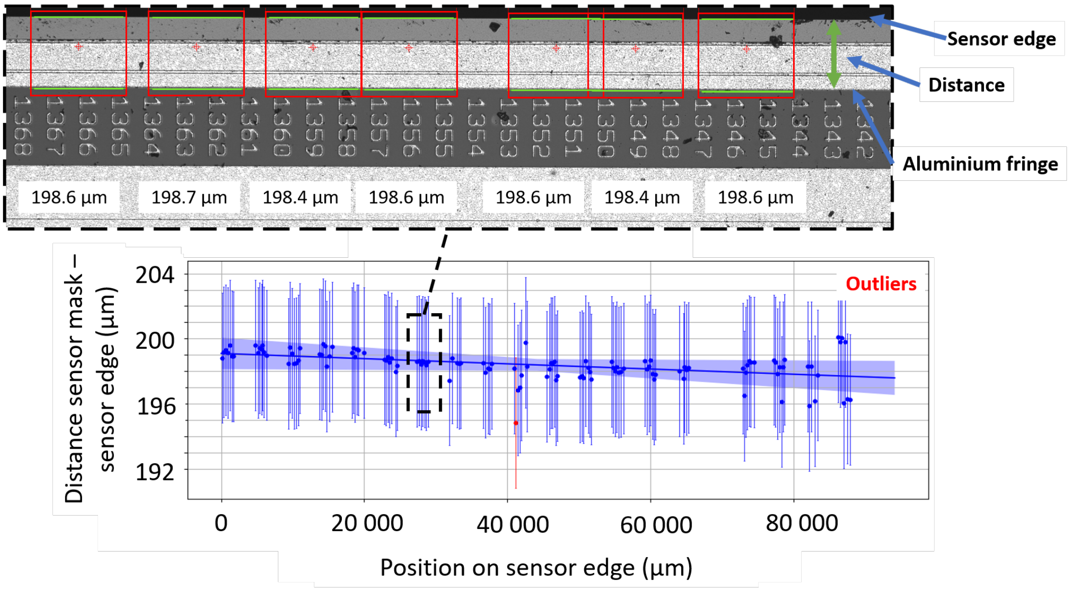

Figure 4.3.: Dicing angle analysis. Each image contributes a group of measurements to the graph. Within each image up to 7 patterns are recognised to measure the distance between the dicing edge and aluminium mask. After excluding outliers marked in red, the slope of the linear fit represents the angle between the dicing edge and aluminium mask and thus the strip implants. Outliers are excluded with an iterative fitting method. Additionally, the uncertainty of the fit is highlighted by the light blue band. To speed up the procedure the number of images taken along one sensor edge will be reduced in the production phase.

The dicing angle measurement is based on an automated pattern recognition procedure. Due to the four-axis stage each of the four sensor edges can be moved below the camera mounted on a fixture above. Several images are taken with the camera on different positions of a sensor edge. As shown in Figure 4.3, the software searches up to seven identical patterns in each image. Each pattern contains the edge of the sensor itself and the fringe of the aluminium mask of the sensor's periphery. By design, the fringe of the aluminium surface is parallel to the sensor implants. Having these two distinct edges, the sensor edge itself and the fringe of the alumnium surface on the sensor, the analysis extracts the distance in between them with a contour detection. The resolution of the camera is 1.2 µm per pixel but the contour of the edge or the aluminium mask might be blurred among several pixels. Therefore, the uncertainty of a single measurement based on the recognition of the two contours is estimated to be 4 µm.

Each image contributes a group of measurements at a different sensor position. As shown in Figure 4.3, the derived distance from multiple measurements performed in multiple images are combined in a graph which is fitted with a linear function. Due to the very small angles the slope can be taken as representation of the dicing angle between the sensor edge and strips. Additionally, the uncertainty of the linear fit is highlighted. Once a side is measured, the stage turns 90 degrees to proceed with the following sensor edge.

During the prototyping period all four sensor sides are evaluated on their dicing angle with about 20 images per side. In the later production period the procedure will be accelerated by taking only about four images on solely one side having still a sufficient precision of about ±25 µrad. If the dicing angle is not within the specifications the opposite edge can be evaluated since the 2S sensor is rotationally symmetrical by 180 °. A database tag will be added to the favoured sensor edge to be used during the attachment of the HV tails and polyimide strips. This side, having the tails, will be in contact with the alignment pins on the bare module gluing jig.

If a sensor has dicing angles exceeding the vendors specifications it will be rejected. In case of sensor shortage, a fallback solution is to pair sensors having about the same dicing angles but with an opposite sign. This would again result in a good strip-to-strip alignment after the bare module assembly because the sensors top-sides are facing away from each other. Therefore, it is necessary to pass this sensor information to the staff on the assembly line pairing two matching sensors.

Additional pictures are taken at the position where later the sensor edge will be in contact with the alignment pins. In the unlikely case of a damaged part of the sensor edge just in this area the opposite side can be evaluated and tagged if the dicing angle is within the specifications and the edge is undamaged.

Table 4.1 summarizes the dicing angles on various silicon sensors measured with the metrology station. Referring to the vendor specification of angles below 100 µrad all those sensors would be accepted. Dummy sensors, slightly differing in the aluminium mask and the dicing technique, were investigated as well since they are used for the assembly of non-functional dummy modules. No systematic relation between the angle and the sensor edge or the dicing process are seen. The uncertainty of the measurement is about 20 µrad, which translates to a deviation of approximately 2 µm along the sensor edge.

4.3. Backside Isolation and HV Tail Gluing

The silicon sensors are operated with high voltage which is applied between the sensors' bias rail on the front-side and the aluminium backside. Since the Al-CF bridges are connected to the cooling circuit and thus to ground, the silicon backside has to be electrically isolated to

Table 4.1.: Dicing angle measurements. All four dicing angles of a sensor are measured during prototyping period. All sensors measured are within the given specification of 100 µrad. No systematic trends referring to the dicing technique or edge orientation are visible.

Sensor	Dicing technique	Side 1 (µrad)	Side 2 (µrad)	Side 3 (µrad)	Side 4 (µrad)
CMS-ddFZ240_06_2S	Stealth	5 ± 13	-9 ± 17	-7 ± 13	-2 ± 14
CMS-ddFZ240_07_2S	Stealth	-14 ± 18	3 ± 19	-7 ± 13	-5 ± 25
CMS-ddFZ240_01_2S	Stealth	-14 ± 19	-16 ± 14	-10 ± 17	-11 ± 15
CMS-ddFZ200_20_2S	Stealth	19 ± 18	-34 ± 17	-18 ± 17	11 ± 23
CMS-ddFZ200_16_2S	Stealth	-6 ± 18	-3 ± 18	-3 ± 15	-2 ± 17
CMS-ddFZ240_33_2S	Stealth	-4 ± 18	-20 ± 21	-2 ± 16	-9 ± 16
MCZ Dummy 1	Blade	-3 ± 16	3 ± 14	7 ± 26	11 ± 14
MCZ Dummy 2	Blade	-5 ± 18	11 ± 15	7 ± 15	12 ± 15
MCZ Dummy 4	Blade	45 ± 23	11 ± 21	29 ± 17	4 ± 19
MCZ Dummy 5	Blade	47 ± 15	17 ± 47	37 ± 15	13 ± 22

avoid a short circuit which would make the module inoperable. This is realised with 25 µm thick polyimide strips attached to the backside using a precise gluing jig.

4.3.1. Assembly

Independent from part and assembly tolerances a minimal overhang of 500 µm polyimide should always separate the surfaces on ground potential from parts on high voltage potential to ensure stable electrical operation up to 1000 V. During the same assembly step, the HV tails are glued to the sensor backside. For the attachment of both, the HV tails and the polyimide strips, a low viscosity epoxy resin, Polytec EP 601 LV, is used [Pol19a]. The silicon sensors dissipate their heat through the polyimide glue joint making it crucial to minimize the thermal resistance as far as possible by having a high wetting and small glue thicknesses. Glue excess around the sensor edge has to be avoided since it could impair the electrical performance of the sensor. Glue excess onto the Polyimide strip itself could prevent the Al-CF bridge from laying flat on the sensor backside, worsening the assembly precision and thermal performance.

With a daily peak production of eight modules, 16 sensor backsides have to be isolated each day. This suggests a semi-automatic glue application procedure to guarantee reproducibility and thus lack or excess of glue. In the scope of this thesis a custom-made dispensing gantry was designed and programmed. As shown in Figure 4.4, a dispensing gun controlled by a volumetric dispenser is mounted on a three-axis gantry. It applies glue or wire-bond encapsulation material on four sensors or 2S modules placed below. The material is loaded in a cartridge and pushed out precisely with an attached stepping motor. The material is pushed through a dispensing tip, whose design varies with the material to be applied. For the in-plane tip calibration a camera monitors the location of the very end of the tip. The tip height is calibrated with a forked light barrier sensor. The dispensing gantry and its devices are controlled by a custom LabView-based software environment having a design similar to the metrology station software. With it, it is possible to program, save and load dispensing routines. Once the tip is calibrated and the user has loaded or programmed the dispensing steps, the software generates a sequence of machine states to process the routine. Further details on the dispensing gantry and the software developed are given in Appendix B.

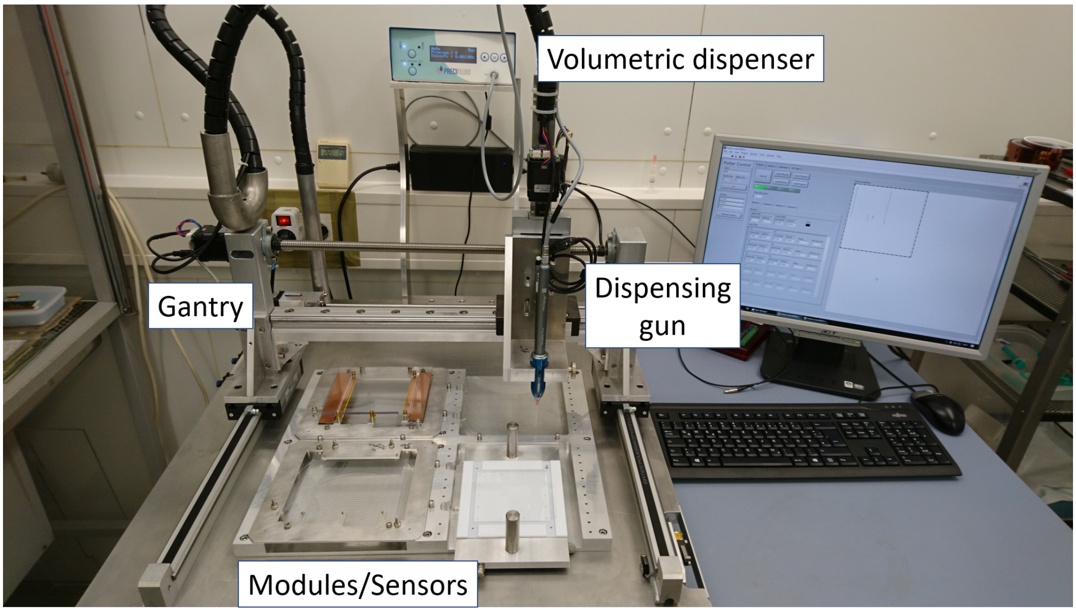

Figure 4.4.: Dispensing gantry used to apply glue or wire-bond encapsulation material in the 2S module production. It houses a dispensing gun attached to a volumetric dispenser and is controlled by a custom-made LabView-based software environment. Four modules or silicon sensors can be handled at once.

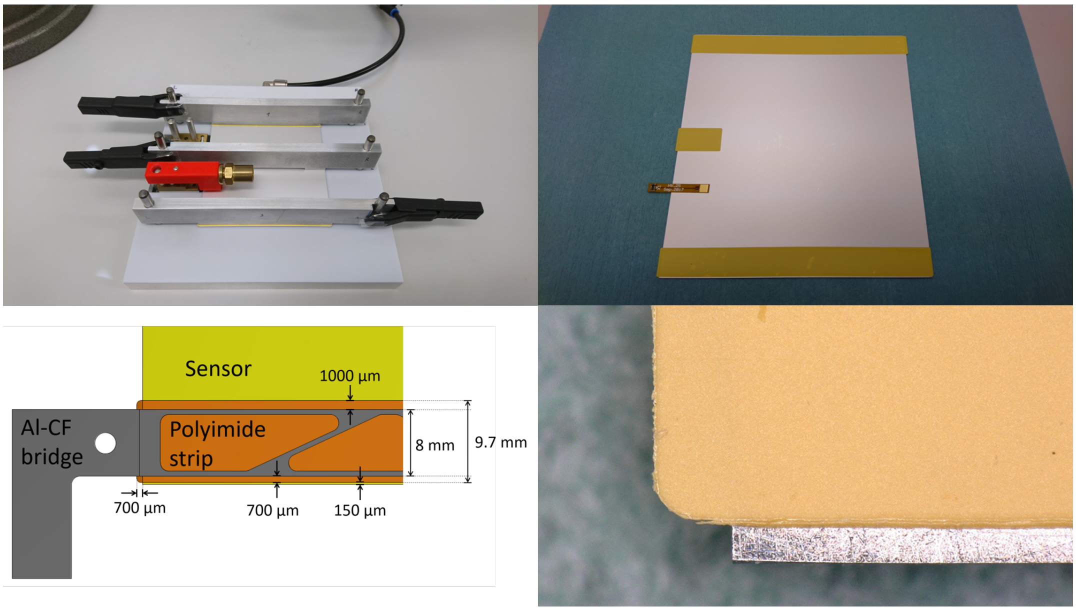

Figure 4.5.: The gluing jig (top left) used to precisely glue the polyimide strips and HV tails on the sensor backside (top right). The positioning of the strips with respect to the sensor edge and Al-CF bridges according to the modules design (bottom left) can be met provided that the components' dimensions are within the specifications. No glue excess between sensor and polyimide strip is observed in this crucial assembly step (bottom right).

As shown in Figure 4.5 the Al-CF bridges are 8 mm and the polyimide strips 9.7 mm wide resulting in an overhang of 1 mm towards the inner side of the sensor and 0.7 mm towards the sensor edge. The strips are 1.4 mm longer than the 2S sensor to have an overhang of 0.7 mm at the position where the Al-CF bridges stick out of the sensor. This is necessary because the dicing edge itself is on high voltage. To respect the 500 µm separation of HV to ground with these component dimensions the placement window parallel to the sensor edge and bridges is 350 µm and 200 µm perpendicular to it. To achieve this, precise gluing jigs are needed and well-trained staff is mandatory.

In the scope of this thesis extensive gluing studies have been performed to optimize the glue application in terms of reproducibility, wetting and minimal gluing thicknesses. Key elements are the amount of glue to be applied, the glue pattern and the tip height. The optimised results are documented here: Two lines of glue with 0.06 ml/mm are used to attach the long polyimide strip. The short one and the HV tail are attached with multiple dots of glue of about 0.015 ml. The tips used are flexible PTFE tubes and have an inner diameter of 0.61 mm. The distance between dispensing tip and sensor surface is about 50 ± 20 µm. Further details on the glue pattern and application are given in Appendix B.4

Once the glue pattern is dispensed to the sensor backside the polyimide strips and HV tails are attached in a dedicated gluing jig also shown in Figure 4.5. Before, the strips are placed on pick-up tools wetted with isopropyl. The pick-up tools have the same width as the Al-CF bridges. L-shaped stops are brought in contact with the pick up tools. Their edges are machined in such a way that the polyimide strips have the required overhang on the pick-up tool when they are slightly pushed against the stop. Once aligned, the L-shaped stops are removed and the pick-up tools are carefully placed upside down on the sensor backside. They are guided with precise alignment pins attached on the gluing jig. Once the strips are placed, the glue spreads due to capillary forces between the sensor backside and polyimide strip until it stops at its edge. This process takes up to 20 minutes. With the given amount of glue applied and the surface covered by the polyimide strip the resulting glue thickness is about 5 to 7 µm. The pickup tools are left on the glue joint during the curing time of 24 hours to enable a flat glue layer. The isopropyl in between does not completely evaporate within 10 minutes giving the staff enough time for the assembly.

During the prototyping period each polyimide strip assembly is inspected with a microscope on possible delamination and the precision of the placement as shown in Figure 4.5. The amount of glue applied on the sensor backside ensures a wetting of above 99 % and is enough to enable the generation of a glue meniscus on the end of the polyimide strip. The meniscus shows that the glue has fully spread below the strip, preventing it from sticking up at its fringes. The positioning of the strips was within the specifications for all the dummy modules built. The functional modules are slightly out of the specifications because the functional sensors delivered had larger dimensions while the purchased polyimide strips subceeded their specifications. This stresses the importance of checking the components or assemblies upon reception.

4.3.2. HV Tail Wire-bond Encapsulation

The HV tails are small flex circuits with a connector, which is plugged into the service hybrid once the hybrids are glued to the bare module. It has an exposed surface on which the wire-bonds are placed to connect the sensor backside electrically. This is done on a PTFE vacuum jig and a semi-automatic wire-bonding machine. Once the wire-bonds are placed they are protected with a drop of silicone elastomer, Sylgard 186 [Cor19]. It takes 48 hours for the silicon elastomere to cure completely but after 24 hours it is stable enough for further handling. More details and studies of the wire-bond encapsulation material are given in Section 4.7.

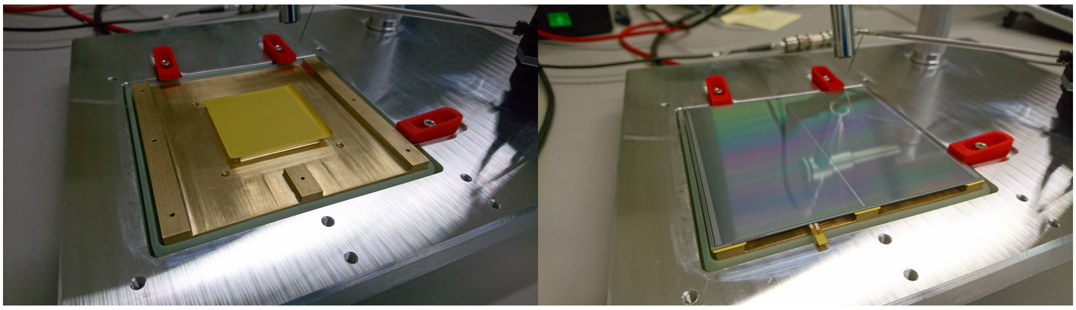

Figure 4.6.: The HV / I(V) test system uses three brass rails emulating the Al-CF bridges in a 2S module (left). The sensor assembly is placed with the polyimide isolation on the rails and fixed by vacuum (right). HV applied between the sensor backside and brass rails tests the strip isolation. A subsequent $I(V)$ curve measurement validates the functionality of the sensor.

4.3.3. HV / I(V) Test System

After the HV tail is wire-bonded to the sensor backside and protected with an encapsulant, the assembly is tested for its high voltage stability, verifying the electrical isolation of the polyimide strips. In addition to this the $I(V)$ curve of the sensor is measured contacting the HV tail and the bias rail on the sensor's top side with a probing needle. In the scope of this thesis a test system was designed to perform these tests. 5 % of the sensors are going to be characterized before the module assembly in dedicated institutes approved as Sensor Qualification Centres to keep track of the sensor's quality on a sample basis per batch. Therefore, for 95 % of the sensors this is the first time the electrical characteristics of the sensor are evaluated after they have left the manufacturer. Damaged sensors have to be sorted out, broken polyimide isolator strips can be removed and replaced.

As shown in Figure 4.6 the setup contains three brass rails emulating the Al-CF bridges. The sensor is placed on the rails and pushed against stops for a well-defined alignment. Vacuum is applied to fixate the sensor assembly on the rails. To verify the HV stability a voltage is applied between the sensor backside through the tails and the brass rails and ramped up to 1000 V. Possible shorts are indicated by sparking or an atypical increase in the current, which is detected by the attached custom control electronics. On sensor assemblies with intact HV isolation the $I(V)$ curve is measured placing a probing needle on the bias rail. Suspicious sensors with increased current or an atypical $I(V)$ curve are inspected optically and possibly rejected. The values measured can also be compared to the measurements done by the manufacturer. The results are uploaded in a database and can later be compared with $I(V)$ curves measured on the final module, to validate the integrity of the silicon sensor throughout the module assembly. The measured $I(V)$ curves during module assembly are summarized in Section 4.8.

4.4. Bare Module Assembly and Alignment Measurement

4.4.1. Bare Module Assembly

As mentioned in Section 3.3, a properly working stub logic puts strict requirements on the parallelism of the strips on the two sensors in a p_T-trigger module. The maximum tilt allowed is 400 µrad. Therefore, an accurate bare module assembly is a crucial step for the functionality in the later tracker. The assembly is made on a precise gluing jig using alignment pins shown in Figure 4.7. The first sensor is placed face down on a PTFE surface on the jig. Afterwards it is moved with pushing springs towards three alignment pins. A visual check of the edge's

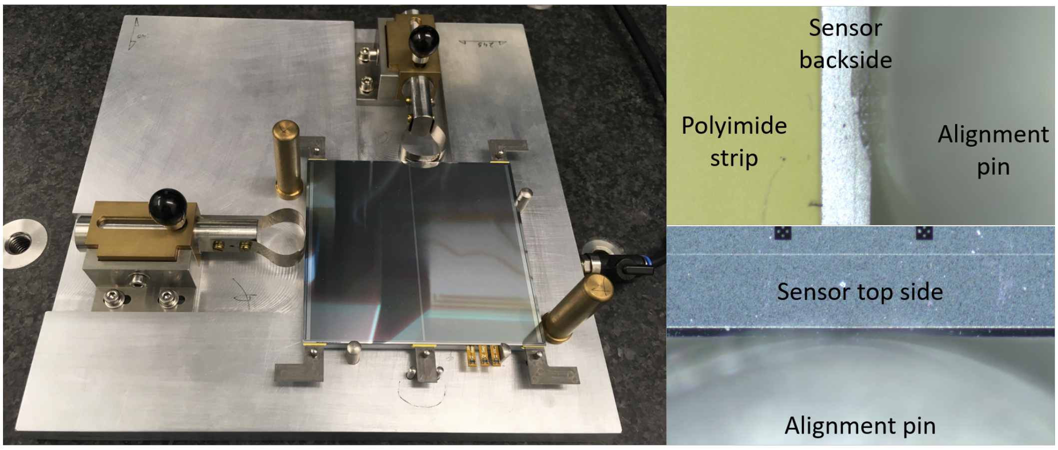

Figure 4.7.: Assembly of a bare module. The bottom sensor, the Al-CF bridges and the top sensor are aligned with precision pins using pushing springs and vacuum (left). The contact of the sensors to each of the three alignment pins is verified using a microscope (top right and bottom right). After the deployment of the components a weight is added on top of the assembly to fixate it for curing.

contact with the alignment pins is mandatory before vacuum is applied to fixate the sensor in its position. The pushing springs are removed and the bridges are placed with the help of positioning pins on the sensor backside. The bridges are covered with a boron nitride filled epoxy resin Polytec TC437 [Pol19b]. For this an aluminium bar that has the same length as a 2S sensor and a width of a bridge is wetted with Polytec TC437. The bridges are dipped on the bar to pick up glue. The filling material increases the thermal conductivity, which is beneficial for the thermal performance of the module. Due to its higher viscosity compared to the Polytec EP 601 LV the filled glue remains close to the glue joint reducing the probability to protrude over the sensor edge. The second sensor is placed facing up on the bridges and is pushed against the same alignment pins as the first sensor. Due to the machining process the Al-CF bridges tend to have a slight bow. In addition to this, the silicon sensors tend to have a bow as well. Therefore, after a visual validation of the pin contact a weight is applied on the assembly keeping it in a flat state during curing, which takes about 24 hours.

4.4.2. Bare Module Alignment Measurement

The alignment of each assembled bare module has to be measured. This is done with the metrology station introduced in Section 4.3. Additional to the camera it houses a laser-based distance measurement device mounted right beside the vacuum jig. The device measures the distance of flat objects placed 25 mm in front of it within a range of ±1 mm with a 40 µm wide laser spot that is reflected by the object on a light sensitive array.

The bare module is placed on the jig and fixated by vacuum and the laser spot is centred on the 320 µm thick edge of the top sensor. The bare module is then moved along the distance measurement device. The distance is measured by the device at a rate of 100 Hz resulting in about 10 000 measurement points per edge. Afterwards, the bare module is moved upwards to focus the laser spot on the bottom sensor's edge and the module again moves along the laser spot scanning the distance to the bottom sensor edge. Each of the two rows of measured data points can be fitted with a linear function, resulting in the orientation of each sensor edge with respect to the laser measurement device. By subtracting both linear functions the relative orientation of the two sensor edges can be calculated. Figure 4.8 shows a bare module

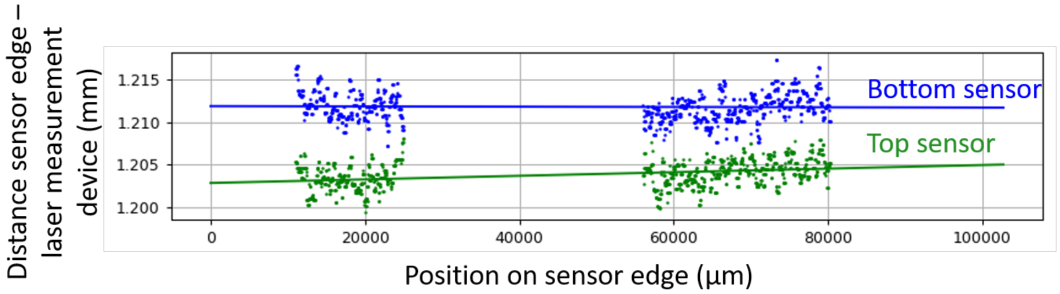

Figure 4.8.: Edge alignment measurement of a bare module. The measurement points of the top (green) and bottom (blue) are fitted with a linear function. The difference of both functions yields the edge alignment. Areas in which the laser reflection is disturbed are masked before the linear function is fitted to the data. The corresponding measurement points are omitted in the graph.

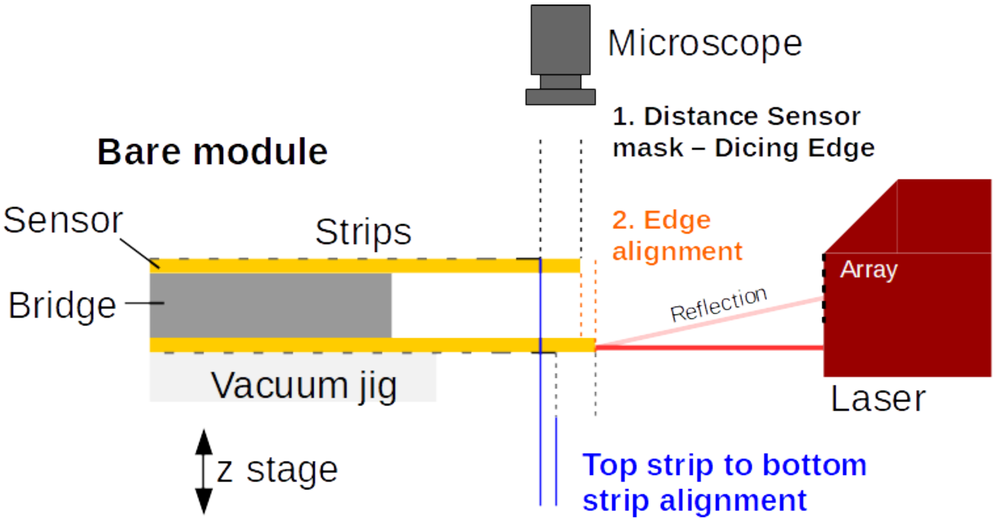

Figure 4.9.: Illustration of the strip-to-strip alignment reconstruction with the optical dicing angle measurement and the laser-based edge alignment measurement.

alignment measurement. The bridges or HV tails standing out of the sensor assembly can impair the reflection of the laser spot. Therefore, the measurement points of these areas are masked before the linear fit. Due to the roughness of the sensor edge the uncertainty of a single measurement point is estimated to be about ±7 µm. At least the module side on which the HV tails are attached has to be measured to get the edge alignment information needed for the strip-to-strip alignment. This is necessary because this side was aligned in the bare module gluing jig and these sensor edges were evaluated in the sensor metrology station.

Because thse measurements solely give the edge-to-edge alignment of the bare module, the dicing measurement has to be considered as well to receive the final strip-to-strip alignment illustrated in Figure 4.9. The coordinate system of all measurements is chosen such that a simple addition of the measurement values yields the strip-to-strip alignment. Details on the measurement and analysis procedure are given in Appendix A. Table 4.2 summarizes the edge and strip-to-strip alignment of the prototype modules built at KIT. The strip-to-strip alignment of each dummy and functional module was within the specification of 400 µrad.

Table 4.2.: Bare module edge and strip-to-strip alignment. The bare module edge alignment combined with the dicing angles of the two sensors yields in the strip-to-strip alignment of the module. Each bare-module built at KIT fulfilled the specifications of a strip-to-strip alignment below 400 µrad.

Module	Edge 1 (µrad)	Strip 1 (µrad)	Edge 2 (µrad)	Strip 2 (µrad)	Edge 3 (µrad)	Strip 3 (µrad)	Edge 4 (µrad)	Strip 4 (µrad)
Dum. Module 1	108 ± 17	100 ± 35	-28 ± 12	49 ± 27	101 ± 18	115 ± 40	54 ± 10	77 ± 25
Dum. Module 2	-8 ± 25	-16 ± 35	-18 ± 12	-4 ± 24	-29 ± 15	-15 ± 34	-45 ± 11	-22 ± 24
Func. Module 1	26 ± 18	17 ± 29	47 ± 12	41 ± 31	49 ± 15	35 ± 29	56 ± 10	49 ± 32
Func. Module 2d	-1 ± 24	4 ± 36	-9 ± 11	-59 ± 28	-43 ± 16	-71 ± 33	-26 ± 10	-26 ± 31
Func. Module 2	126 ± 24	116 ± 35	122 ± 14	120 ± 31	115 ± 16	154 ± 28	92 ± 10	124 ± 26

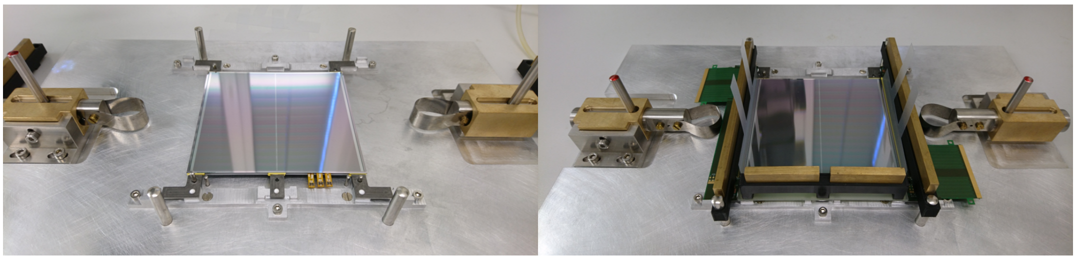

Figure 4.10.: Hybrid gluing of a 2S module. The bare module is placed with alignment pins on an assembly jig. After applying drops of Polytec TC 437 on the exposed Al-CF bridges manually with a pneumatic dispensing gun the SEH can be placed with alignment pins on the front side of the module. The FEHs are aligned manually under a microscope to the sensors strips and are pushed by springs against the bare module.

The third functional bare module, used for the second functional module, had a slightly increased tilt in the strip-to-strip alignment compared to all other of about 120 µrad. With the split measurement of dicing angle (see Table 4.1) and edge alignment it is distinguishable that this arose in the bare module assembly step. It is assumed that one sensor did not have perfect contact to all three alignment pins, although this was checked with a microscope during assembly. This calls for an improvement of the visual validation of the pin contacts during the production phase. The resulting uncertainties on the strip-to-strip alignment are below 40 µrad, which means that the alignment is determined within a window of ±4 µm.

So far only the tilt between the strips was discussed. Shifts orthogonal or parallel to the sensor edge should be less than 200 µm to avoid problems with the HV stability. With the assembly procedure presented, offsets this large are very unlikely and even do not impair the module's functionality. Orthogonal offsets slightly decrease the effective area for the stub finding. Parallel offset can be compensated by applying an additional shift in the stub logic which is done anyway in most of the modules because they are not oriented perfectly perpendicular to the interaction point.

The offset generated by the sensor dicing can be extracted by subtracting the two y-intercept values of the dicing angle fit. Because the dicing of the sensors is a well-controlled process by the vendor it is very unlikely that these values differ by more than 10 µm. Therefore, it is sufficient to evaluate the laser measurements, because it is more likely to introduce an offset due to a bad gluing procedure.

4.5. Hybrid Assembly

The module is read out and operated with two FEHs and one SEH. The assembly of the hybrids to the bare module is done on a dedicated assembly jig shown in Figure 4.10. Polytec TC 437 is applied manually with a pneumatic dispensing gun on the exposed surfaces of the Al-CF bridges. The FEHs are placed on the Al-CF bridges on the left and right side of the module. Two polyimide foils with a thickness of about 100 µm serve as spacers between the bare module and the FEHs. They are removed after curing and ensure a gap while the FEHs are pushed towards the bare module. The resulting gap will later be filled with wire-bond encapsulation material in order to increase the high voltage stability of the module. The alignment of the wire-bond pads between FEHs and the sensor is done manually using a microscope. To ensure a stable wire-bonding process the displacement should not be larger than 90 µm. Applied weights ensure thin and flat glue layers between the hybrids and the Al-CF bridges. The glue has to cure for 24 hours.

Because the development of a final SEH with all functionalities and dimensions is ongoing, substitution parts where used in the prototype modules built. For the very first module a glass-fibre reinforced plastic (GRP) plate was glued to the bare-module. A small printed circuit board (PCB) containing a low pass filter and plugs for the HV tails was attached to it. The HV power supply is connected with cables soldered on dedicated pads. For the second module an improved substitution was developed having the same dimensions and alignment holes as the final SEH. The HV plugs have identical positions as the ones on the SEH for a stress-free connection of the HV tails.

During the production period the SEH is placed with alignment pins on the stump and the two long Al-CF bridges. The SEH has two flex circuits with connectors which are folded and then plugged in the two FEHs for power and readout. The additional fold-over reduces the mechanical stress applied on the plugs and compensates slightly shifted FEHs. The exact procedure of how to glue the service hybrid with its flex circuits overlapping the FEH has to be evaluated as soon as the components are available.

4.6. Readout Wire-Bonding

Each of the 4064 sensor strips is connected to the front-end electronics with a wire-bond. The procedure is done in a semi-automatic bonding machine type Hesse Bond Jet 820. In addition to the readout bonds three additional bias wire-bonds are placed on each sensor corner. The bonding is done on a dedicated jig which is designed to handle the module on both sides without harming previously placed bonds. The module is fixated by applying vacuum with suctions cups on the lower silicon sensor. Additional support rods can be moved upwards below the FEH to prevent resonances impairing the ultra-sonic welding process. The huge number of readout channels and modules to be built per day puts strict requirements on the reliability and stability of the process. Frequent reworking of damaged, missing or weak wire-bonds would cause an inconvenient and almost invincible bottleneck in the assembly line. Therefore, extensive wire-bonding studies are mandatory as soon as more components are available to build modules with the final dimensions.

Considering the large number of modules that have to be built, the wire-bonding process per module including visual inspection should not take longer than one hour. For the first module it took almost three hours to place all wire-bonds. A faulty wire-bond program caused damage on the second module which left it inoperable. Therefore, the readout hybrids were removed and reused in the next module. In the following this module is referred to as the second module. It took almost two hours to place all wire-bonds. A one hour wire-bonding process will only be possible having a highly effective time-management. E. g. the optical inspection of a wire-bonded module has to be made while a second module is currently handled by the machine. The daily workload should at least be separated on two shifts to ensure the staff staying highly concentrated.

4.7. Wire-Bond Encapsulation

Due to the double-sided design of the 2S modules the wire-bonds are exposed on both sides. To avoid mechanical damage by handling during testing, shipping and integration all wire-bonds will be protected with an encapsulation material. Furthermore, the encapsulation protects the wire-bonds from breaking due to resonances in the magnetic field as seen by the CDF experiment at Fermilab and electrochemical corrosion as seen by the innermost pixel detector layer of the ATLAS experiment [Bol+03].

In the scope of this thesis extensive application studies and irradiation tests were performed to ensure a reproducible application and reliable operation. The material used is a silicone elastomer, Sylgard 186 [Cor19].

4.7.1. Application Procedure

For a precise application of the wire-bond encapsulation material the dispensing gantry introduced in Section 4.3 is used. The application procedure developed uses a tapered tip with an inner diameter of 0.41 mm. The two-component material is mixed and filled into a cartridge. Afterwards the gantry calibrates the tip position. Four modules, placed within their carriers, are mounted in the gantry. The application is done in three steps on each wire-bond row. The first step is to dispense a line of encapsulant with 2 ml/mm on both wire-bond feet rows on the sensor and hybrid side. This is done for each module and its two exposed wire-bond rows. Due to its high viscosity the encapsulant needs about 5 to 10 minutes to flow in between and under the wire-bond feet and stops once it has reached the sensor edge or hybrid fold over region. Afterwards a third line with 3 ml/mm is applied on the top of the wire-bond loop. The material merges with the previously applied lines and forms a uniform protection layer along the whole wire-bond row. The pot life of the material is defined as the period in which the viscosity doubles from its initial value and is claimed to be 90 minutes. To get reproducible application conditions the routine should not take longer than 30 minutes to avoid significant changes in the flow behaviour of the material. The automated application procedure for four modules also takes about 30 minutes. The applied material per row is approximately 0.6 g resulting in a total mass of 2.4 g of encapsulant per module, which is about 6 % of a module's mass. More details about the wire-bond encapsulation procedure are given in Appendix B.5.

4.7.2. Irradiation Studies

The wire-bond encapsulation will be used in the 2S module region as well as in the PS module region. Therefore, it has to be radiation hard to up to a fluence of $1 \times 10^{15}\,\frac{\mathrm{n_{eq}}}{\mathrm{cm}^2}$ referring to the radiation damage encountered by the silicon sensors. In addition to this it has to withstand thermal cycles since the tracker temperature will be at about 20 °C during shutdowns and down to $-33\,^\circ\mathrm{C}$ during operation. Any stress applied from the encapsulant to the wire-bonds needs to be excluded.

In the scope of this thesis irradiation studies were performed to test the encapsulant for its radiation hardness, electrical isolation and thermal stress. The test was performed on a silicon dummy module having one row of wire-bonds encapsulated and irradiated with $1 \times 10^{15}\,\mathrm{protons/cm^2}$.

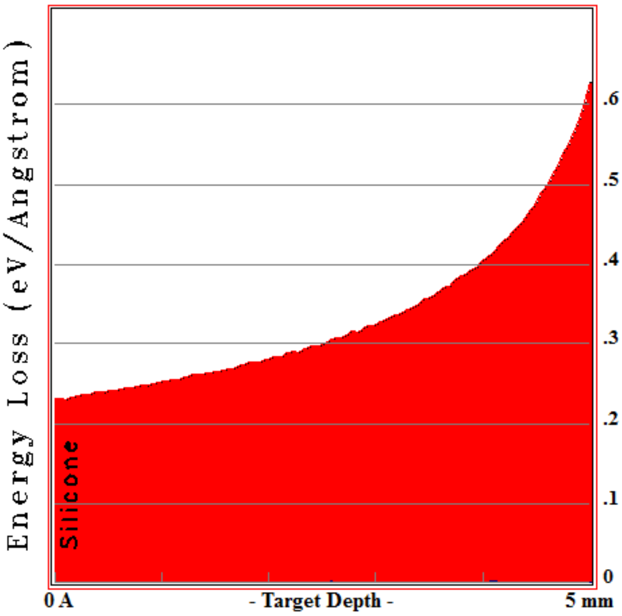

Figure 4.11.: Simulation of the energy loss of 23 MeV protons in silicone. Within 5 mm the energy loss increases from about 0.25 eV/Å to 0.6 eV/Å. The layer of wire-bond encapsulation material is approximately 1 mm high. Therefore, the assumed mean energy loss is at least 0.25 eV/Å.

The irradiation was done at a cyclotron delivering protons with an energy of 23 MeV. A tool calculating the stopping ranges of ionizing particles in matter (SRIM [Zie19]) was used to estimate the applied dose in the silicone elastomer. As shown in Figure 4.11, the energy loss per Å is estimated to be at least 0.25 eV for a 23 MeV proton on the first 1 to 2 mm of silicone material. With the deposited fluence of 1×10^{15} protons/cm² and a material density of $1.12\,\mathrm{g\,cm^{-3}}$ the approximate applied dose results to

$$D = \frac{\frac{\text{Protons}}{\text{cm}^2} \cdot \frac{\text{Energie deposition}}{\text{cm}\cdot\text{Proton}}}{\text{Material density}} = \frac{\frac{10^{15}\,\text{Protons}}{\text{cm}^2} \cdot \frac{25\cdot 10^6\,\text{eV}}{\text{cm}\cdot\text{Proton}}}{1.12\,\mathrm{g\,cm^{-3}}} = 3.57\,\mathrm{MGy}. \tag{4.1}$$

An equal irradiation of silicon would deposit a total ionizing dose of about 2.8 MGy, and a fluence of $2 \times 10^{15}\,\frac{\mathrm{n_{eq}}}{\mathrm{cm}^2}$, which is twice the expected value in the PS module region. The total ionizing dose expected to be deposited in the silicone elastomer in the experiment is 900 kGy. Therefore, the applied dose in the silicone elastomer is assumed to be sufficiently high to test the integrity of the wire-bond encapsulation after the full module lifetime. The irradiation was part of a measurement routine checking the wire-bond functionality under various conditions. As shown in Figure 4.12, the electrical connection of the wire-bonds was tested between the AC pad on the center region of the sensor and the bump bond pad of the CBC using probe needles. The integrity of the electrical connection of 508 out of 1016 wire-bonds were tested after each of the following steps:

- Thermal cycles: 20 times from +20 °C to −20 °C
- Wire-bond encapsulation with Sylgard 186
- Thermal cycles: 20 times from +20 °C to −20 °C
- Irradiation with 3.57 MGy using 23 MeV protons

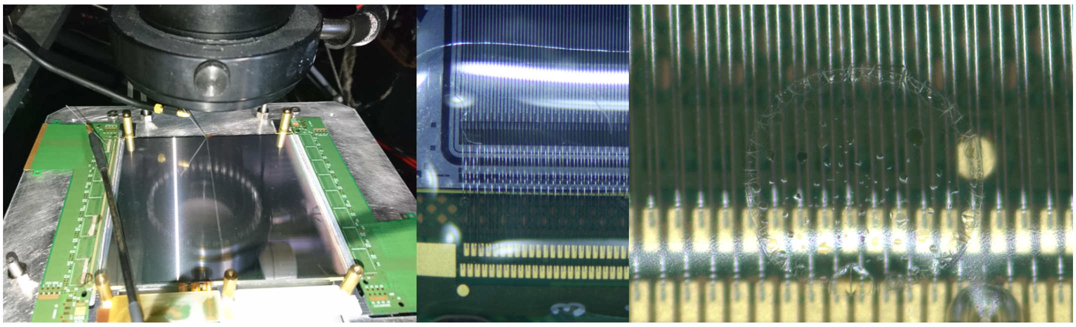

Figure 4.12.: With probe needles on the AC pad in the mid sensor region and the CBC bump bond pad the resistance of the tested wire-bond is measured to be zero (left). The silicone elastomer protecting the wire-bonds turns from shiny (middle) to blurry (right) after an irradiation of 3.57 MGy. Halos of small cracks emerged on the materials surface.

- Thermal cycles: 20 times from +20 °C to −20 °C

Not a single wire-bond connection was lost during the measurement campaign. Figure 4.12 also shows a close up picture of the silicone elastomer before and after the irradiation of 3.57 MGy. Halos of small cracks emerged on the material's surface. Additionally, the surface switched from being shiny to blurry. But due to the electric functionality of the wire-bonds and the intactness of the material as a whole this is not seen to be a problem.

With these results the usage of Sylgard 186 as wire-bond encapsulation material in the Outer Tracker is verified.

4.8. I(V) Measurements during Module Assembly

For a well-functioning module, the assembly process should not impair the sensor performance. As stated before, during the production phase 5 % of all sensors will be electrically qualified in the SQCs. Then, the $I(V)$ characteristics of all sensors will be measured after the backside isolation and attachment of the HV tail. Once the hybrids are attached and wire-bonded, the $I(V)$ curve of the module is measured before and after the wire-bond encapsulation.

During the prototyping phase additional steps are included. After initially measuring the complete sensor characteristics in a probe station an $I(V)$ curve is measured after each of the following assembly steps:

- The backside isolation with polyimide strips and HV tail gluing and encapsulated wire-bonds. Done on the HV / I(V) test system introduced in Section 4.3.3.
- The bare module assembly. The bare module is placed on its aluminium carrier, which is in return placed in the probe station to contact the bias rails with a probe needle.
- The hybrid gluing. Same procedure as with the bare module.
- The readout wire-bonding. In the module readout station introduced in Section 4.9.1.
- The readout wire-bond encapsulation. In the module readout station.

Figure 4.13 shows the $I(V)$ characteristics of the first three prototype modules built at KIT. The $I(V)$ curves of the first module built did not change their shape during the assembly process but are shifted with respect to each other. As stated in Section 3.3.1, the sensor current

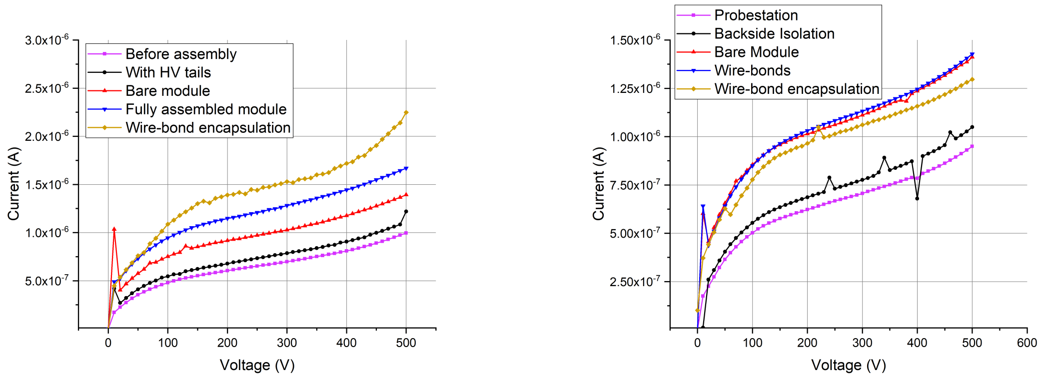

(a) Module 1 - Top sensor

(b) Module 1 - Bottom sensor

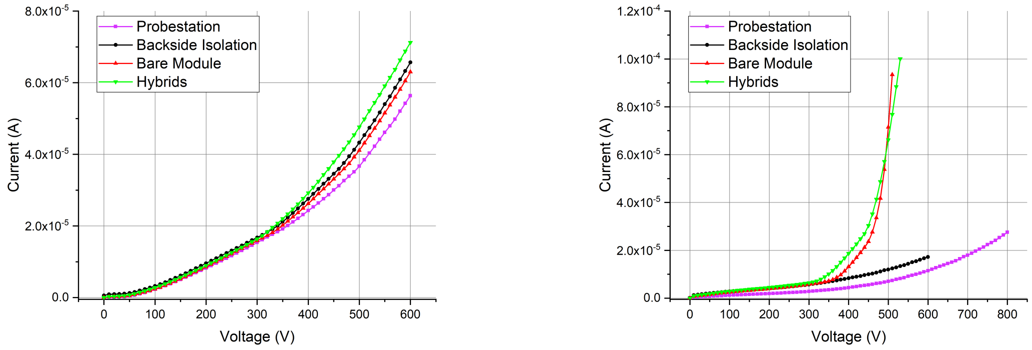

(c) Module 2 - Top sensor

(d) Module 2 - Bottom sensor

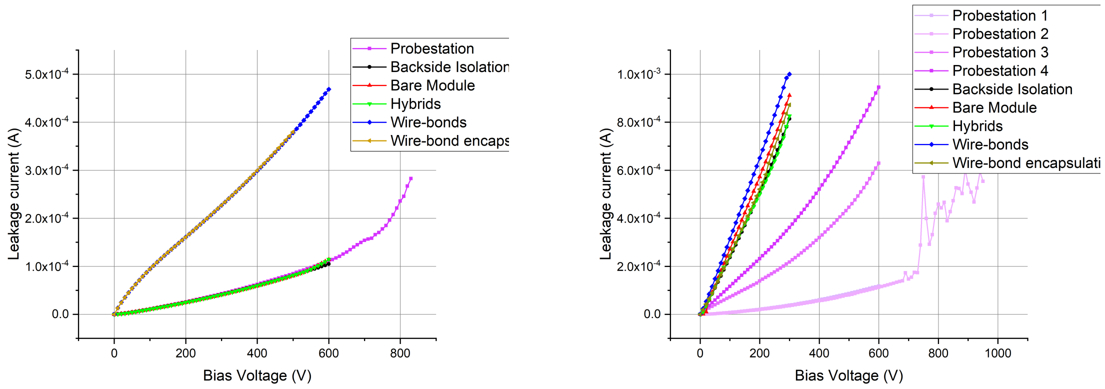

(e) Module 3 - Top sensor

(f) Module 3 - Bottom sensor

Figure 4.13.: $I(V)$ curves of the prototype modules built at KIT. The first module did not show an altered behaviour, despite shifts caused by different sensor temperatures. In the second module the $I(V)$ of the bottom sensor changed its shape indicating a possible issue in the assembly process. The third module, containing sensors with an initially high leakage current also showed a change of their $I(V)$ curves during the assembly process.

depends on the temperature. For the first measurement the sensor rests on a temperature stabilized jig at 20 °C. The $I(V)$ curve after the backside isolation was also measured within the probe station, because the HV/I(V) test station was not available at this time. A PTFE foil was placed between sensor and jig, explaining slightly higher temperatures. The following two measurements on the bare module and final module did not allow a temperature stabilization because the module was placed in its carrier, having the temperature of the environment. Also the module readout station introduced in Section 4.9.1 was not available at this time.

The second module showed an increased current on the bottom sensor after the bare module assembly. The origin is not understood but possible reasons are a contamination with unknown residues on the sensor, a scratch on the sensor surface or other damage unintentionally caused during handling. Even with an intensive cleaning of the sensor edge and an optical inspection the origin of the current increase could not been identified. The top sensor shows variations at higher voltages which can be explained by different sensor temperatures during the measurements.

The third module contains 2S sensors with an initially very high leakage current. These $I(V)$ curves hint at severe damage before the assembly started. During module assembly the current further increased, but due to their overall bad condition an exact estimation of the origin is not possible.

The measurements shown in Figure 4.13 demonstrate the importance of measuring the $I(V)$ characteristics during the module assembly in the prototyping phase. This will be of more interest once the sensor type and quality is equal for each prototype built, which simplifies conclusions about possible origins of damage.

4.9. Module Qualification and Measurements

Figure 4.14 and Figure 4.15 show the first functional modules built at KIT. After the assembly of the module prototypes, they are qualified on several characteristics such as front-end noise, $I(V)$ curves and source measurements. In the scope of this thesis the development of a dedicated temperature-stabilized module readout station was supervised and is described in detail in [Kop18].

4.9.1. Module Readout Station

Prototype modules and final modules can be investigated in a temperature-stabilized and dark environment provided by the module readout station. As shown in Figure 4.16, the module resting on its aluminium carrier lies on a cooling jig in a light-tight box. The temperature on the carrier is stabilized with a two-staged cooling system using a chiller constantly keeping a pre-cooling copper block on about −10 °C. Between the pre-cooling block and the copper jig on which the carrier lies are four Peltier elements installed to provide an adjustable temperature on the carrier between −35 °C and +30 °C. Due to the cold temperatures inside the box it is flushed constantly with dry air to avoid water condensation on sensitive parts. A controllable valve can accelerate the cooling process if needed by increasing the dry air flux significantly. With a bypass on the cooling circuit the coolant flow through the box can be stopped and the heating process can be accelerated.

The module mounting mechanism is designed to ease the module installation and removal as far as possible. By putting down a lever containing pushing springs the carrier is pressed on the cooling jig ensuring a good thermal contact. The usage of screws was not seen to be feasible due to an increased possibility of accidents during the mounting procedure. The box's walls contain additional lead inserts to minimize the emission of ionizing radiation outside the station during a measurement with a radioactive source, which can be mounted above the module on the fixation lever. Below the module a 15 cm×15 cm large plastic scintillator serves

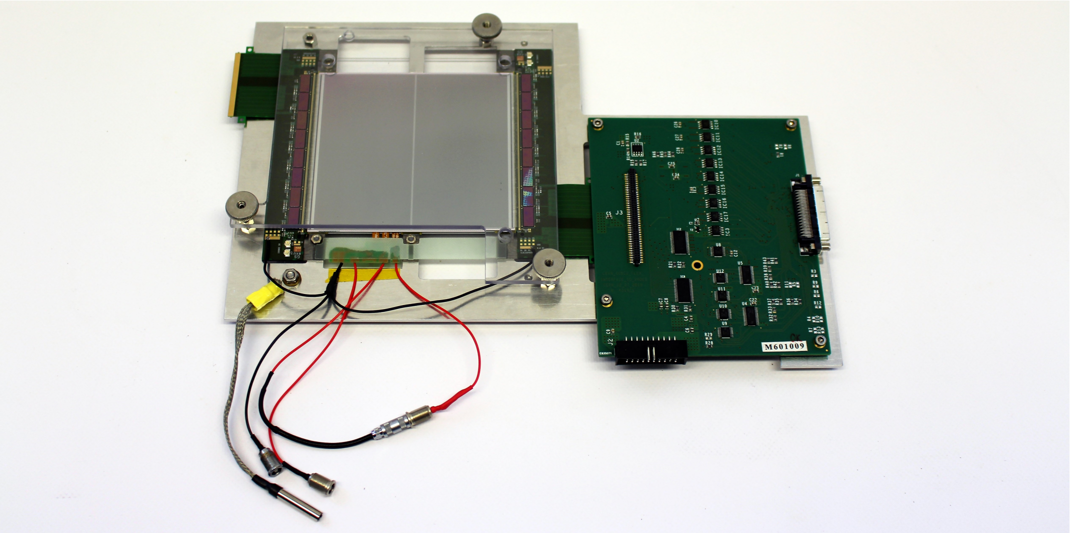

Figure 4.14.: First functional 2S module built at KIT. Due to the lacking SEH small filter circuits are used as substitutions. Only one side of the module can be read out at a time with an attached interface board resting on the same carrier as the module.

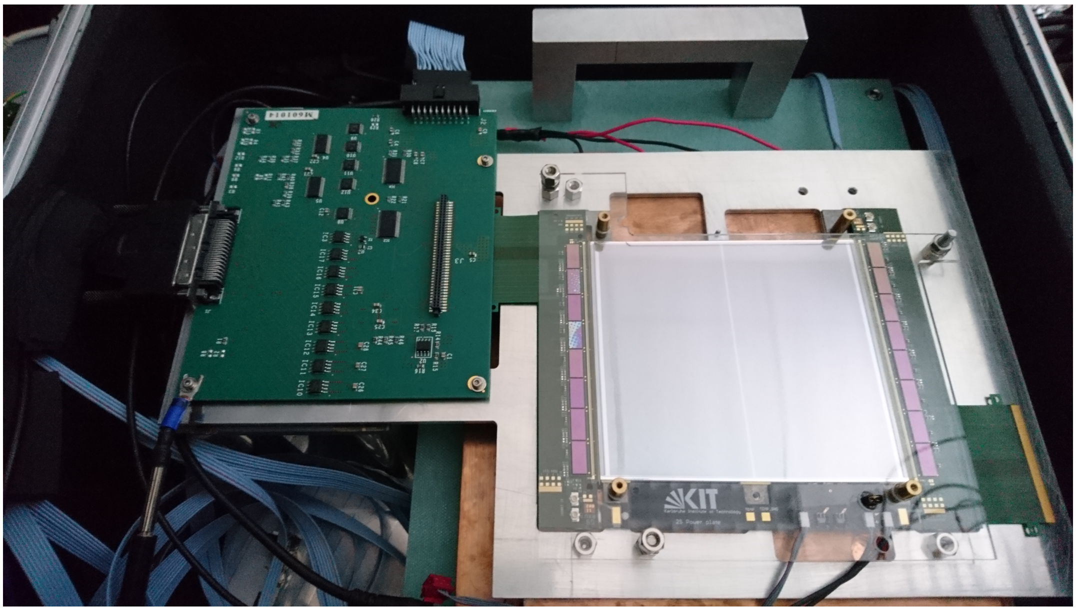

Figure 4.15.: Second functional 2S module built at KIT. A substitution for the SEH, a plate containing the high voltage filter circuit having the same dimensions as a SEH was used. On the image the module rests in its carrier and is placed inside the module readout station.

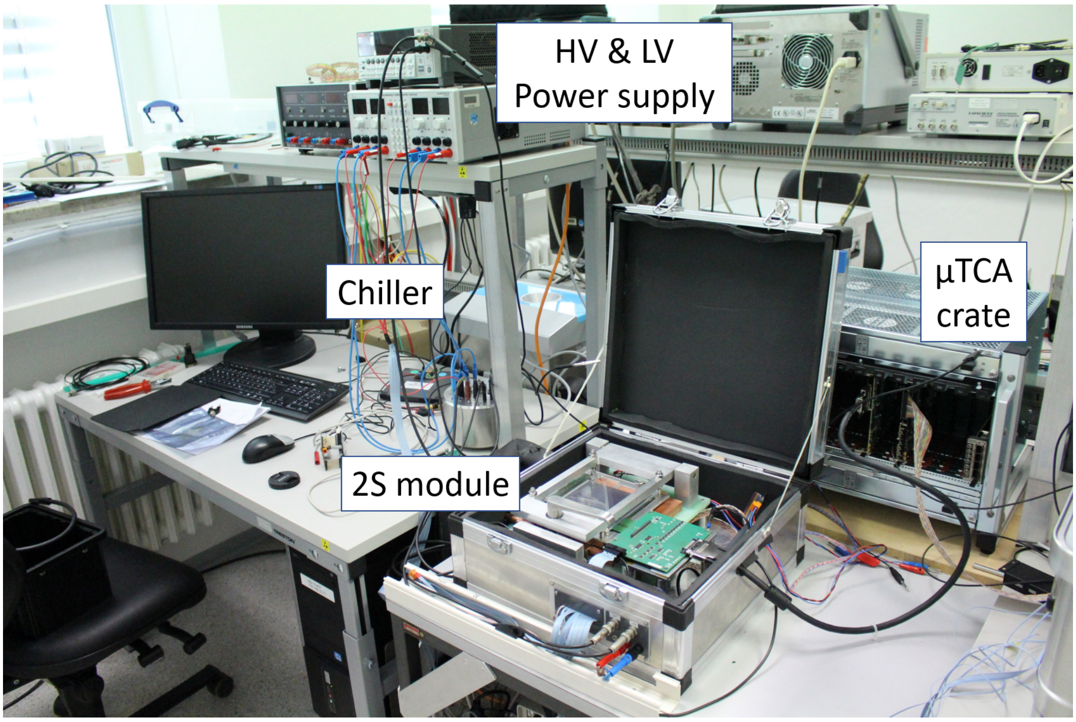

Figure 4.16.: Temperature stabilized 2S module readout station. The modules are placed within a light-tight box on a cooling jig whose temperature is stabilized with Peltier elements and a chiller serving the pre-cooling. Two power supplies deliver the low and high voltage for the module operation. The readout is done via an FPGA board located in a µTCA crate.

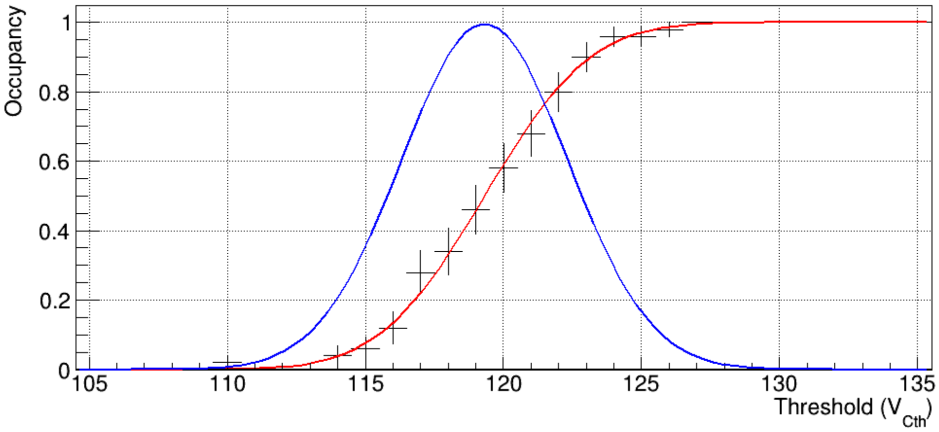

Figure 4.17.: Noise measurement of a single channel on a CBC2. By lowering the threshold, which means increasing the V_{Cth} values, the occupancy rises from 0 to 1 according to a Gaussian error function (red). The width parameter σ of its derivative, a Gaussian function (blue), is defined to be the noise. The pedestal value of this channel is 119 V_{Cth} and the noise is 3 V_{Cth}.

as trigger source. The signal is routed outside the box to the readout board. A high voltage power supply for the sensor and a low voltage power supply for the front-end electronics is needed to operate the module.

The dry air flux valve, the high voltage power supply, the Peltier elements, the temperature and humidity sensors are controlled and read out with custom C_{++}-based software including a GUI for convenient use. The software also handles the modules communication via middleware called Phase 2 Acquisition and Control Framework (Ph2_ACF) [CMS19a]. The Ph2_ACF is introduced in more detail in Section 5.2.3. It communicates with the readout board based on the Xilinx Kintex 7 FPGA technology, called FC7 [Pes+15]. The FC7 runs the dedicated firmware to communicate with the readout hybrids. A transition board is directly connected to the front-end hybrid as a substitute for the SEH. It distributes the signal lines and power voltages and will be obsolete for modules built with final components.

With the module readout station developed it is possible to characterize the performance of prototype modules and final modules at temperatures as within the CMS detector.

4.9.2. Noise Measurements

One of the most important quantity to operate a silicon detector is the noise on the analogue front-end electronics. Low noise increases the sensitivity for small signals and thus the detector efficiency.

Due to the binary output of the CBC the noise is derived from a threshold scan meaning that the channel's occupancy is measured while the threshold is increased. The threshold voltage of the comparator can be adjusted stepwise in DAC counts called V_{Cth}. In case of the CBC2 this is encoded by 8 bits, having 256 possible steps. The CBC3, as it is used in Chapter 5, has a 10 bit encoding resulting in 1024 steps. Due to the electron readout, higher V_{Cth} values represent lower thresholds. The noise measurement of a single channel on a CBC2 is shown in Figure 4.17. By lowering the threshold the occupancy increases from 0 to 1 according to an error function. The threshold value with a corresponding occupancy of 0.5 is called pedestal. The width parameter σ of the error function's derivative, a Gaussian function, is defined to

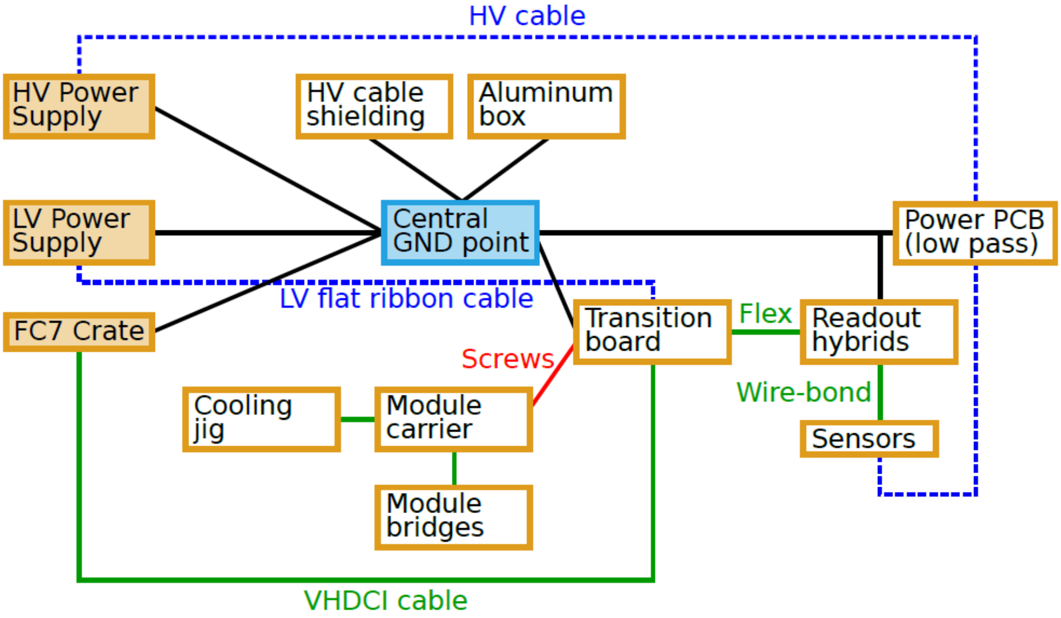

Figure 4.18.: Star-like grounding scheme for the 2S modules. The basic principle is to ground all parts at a central grounding point. Black lines represent grounding connections while the blue lines are low and high voltage transfer lines. The green connections are predefined for readout and cannot be changed.

be the noise on the analogue front-end. To avoid noise hits on the front-end impairing the tracking, the threshold for particle detection is set to a value which is at least five times higher the noise. Based on Gaussian statistics this means that only once in 1.7 million readouts a channel detects a hit caused by noise.

A well-defined grounding scheme is crucial for low noise on the module. Therefore, a star-like grounding scheme shown in Figure 4.18 was developed for the module readout station avoiding grounding loops as much as possible.

Bias Voltage

The noise on the analogue front-end of a CBC channel is mainly driven by the thermal noise on the attached strip capacitance of the silicon sensor. When fully depleted, a single strip with a length of about 5 cm has a capacitance of 9 pF resulting in a noise of about 1000 e^-. The strip capacitance decreases with the bias voltage as long as the bulk is not completely depleted.

The bias voltage should be high enough to fully deplete the silicon sensor, to have low noise and a maximized volume to detect signals. By measuring the noise depending on the bias voltage the operation voltage of the module can be determined. In Figure 4.19 this measurement is shown for both modules built. The noise is measured on one readout hybrid while the bias voltage is increased. Due to the high leakage current of the second module's sensors the measurement ends at 230 V. The saturation of both curves happens above 150 V. The operation voltage for the first module is set to be 300 V and 230 V for the second, to have enough margin to be well above the depletion voltage.

Noisy Channels

Figure 4.20 shows the noise distribution of all 4064 channels of both modules at room temperature of (about 23 °C). In case of the prototype modules, both hybrids have to be connected

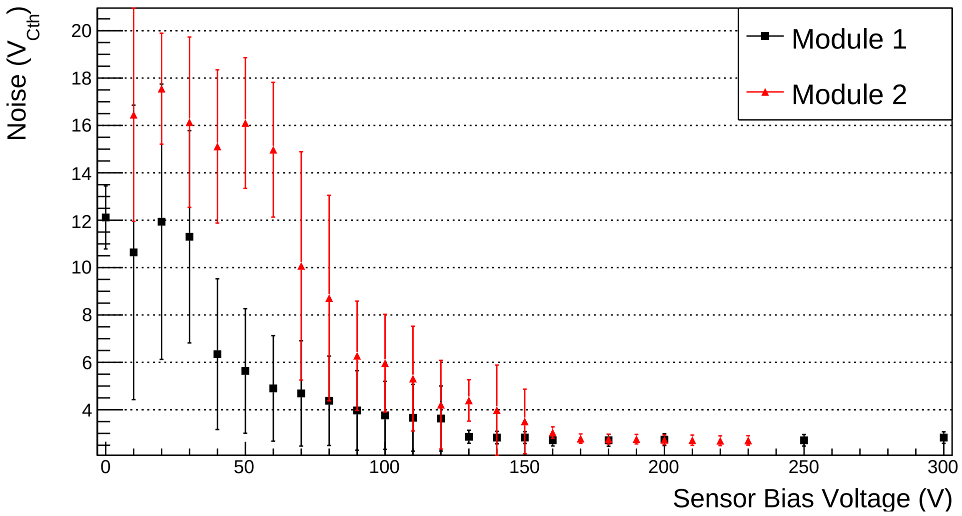

Figure 4.19.: Mean noise on one front-end hybrid depending on the applied bias voltage of the two modules built. The error bars represent the root mean square of the distribution. Between 150 V and 200 V the noise on both modules reaches its minimum.

individually to get the average noise of the whole module. The two modules have a mean noise value of about 2.7 V_{Cth}. With a translation factor of 320 e^- per V_{Cth} as derived in [Dee17] this is equivalent to about 860 e^-.

On the first module three channels show an increased noise value. Taking a closer look, a scratch was found on the top sensor that crosses about ten channels including these three. A following test pulse measurement revealed an electric connection between the three channels. By injecting a test pulse in one channel it also turns up in the other two. Therefore, the increased noise is reasonable due to the higher capacitance attached to each channel. A signal arriving on one of the strips spreads with lower amplitude on all three channels decreasing the probability to exceed the threshold set on the channel's comparator. Therefore, the channel's efficiency for detecting signals is decreased.

The second module shows more noisy channels, which is expected due to the bad conditions of the attached sensors. Nevertheless, all conspicuous channels can be linked to damage on the sensor surface caused by accidents in the probing procedure or handling. This reasserts that a carefully handling of the silicon sensors is mandatory for the module production.

Sensor Temperature

The module readout station is temperature stabilized using a two-staged cooling circuit. The monitoring of the temperature is done with four thermal resistors read out by a custom-made PCB board. Peltier elements between the pre-cooling block and cooling jig holding the module carrier control the temperature. Unfortunately, as shown in Figure 4.21, turning on the cooling circuit including the temperature readout PCB and Peltier elements increases the noise on both modules. This effect is larger for the first module compared to the second. It is assumed that the grounding of the second module is improved because wire-bonds instead of solder joints was used to connect the HV ground with the hybrid ground.

Afterwards, the temperature is reduced in steps of 5 °C while the noise on the hybrid is measured. The temperature is measured with the thermistor included on the HV tail of the top

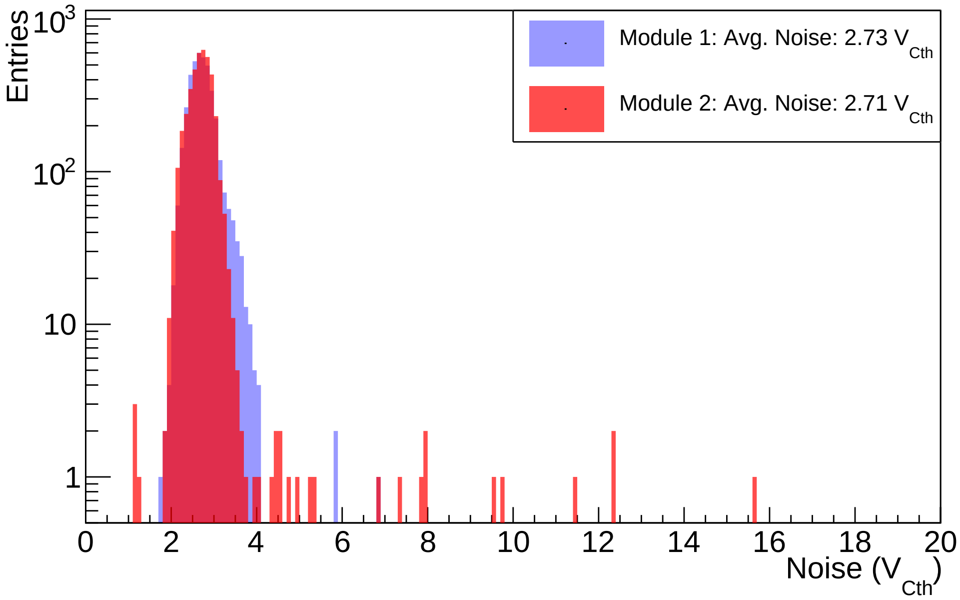

Figure 4.20.: The average noise at room temperature of all channels of the two modules built. The value of 2.7 V_{Cth} is equivalent to about 860 e^-. The bias voltage was 300 V for the first and 230 V for the second module.

sensor. It is assumed that the increased power consumption of the Peltier elements at lower temperatures impacts the noise of the front-end channels. For the first module the resulting noise levels impair the particle detection at reasonable threshold levels. In case of the second module reliable data taking is possible even at lower temperatures because the noise remains in a region of about 3 V_{Cth}.

The studies show that it is possible to build and operate 2S modules with low noise. Nevertheless, they also indicate that a proper grounding scheme and a well-controlled environment is crucial for the modules' operation.

4.9.3. Module I(V) Curves

As described in Section 3.3.1, the leakage current of silicon sensors is mainly depending on irradiation, temperature and bias voltage. To further characterize both functional prototype modules $I(V)$ curves at different sensor temperatures are measured and are shown in Figure 4.22. As expected, the current decreases with temperature and voltage.

In the final module design it will not be possible to measure the $I(V)$ curve separately for the bottom and top sensor because both sensors will be biased via the same power connection. This makes the trouble shooting of fully assembled and faulty modules more difficult. Therefore, the prototype modules built contain a filter circuit in which the electric connection of the sensor can be established either separately or in common. The temperature is measured on the thermistor of the HV tail of the top sensor.

The $I(V)$ curves of the first modules behave as expected. They keep their shape and decrease with temperature. The $I(V)$ curves of the second module are almost not affected by the decrease of temperature. This hints at the origin of the high leakage current not coming from the silicon bulk. It is assumed that some damage on the sensor's periphery causes a low resistant connection resulting in the high leakage currents.

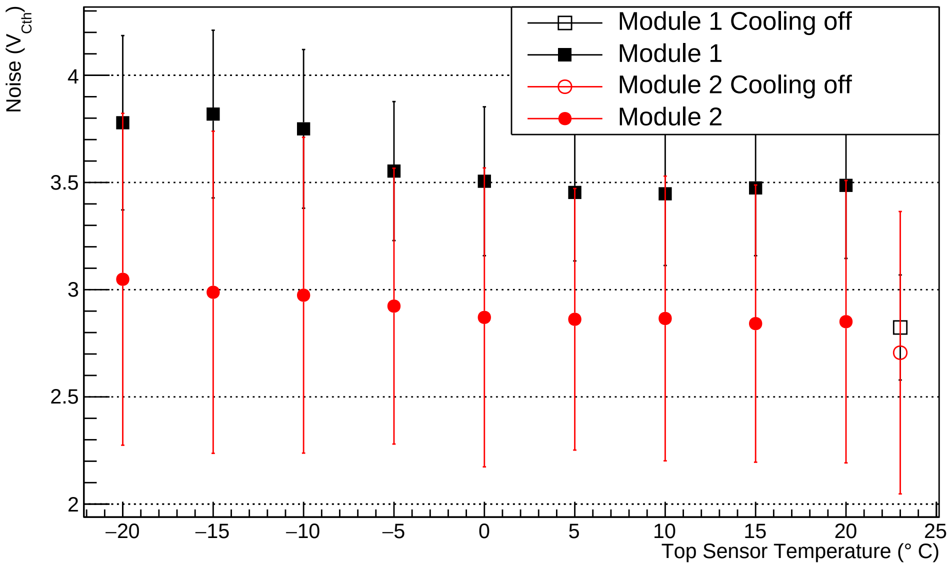

Figure 4.21.: Temperature dependence of the average noise levels on all channels of one hybrid for the two modules. The temperature was measured on the HV tail thermistor of the top sensor. The error bars represent the standard deviation of the distribution.

4.9.4. Source measurements

The final test performed on the prototype modules is done with a ^{90}Sr source placed above the silicon sensor. The electrons emitted by the source are detected by the sensor generating a Gaussian-shaped hit profile. As shown in Figure 4.23a the top sensor detects more electrons compared to the bottom sensor because part of the emitted electrons are stopped in the top sensor. The measurement is performed with a random trigger, meaning that there is no correlation between electrons generating a signal in the sensor and the trigger signal. The hit detection of such a particle is therefore random and the hit count depends on the trigger frequency and emission rate of the source.

A second measurement tests the stub output of the module. The chips and firmware can be configured to trigger on detected stubs in the front-end. Stubs are only created by particles crossing both silicon layers. Therefore, the resulting hit profile should be nearly identical for both sensor layers as visible in Figure 4.23b.

4.10. Module Qualification during Production

During the production phase up to eight modules will be assembled per day. Each module is tested before and after the wire-bond encapsulation resulting in 16 module tests per day that have to be performed in a single module test station. Therefore, the module testing should not take longer than 30 minutes. To fully guarantee the functionality of the module the $I(V)$ characteristics of the sensors have to be tested as well as the noise of the front-end. A grading scheme to group modules according their performance in terms of leakage current or number of broken, noisy or faulty channels has still to be evaluated.

Each module will be tested at room temperature in a single module readout station. For this, a collaboration-wide test routine has to be defined, which can be controlled with a simple

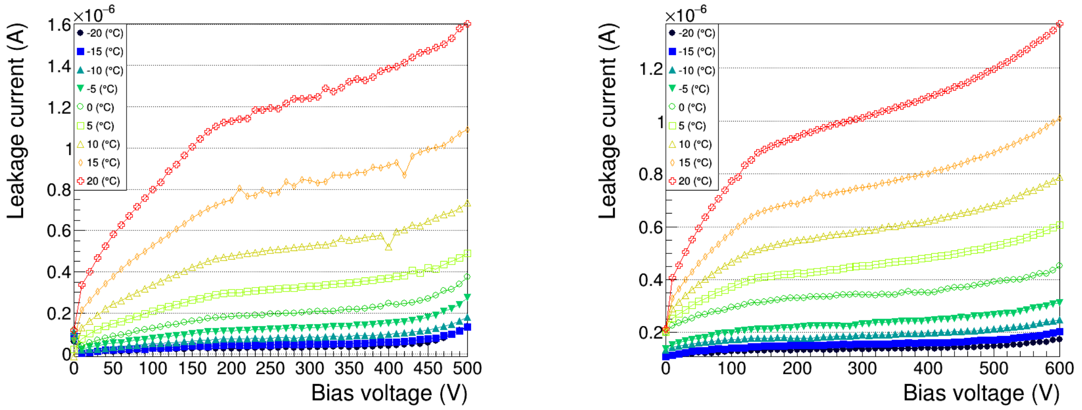

(a) Module 1 - Top sensor **(b)** Module 1 - Bottom sensor

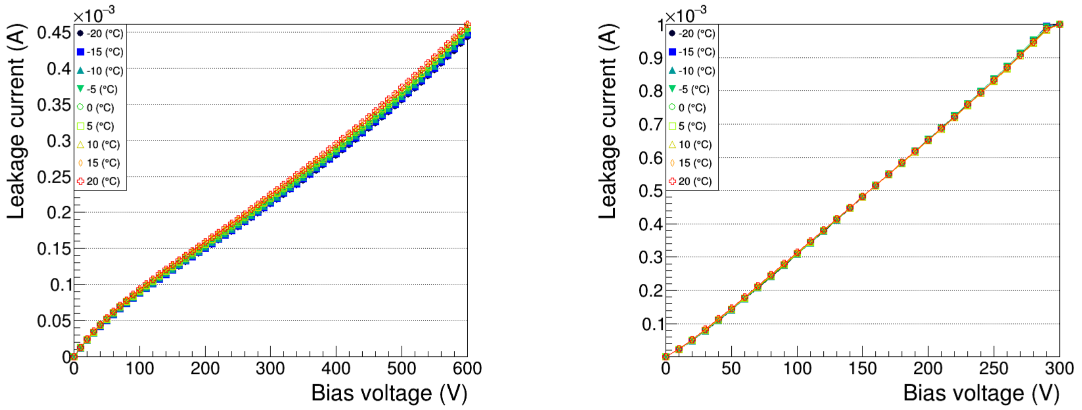

(c) Module 2 - Top sensor **(d)** Module 2 - Bottom sensor

Figure 4.22.: Temperature dependent $I(V)$ curves for the modules built at KIT. The measurements are performed separately for the top and bottom sensor. As expected the current decreases with voltage and temperature. Due to the bad conditions of the sensors used in the second module the temperature dependence is almost not visible.

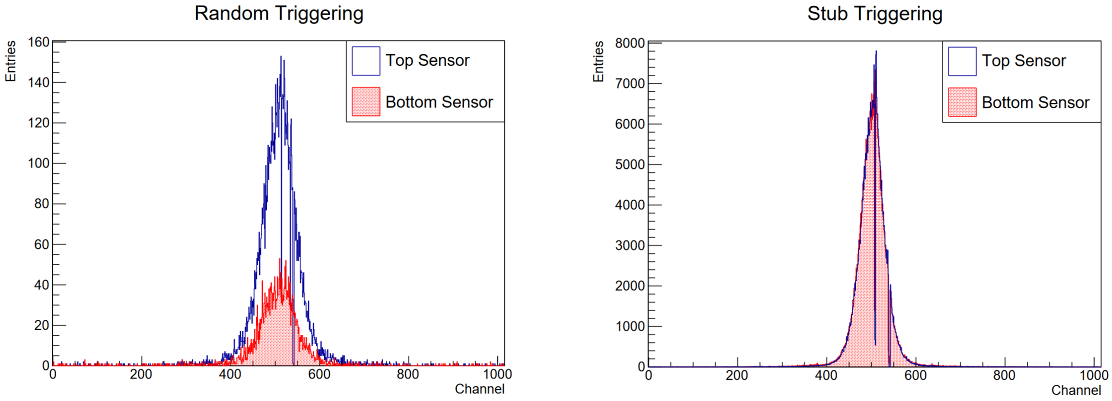

(a) Random triggers

(b) Stub triggers

Figure 4.23.: (a) ^{90}Sr measurement with random triggers. A fraction of the particle is stopped in the first layer and does not reach the second sensor. Therefore, the top sensor detects more hits. (b) ^{90}Sr measurement triggered on stubs. Because a stub is only created by particles crossing both sensor layers the hit profiles of top and bottom sensor are nearly identical.

GUI. In addition to this all modules are tested in a burn-in station. Within this station up to eight modules are tested for at least two days and undergo at least 20 temperature cycles between −20 °C and 20 °C. Depending on module distribution paths this test is either at the assembly or the integration site.

All measurements performed on the module and its components have to be tracked by the construction database. This requires further developments to keep the usage as handy as possible for the staff building the modules and characterizing their properties.

4.11. Summary Module Assembly

This chapter describes the assembly and test procedures to build 2S modules for the CMS Outer Tracker. A metrology station was developed, constructed and programmed to measure the dicing precision of 2S sensors and the strip-to-strip alignment of bare modules. With a custom-made dispensing gantry a gluing procedure was developed to reliably apply the polyimide isolation to the sensor's backside, with almost perfect wetting, thin glue layer thicknesses and no excess of glue. The development of a temperature-stabilized test station was supervised, with which it is possible to characterize the behaviour of the modules at low temperatures. Irradiation studies of silicone-based wire-bond encapsulation material verify its usage in the Outer Tracker.

In 2018 ETP was the first production centre to build a functional module outside the pilot centre CERN. A second functioning module followed in 2019. Both modules can be operated at low front-end noise levels to detect particles emitted by a ^{90}Sr source.

Most of the components used to assemble a 2S module are still under development. Therefore, the development of the assembly process will be ongoing as long as the components do not have their final design and functionalities. By the end of 2019, the production sites will be handed out the first functional versions of the SEH and FEHs including CBC3s. In addition to this, an extension mezzanine board containing the first version of the CIC can be plugged into this FEHs. This will result in the first prototype modules which resemble the same electric functionality as a final 2S module.

5

High Rate Tests of the CMS Binary Chip DAQ Chain

The detector components deployed in the future CMS Outer Tracker have to fulfil several requirements before they are approved for usage. One of these requirements is the operability under high rate conditions. Various simulations have been performed to understand the conditions in the future Outer Tracker [CMS18]. The bunch crossing rate of the LHC will remain at 40 MHz and the pile-up can reach a mean value of up to 200 inelastic collisions per bunch crossing. The resulting hit occupancy based on the granularity of the PS and 2S module is shown in Figure 5.1 and reaches a maximum of about 1 % for 2S modules.

In the scope of this thesis a system was developed to test the high rate operability of the 2S module readout chain. This chapter describes in detail the requirements for the system, its commissioning and first results. Due to the ongoing development of the readout electronics solely the first part of the readout chain, the CBC, could be tested. Future upgrades of the system will expand the readout chain with the CIC, LpGBT and VTRx+, which were introduced in Section 3.3.2 and Section 3.3.2.

The measurements presented in the following mainly focus on the efficiency of the CBC to detect injected signals and the resulting stubs at high trigger and hit rates. In addition to this, the effect of signals generated in previous bunch crossings on the efficiency as well as the noise behaviour under these conditions are discussed. Several tests are made in which different parameters are varied:

- Efficiency depending on the track density / occupancy
- Efficiency and chip behaviour depending on trigger rates
- Stub finding efficiency depending on the inclination angle of particles
- Noise behaviour depending on the track density / occupancy
- Efficiency depending on decreased cluster signals to emulate irradiation levels on the sensor

All tests are performed under high hit and trigger rates. Those measurements could so far not be performed with usual laboratory or beam tests.

5.1. Motivation / Status Quo

Usual tests to characterize the operability of silicon detectors involve beam lines on accelerators or radioactive sources as shown in Figure 5.2. In terms of types of particles interacting with the detection material, beam tests are closest to the environment of the running experiment. Accelerated particles pass multiple planes equipped with silicon pixel modules, called telescope, before and after the device under test. With the telescope the trajectories of the traversing particles are reconstructed. For an efficiency measurement, it is checked whether the device

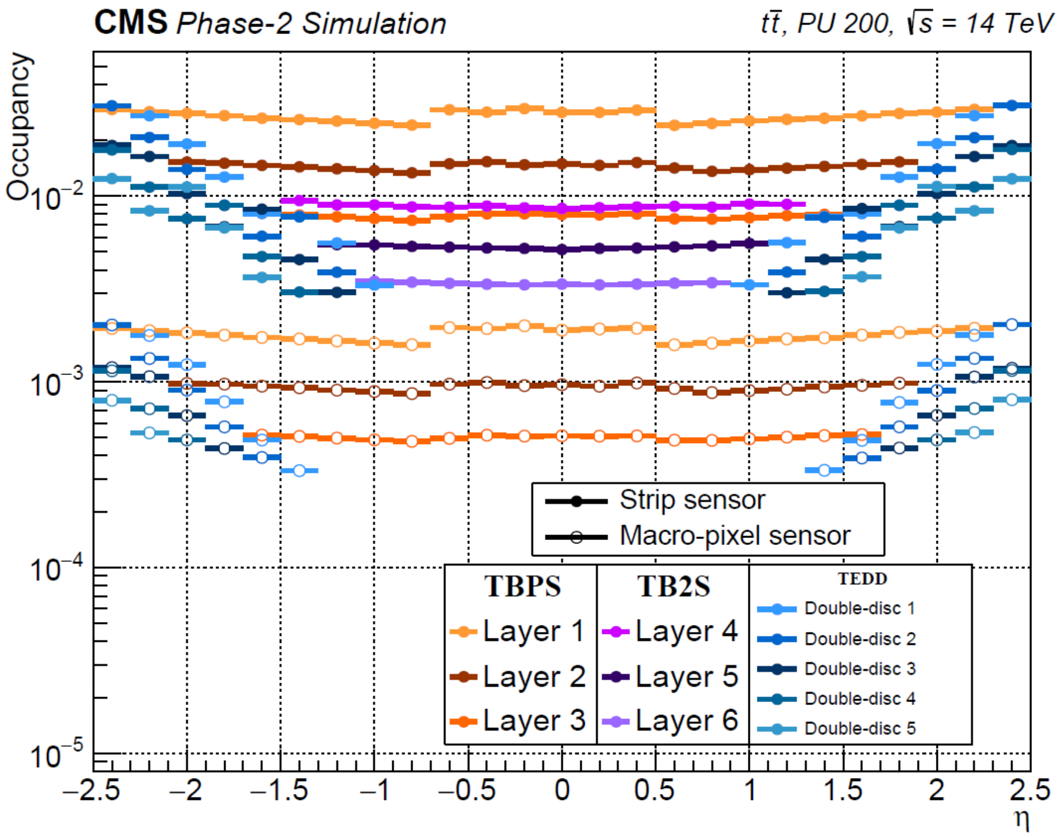

Figure 5.1.: Simulation of the hit occupancy within the Outer Tracker depending on η and the module type. 2S modules deployed in the TEDD have the highest hit occupancy at $\eta \approx 2.5$ of about 1 % [CMS18].

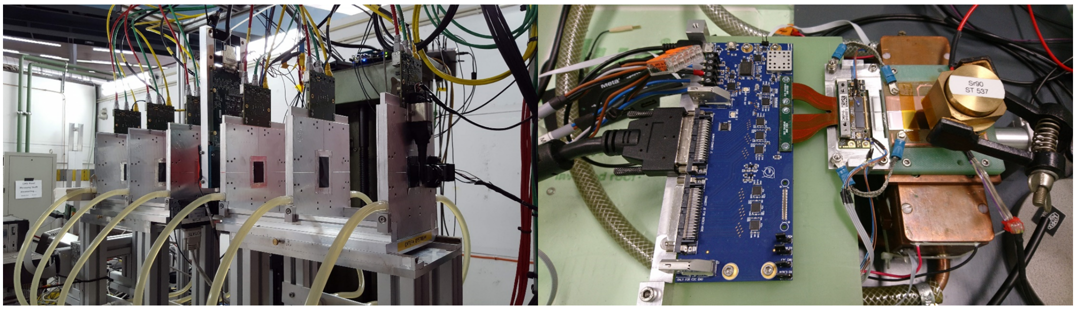

Figure 5.2.: Measurement systems used to test silicon detectors. In a beam test an accelerator beam is directed on a device under test. Before and after the device the particles are tracked with a telescope for efficiency measurements (left). With a radioactive source such as ^{90}Sr the signal collection of silicon detectors can be measured (right).

under test records the particle at the expected position. Most beam lines cannot deliver a particle density comparable to the environment in the future Outer Tracker. Also the trigger rates are often limited by the telescope readout, which does not cope with particle densities up to 15 MHz/cm^2 and trigger rates of up to 750 kHz. Within the CMS collaboration the mostly used beam test facilities are the CERN SPS North Area, Fermilab and DESY II [Eng19] [Fer19] [Deu19].

Depending on their size and activity, radioactive sources can have a high particle emission rate. Unfortunately, the particles' energy is on average not high enough to allow tracking with several layers of silicon sensors. Therefore, position related efficiency studies on detector systems are not possible with radioactive sources. Usual test systems, as shown in Figure 5.2, use a scintillator placed below the detector to trigger passed particles.

To summarize, the available test systems do either not fulfil the particle rate or tracking requirements to test the detector efficiency under high rate conditions characterised by a high, known signal rate on the front-end in combination with a high trigger rate. This calls for a new test system.

5.2. The KArlsruhe high RAte TEst system: KARATE

A new test system was developed in the scope of this thesis to validate the high rate operability of the 2S module readout chain, called KARATE, which stands for KArlsruhe high RAte TEst.

5.2.1. Requirements

The generation of high rate signals on a silicon strip sensor, e.g. with with particles, seems not to be practicable. Instead, the system should emulate signals coming from a silicon strips sensor. The requirements that have to be met by the new system are:

- Controllable generation of unipolar pulses
- Pulse rise time below 20 ns, which is the rise-time of the CBC's analogue front-end
- Capability to run constantly at 40 MHz
- Low noise on the front-end

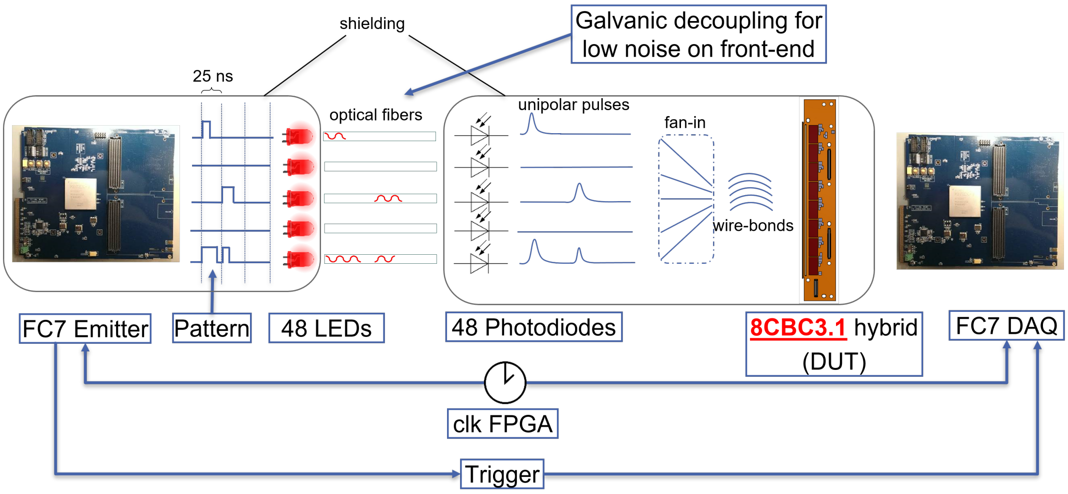

Figure 5.3.: Schematic of the KARATE working principle. An emitter FC7 board controls 48 LEDs generating light patterns at 40 MHz. The light patterns are routed via optical fibres on 48 photo diodes, each of which is AC-coupled to a CBC channel. The light arriving on the photo diodes generates a unipolar pulse that is subsequently injected into the CBC channel. The light pulse length of the LED is adjustable in steps of 3.125 ns causing different resulting signal amplitudes on the CBC channel.

Using a voltage drop on a capacitor is not seen to be feasible because it has to be charged every once in a while. Such a system is not able to run constantly on 40 MHz. Concerns about the additional noise reasserted the abandonment of using capacitors.

Instead, the combination of a LEDs and photodiodes is chosen which fulfills all requirements. The signal generation in the photodiodes is also based on a sensitive pn-junction comparable to a strip sensor. This combination has the additional advantage that it galvanically decouples the emitting system from the injection system, reducing the risk of coupling additional noise into the front-end.

5.2.2. Setup

Figure 5.3 shows the working principle of the KARATE system. Two FC7 boards are used to generate the signal patterns and to read out the data of the front-end electronics. The FC7 emitter board stores a list of patterns on its internal memory. Each 25 ns a signal pattern is sent to an array of 48 LEDs. The light pulses generated are routed via optical plastic fibres on 48 photodiodes. The resulting unipolar pulses reach the front-end of a CBC channel via AC-coupling. For this the injection board is wire-bonded to the channel pads of a hybrid containing eight CBC3.1s, called 8CBC3.1 hybrid. The hybrid is read out electrically with an interface board and an attached readout FC7 board running dedicated firmware. The emitter and injector are both placed within a box. Only the optical fibres reach from the emitting side to the injection system. This decouples both circuits galvanically from each other resulting in low noise on the CBC front-end. An external 40 MHz clock generator synchronises both FC7s. Via a cable the trigger signal is sent from the emitter FC7 to the readout FC7.

Extensive studies on a suitable combination of an LED and a photodiode were done on a test setup using a flex hybrid housing two CBC2s. The chosen LED is called IFD99B [Fib19]. It is used for optical data transmission at 156 Mb/s using standard plastic fibres with a diameter of 1 mm. Its signal rise time is 3 ns in a pre-biased mode. This mode means that the LED is

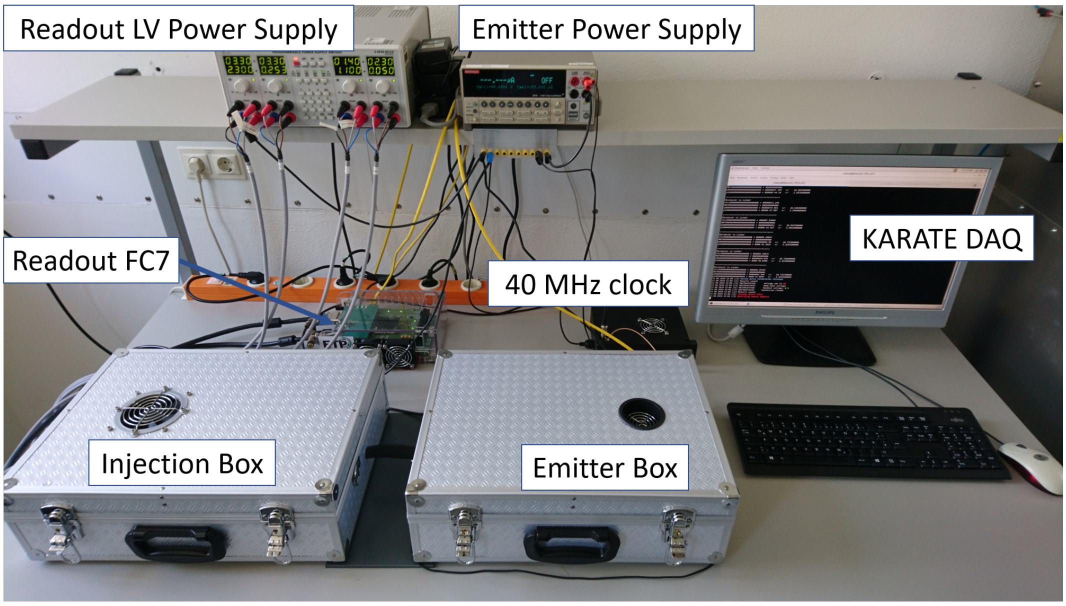

Figure 5.4.: The KARATE system. Emitter and injector are both placed inside a box for protection. A low voltage power supply is needed to read out the hybrid and an additional one to power the LEDs in the emitter box. The readout FC7 and the external 40 MHz clock generator are placed outside the boxes. A computer runs the KARATE data acquisition framework.

always turned on due to an applied bias voltage and an additional voltage pulse increases the light intensity for a short period of time. This avoids longer signal rise times in which the LED first has to turn on. The signal current generating the light flash on the LED is limited by a 750 Ω resistor.

The chosen photodiode on the injection circuit is called FDS015 [Tho19]. It has an active silicon surface of $\varnothing = 150\,\mu\text{m}$. The photodiode stays unbiased, using only the depleted pn junction caused by the built-in potential. This results in electron pulses of several thousands of electrons and a capacitance of 9 pF, comparable to a strip of a 2S sensor. The signal rise-time is 35 ps. Due to the AC-coupling in the injection circuit only the AC part of the LED signal is transferred.

Figure 5.4 and Figure 5.5 show the two boxes containing the emitting and injection boards of the KARATE system and the surrounding components such as the readout FC7, the power supplies and the 40 MHz clock, which complete the table top system.

The generated light pulses can vary in their duration. A pulse can have 15 different lengths. The longer the light pulse on the LED the higher are the resulting signal amplitudes in the CBC front-end, mimicking signals from 0 to up to $60\,000\,e^-$. In addition to this, it is possible to change the intensity of the light by adjusting the bias voltage of the LED as shown and evaluated in Section 5.3.4.

The 48 photodiodes are attached to the transition section between two CBCs. The last 24 channels of the first CBC and the first 24 channels of the second CBC are instrumented. The hybrids in the 2S module have a fold-over to also connect the bottom sensors to the readout chips. Therefore, half of the 24 channels on each CBC are connected to the top-side and the other half to the bottom-side of the hybrid. Each CBC is directly connected with its neighbours sharing hit information to avoid acceptance losses in the stub detection between two chips, as described in Section 3.3.2. This configuration of the instrumented channels ensures the

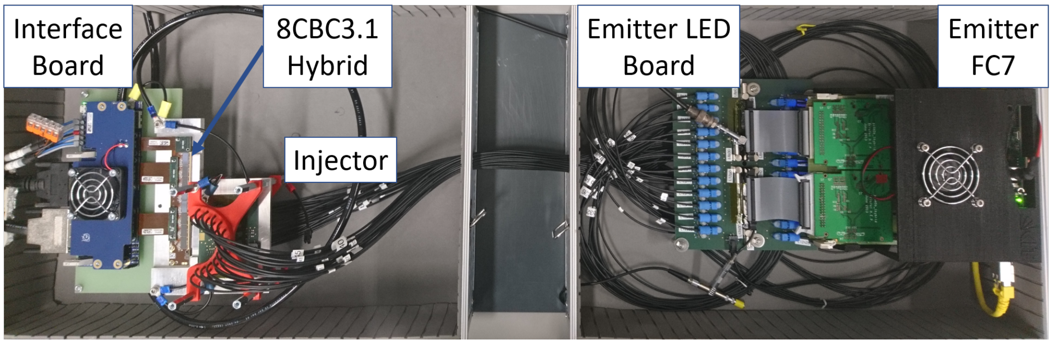

Figure 5.5.: A view inside the injector and emitter box. The emitter on the right consists of an FC7 controlling a board with 48 LEDs. Light patterns are routed via optical fibres to the injection system on the left. The 8CBC3.1 hybrid is read out electrically by an interface board.

validation of the correlation between the top and bottom sensor for the p_T filtering and the inter-chip communication at high rates.

5.2.3. The CMS Tracker Phase 2 Acquisition and Control Framework

The CMS Tracker Phase 2 Acquisition and Control Framework, or Ph2_ACF for short, is a software framework developed to communicate with all Phase 2 tracker-related readout electronics [CMS19a]. Currently developed and used to read out prototype components such as the 8CBC3.1 hybrid, central functionalities will be transferred to tracker data acquisition software to readout and configure the complete future tracker.

The basic principle of the Ph2_ACF is to mirror the hardware within the framework. Therefore, each real component has a software equivalent which can be configured. An XML file contains the hardware description and settings. The XML file stores the information for data communication such as the IP address of the readout FC7, clock and trigger sources and chip settings, e.g. the threshold applied on the CBC channels or the latency value.

The main routines that can be called to read out a hybrid or functional 2S modules:

- **systemtest**: Checks if the hardware description file has the correct format.
- **datatest**: Checks if the Ph2_ACF can communicate with the firmware on the FC7 and if the data format matches the attached hardware.
- **commissioning**: Measures the noise, latency and stub latency
- **calibration**: Manages the calibration routine. This involves a trimming procedures in which all the pedestal of all channels are shifted to a common value by offsets. This assures an uniform response on incoming signals for a given threshold setting. The offset results are stored in text files, which can be configured in the hardware description file for a well-calibrated module readout.

5.2.4. KARATE DAQ Framework

The KARATE DAQ framework is embedded within the Ph2_ACF to ease the data handling among the hardware components. The framework extends the Ph2_ACF with eight classes handling the run configuration and data analysis:

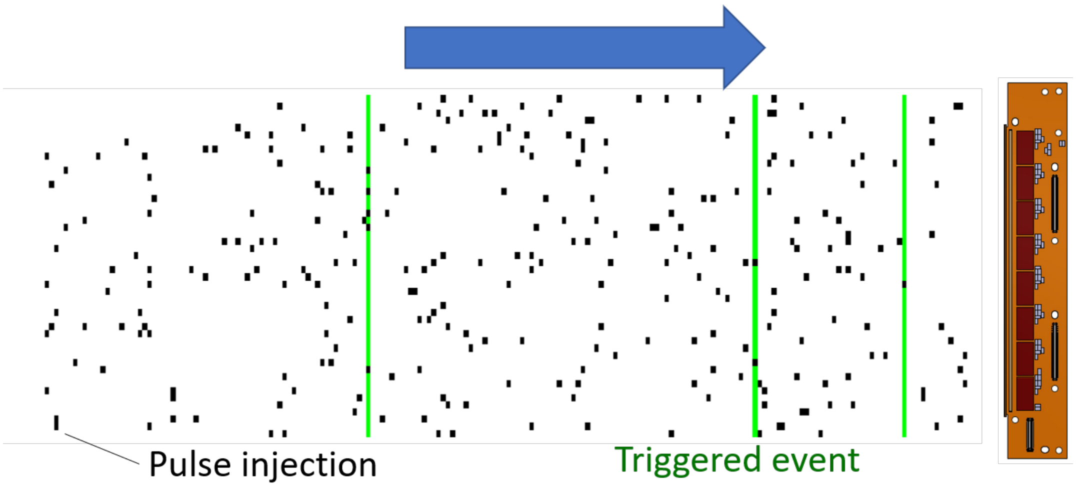

Figure 5.6.: Visualisation of the injection procedure. Each column represents a pattern containing the hit information of 48 channels. Hits are marked with a black rectangle. Events that are triggered for readout are highlighted in green.

- **KarateChannels**: The configuration of which channel is connected to the system might change with time and is stored only once in this class. For consistency, all instances of the framework obtain the list of channels from this class. It also reads the KARATE calibration files containing the conversion factors between light pulse length and front-end signal amplitude.
- **KarateFC7Emitter**: Contains all methods to communicate with the emitter FC7 to store the patterns and to adjust settings.
- **KarateKeithley2410**: Controls the power supply biasing the LEDs on the emitter board.
- **KarateCommission**: Several test procedures necessary for the system's commissioning are combined in this class. This involves measurements of the signals arrival time or pulse reconstruction routines.
- **KarateCalibration**: Measures the correlation between light pulse length and signal amplitude on the front-end for each channel and light duration. The generated file is read by KarateChannels.
- **KarateDAQ**: Main class of the framework. It handles instances of the following classes:
  - **KarateSettings**
  - **KaratePatternGenerator**
  - **KarateEvent**
  - **KarateEventAnalyzer**
  - **KarateFileHandler**

  Each measurement is configured with an additional KARATE settings file, which is read by an instance of KarateSettings. The information is used to adjust settings on the hardware and the pattern list which is generated by an instance of KaratePatternGenerator. The pattern generator produces a list of KarateEvents which are then stored on the

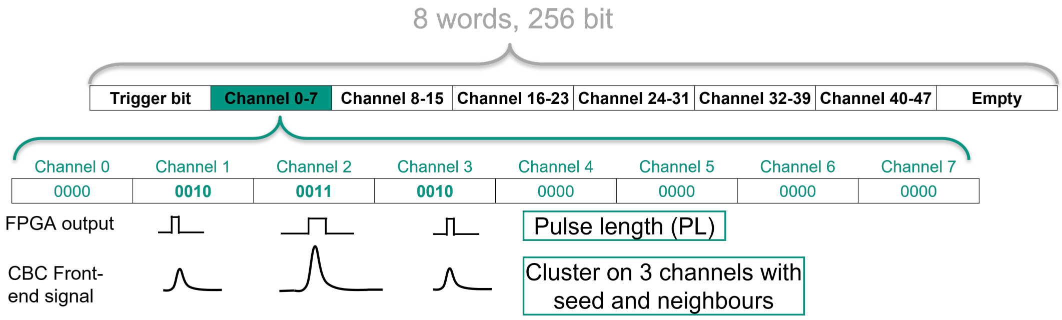

Figure 5.7.: The KARATE pattern structure. A KARATE pattern contains the four bit pulse information of all 48 channels and the trigger bit using 8 words. With varying pulse lengths within one pattern cluster signals can be emulated on the CBC's front end.

emitter FC7. A command is sent to the emitting FC7 to start the pattern output. The pattern injection happens at 40 MHz, but not all injected patterns are accompanied by a trigger signal which is sent to the readout FC7, as described in Section 5.2.5. All triggered events are stored on the internal memory of the readout FC7. After a run the KarateEventAnalyzer compares the readout with the pattern input event by event. If activated, injection patterns and the readout data can be saved to the hard drive with an instance of KarateFileHandler. KarateDAQ instances are able to read these files and to repeat the analysis.

Figure 5.6 visualises the pattern injection into the 8CBC3.1 hybrid. The pattern injection happens at 40 MHz but not each event contains a trigger signal. The triggered events are highlighted in green and can be distributed according to the input given in the settings file.

The settings file contains information on the pattern generation, chip settings and which analysis results should be displayed. The input is split in variables and observables. The variables contain the actual settings values such as threshold or latency. Values from the KARATE settings file supersede the values given in the Ph2_ACF hardware description file. Instead of having fixed settings for a single run, it is possible to define two variables as a range. This results in a two-dimensional measurement matrix and the measurement steps are processed one after another.

The list of observables defines which results are requested from the KarateEventAnalyzer. After each run the graphs and histograms in which they are visualized are updated and in the end saved in a ROOT file. With this online analysis its possible to have immediate feedback of the current measurement. Most of the observables such as the occupancy or cluster efficiency are displayed in point graphs. Some of the observables are displayed for each channel individually or contain two-dimensional information in form of a histogram for each single run. An example settings file is shown and described in detail in Appendix C.2.

The readout firmware stores all triggered events on the internal DDR3 memory of the FC7 until they are requested by the data acquisition software. The maximum number of events to be stored on the internal memory of the FC7 is one million. Therefore, it is possible with the KARATE system to investigate average occupancy effects down to regions of 10^{-6}.

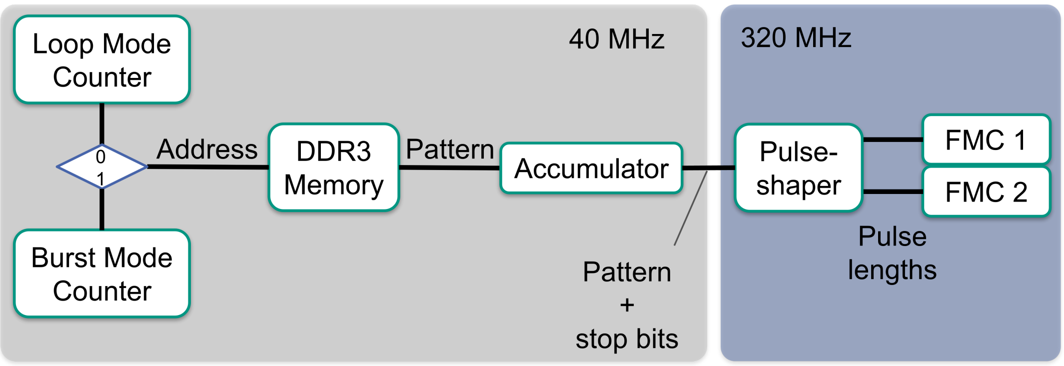

Figure 5.8.: Schematic of the KARATE firmware. Two different modes count addresses which are used to read out pattern stored on the internal DDR3 RAM. Afterwards the patterns are processed in a pulse shaper to translate the information to pulse lengths on the FMC ports where the emitter LEDs are connected. In Appendix C.3 the KARATE firmware is illustrated in more detail.

5.2.5. Emitter Firmware

The firmware on the emitter FC7 is based on the VHDL[1]-based Golden Firmware version 5.0.3 provided by the developers of the board [Pes+19]. Within this golden firmware user code can be inserted conveniently without extensive work on the physical pin assignments or communication protocols. The written firmware reads, processes and sends the patterns out to control the attached LEDs.

Up to eight million patterns are stored on the internal DDR3 RAM of the FC7. Each pattern is structured as shown in Figure 5.7, consisting of 256 bits, divided in eight 32-bit words. The bits of the first word are unused despite the trigger bit. Six words follow, containing the hit information of the 48 channels, 4 bits for each channel. The last word is empty. Within one clock cycle of 40 MHz the Kintex 7 architecture is able to read out 256 bits of its memory at once, which is by chance equivalent to one pattern.

As shown in Figure 5.8, there are two modes the KARATE firmware operates. Each mode is first configured and then stays in an idle state awaiting a start command from the KARATE DAQ. Within loop mode the RAM is read out with addresses generated by a counter block which is permanently looping over addresses of patterns stored in the memory. Each loop ends at a given address saved in a control register. If reached, the count jumps back to zero and the loop repeats. This is used for commissioning procedures and pulse shape reconstruction in which permanent input is necessary. In burst mode the addresses of patterns stored in the memory are also increased by a counter. Different from the previous mode the number of loops is defined in a control register. This results in a defined number of output frames. To suppress any output of the two modes the firmware can be set to idle. In this case the subsequent address of the last stored pattern is sent out by the counters permanently. This pattern is filled with zeros by default and therefore the output is suppressed.

The accumulator block receives the patterns from the memory. The patterns change at 40 MHz. To make two subsequent identical patterns distinguishable the accumulator only forwards each pattern for half a 40 MHz clock cycle followed by a stop pattern the rest of the clock cycle, which is filled completely with ones. Once the pulse shaper running on 320 MHz receives a new pattern it translates the four bit pulse length information in pulse length durations between 0 and 46.875 ns. The 40 MHz and 320 MHz clock signal are both derived

---

[1] Very High Speed Integrated Circuit Hardware Description Language

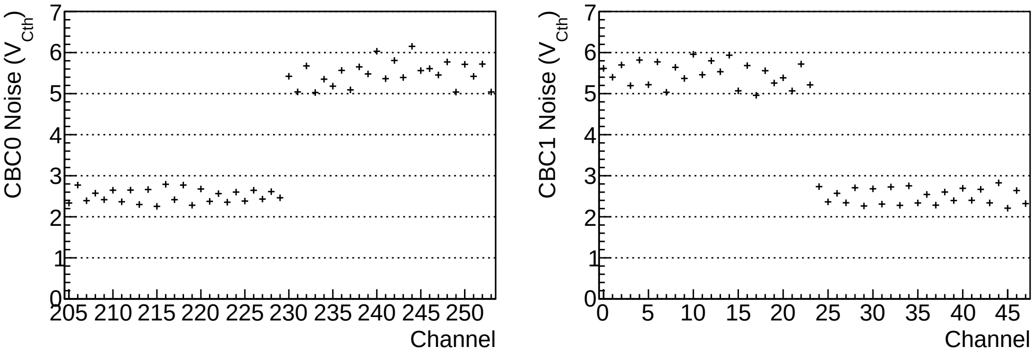

Figure 5.9.: Noise on the attached channels in the KARATE system. The last 24 channels of the first and the 24 first channels of the second CBC are connected. The noise is around 6 V_{Cth}, which translates to about 940 e^-.

from a clock generator, which receives its input clock from the external clock generator via the FMC port. With a control register it is possible to tune the phase of the internal 40 MHz clock. An additional register enables the usage of an internal clock input. The clock signal is then forwarded to an output on the LED emitter board with which it can be forwarded to the readout FC7 for synchronisation. However, using the external clock is advantageous because it has a higher signal quality.

5.3. Commissioning

The KARATE system offers a large variety of input parameters and settings. Therefore, extensive commissioning is important to understand each aspect of the system. Of the greatest interest are the noise of the instrumented front-end channels, the pulse shape quality, the latency setting and the signal calibration of the KARATE system.

5.3.1. Noise

A detector system should affect the noise of the readout channel as little as possible to enable low threshold settings. This improves the sensitivity for smaller signals and thus the efficiency of the detector. The noise of a CBC channel is derived as explained in Section 4.9.2 by an occupancy measurement depending on the threshold. Figure 5.9 shows the noise of the instrumented channels in the KARATE system. The average value is around 6 V_{Cth}. With a conversion factor of 156 e^-/V_{Cth} this translates to approximately 940 e^- [Sei19].

The noise values are shown without error bars, assuming that systematic uncertainties are identical for all channels. In terms of detector operation of most interest is the detection of outliers, meaning noisy channels or low noise channels indicating a faulty electrical connection to the strip of the sensor. Also the noise values should be as equal as possible enabling a homogeneous distribution of noise hits during detector readout.

The unconnected channels show much lower noise, which is attributed to the missing capacitance of the injection board. In those channels the effect of the hybrids fold-over is also visible. Bottom channels that are routed via the hybrid's fold-over to the bottom side of the module have higher noise compared to the top channels. This is caused by the slightly increased capacitance of the longer signal lines seen by the small alternating variations in the noise. Nevertheless the effect is negligible and it blurs by attaching a capacitance such as a strip from a silicon sensor or a photodiode of the KARATE system.

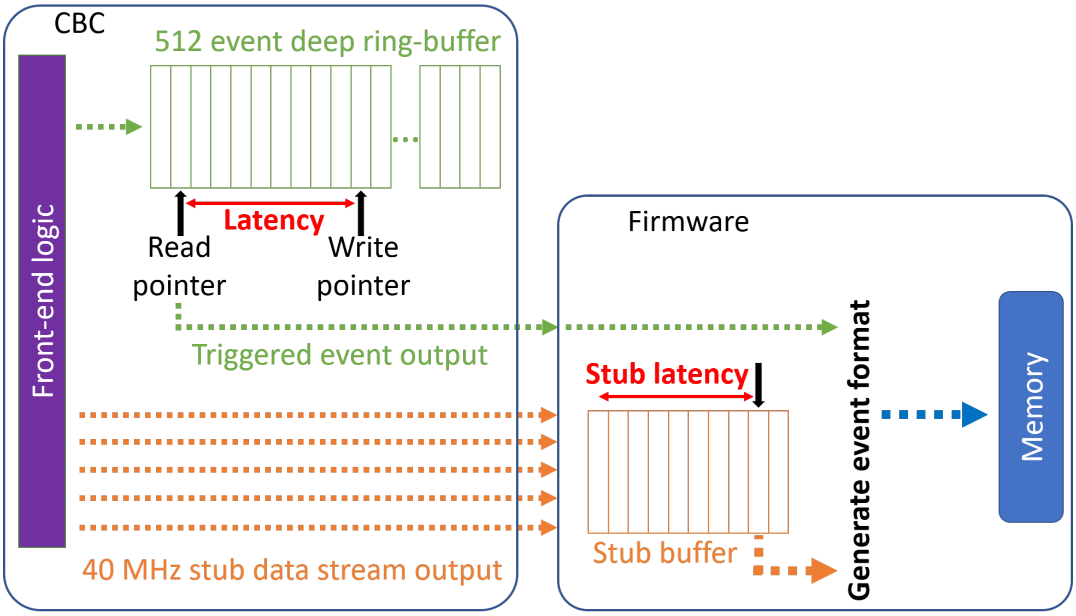

Figure 5.10.: The latency and stub latency have to be adjusted to read out the correct hit and stub information from a CBC. The latency value is a CBC setting describing the distance between the write and read pointer of the 512 event deep ring-buffer. The stub latency is a firmware setting and describes the position in the stub data buffer which has to be combined with the received hit data to generate a matching event format.

The pedestal of the system is at 591 $\mathrm{V_{Cth}}$. All following thresholds settings are stated in electrons based on the conversion factor of 156 $\mathrm{e^-/V_{Cth}}$. To avoid too many noise hits in the readout, a well-chosen threshold is set to a value about five times above the noise of the system. In this case this would be a value of about 30 $\mathrm{V_{Cth}}$ above the pedestal or 4700 $\mathrm{e^-}$. Assuming that the noise follows a Gaussian distribution it is expected to detect a noise hit in a channel once in 1.7 million readout processes.

5.3.2. Latency Scans

As shown in Figure 5.10, the CBC outputs two data streams, the triggered hit data and the stub data. For both data streams a latency has to be adjusted. The hit latency is a setting on the CBC. The CBC stores the binary hit information of all 254 channels within a 512 event deep ring-buffer for 12.5 µs. Once a trigger is received an event is taken from the ring-buffer, serialised and sent out. The ring-buffer readout is managed by a pointer running at a defined latency behind the write pointer. The value has to be identified to read out the matching event for which the trigger signal was sent. Latency values differ for each detector system due to different cable lengths and signal processing in the firmware. The stub latency is a firmware setting. It defines the delay to match the received hit data with the stub data, which is continuously sent out by the CBC and buffered in firmware. The event format generated in the firmware combines the hit data with the stub data and stores it in the internal memory.

In addition to the latency value, which is set in steps of whole bunch crossings, the phase of the front-end has to be adjusted as well but in 25 steps of 1 ns. The highest efficiency is achieved by setting the phase to a time where most of the recorded signals reach their maximum. Because signals can have a large amplitude and thus be above threshold for multiple bunch

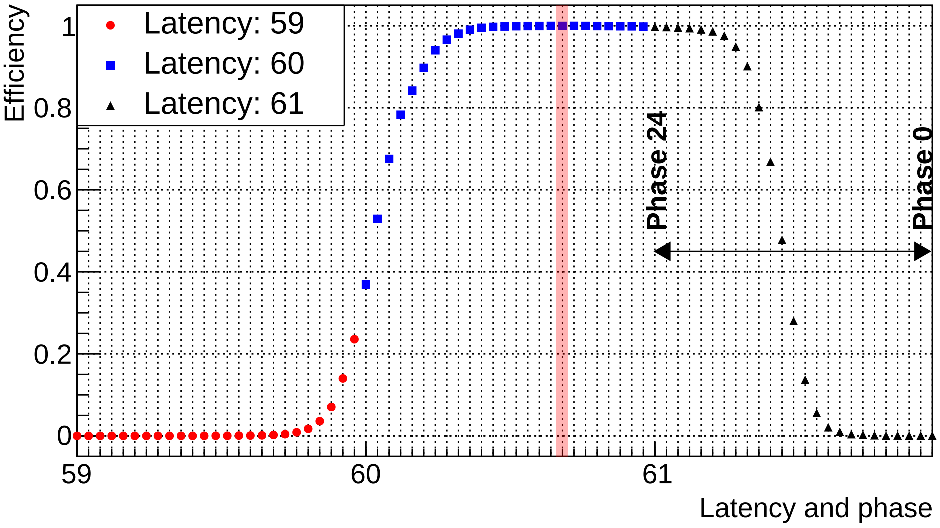

Figure 5.11.: Latency scan of the KARATE system. The overall hit detection efficiency is measured depending on varying latency and phase settings.

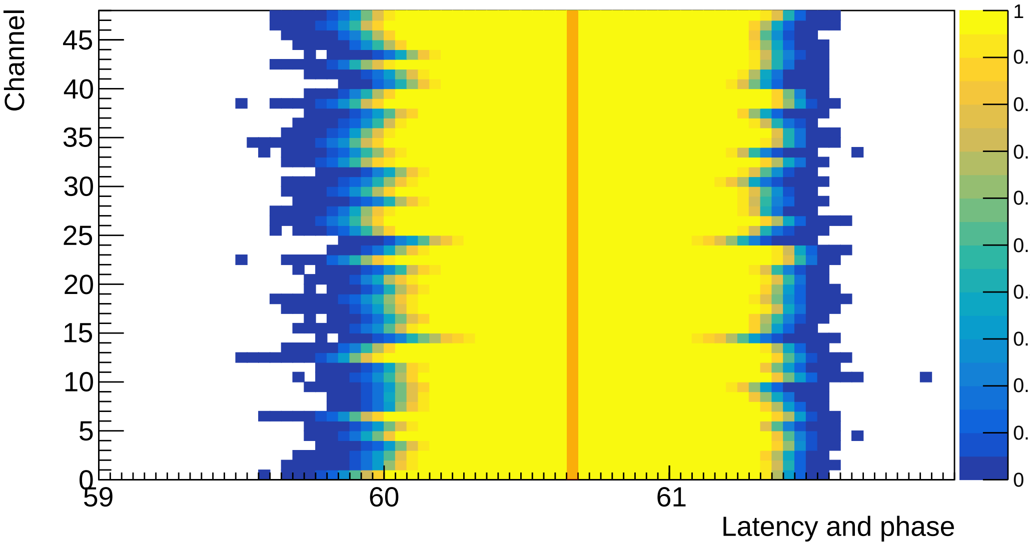

Figure 5.12.: Latency scan for each channel individually. Because each channel has a different response to the same light pulse length the resulting efficiency plateaus vary. The latency value chosen for the following measurements is 60 with a phase setting of 8, which lies in the mid of the efficiency plateau.

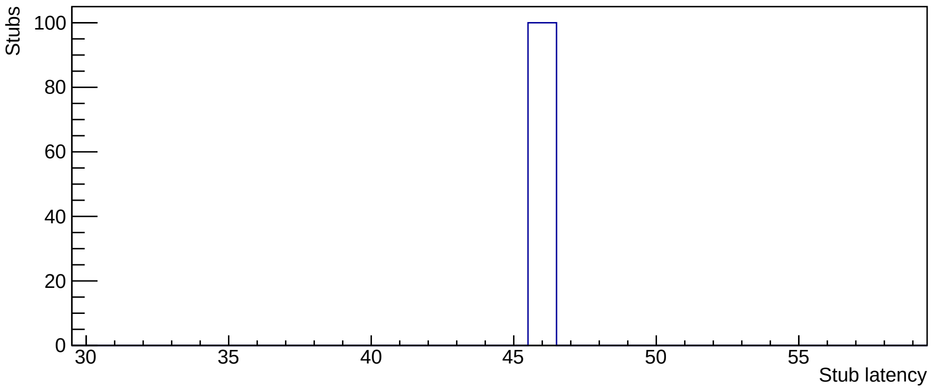

Figure 5.13.: Measurement of the stub latency. The number of stubs for 100 triggered events is recorded while changing the stub latency. With a correct stub latency the injected stubs in the triggered data stream also appear in the stub data stream. Because each injection created a stub the number of stubs should be identical to the numbers of triggers.

crossings it is aimed to be as efficient as possible on the triggered bunch crossing while avoiding to record too much signal still present from previous bunch crossings. The phase setting in the chips can vary inside the tracker due to time of flight delays.

The latency value depends on cable lengths and amount of clock cycles needed to process the signal in the firmware and on the chip. In addition to this, an additional trigger delay can be configured in the firmware. With an additional delay setting of 50 clock cycles the latency of the KARATE system turns out to be between 59 and 61. Therefore, the latency scan performed for the KARATE system is made for settings of 59 to 61. Higher latencies represent earlier bunch crossings, while higher phase settings represent a later sampling time within one bunch crossing. Therefore, for each latency value the phase is shifted from 24 downwards to 0 to get a valid reconstruction in time of the detection efficiency.

Figure 5.11 shows a latency scan for the KARATE system at a threshold of 4800 e^-. The pattern list injected contains one filled and triggered pattern, while the following 49 patterns are empty. In the filled pattern hits with constant light pulse length, resulting in signal amplitudes of roughly 12000e^-, are randomly distributed over the 48 channels. According to these results, the latency value chosen is 60 with a phase setting of 8, which is located in the midpoint of the efficiency plateau.

Figure 5.12 shows the result of the latency scan for each channel individually. In an ideal case, the response among the channels for equal light pulse length would be identical, but variations in the absolute signal amplitude are visible, indicating varying efficiency plateaus between the channels. This affirms the necessity for a calibration to obtain the relation between light pulse length and the resulting signal amplitude, as it is done in Section 5.3.4.

To determine the matching stub latency value the KARATE system is used to inject hits in two corresponding channels from the top and bottom side of the hybrid creating a stub. As shown in Figure 5.13, the stub latency is varied while the number of stubs in the event readout is monitored. The chosen stub latency value is 46, which is the only value with a non-vanishing number of stubs.

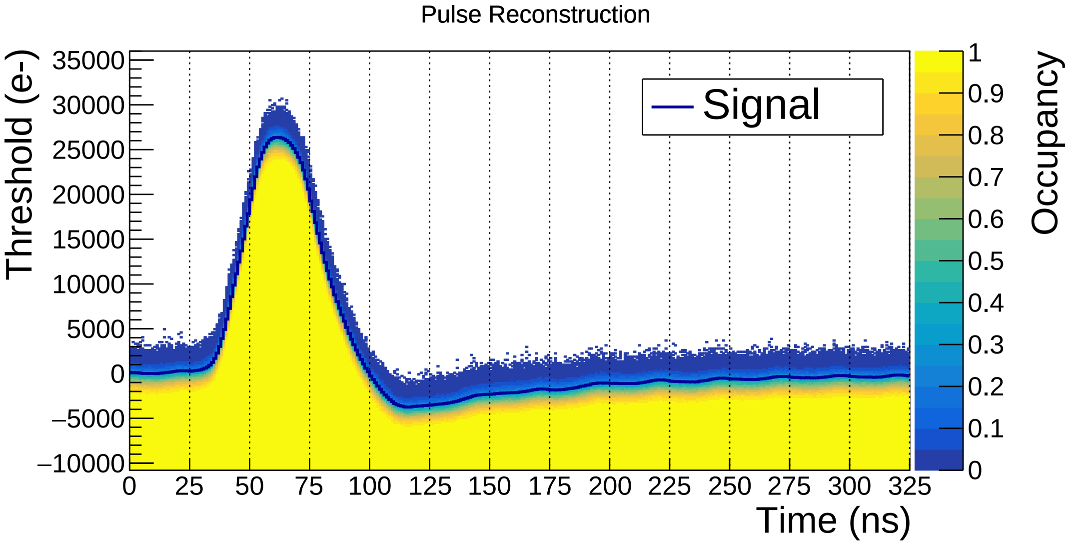

Figure 5.14.: Pulse reconstruction of a single pulse injected with the KARATE system. The pulse height is approximately 30 000 e^-. As stated in the CBC's design specifications the amplifier reaches the maximum after 20 ns and returns below the pedestal after 50 ns. It takes more than 300 ns before the baseline reaches its previous value.

5.3.3. Single Pulse Reconstruction

Figure 5.14 shows the reconstructed pulse of a single injection in one CBC channel. The pulse is reconstructed by measuring the occupancy on the channel for different thresholds and time. Similar to the latency scan the latency is increased step-wise and for each latency value the phase is decreased from 24 down to 0. With this, the pulse injected can be reconstructed correctly. The reconstructed pulse shows exemplary the baseline behaviour during a measurement. As stated in its design specification the amplifier reaches its maximum after 20 ns and falls back below the pedestal after 50 ns [Pry19]. Depending on the threshold setting this signal would generate a hit in two consecutive bunch crossings. This will affect the overall cluster reconstruction efficiency on the system, as shown in Section 5.6. After the injection the baseline stays within an undershoot for more than 300 ns before it reaches its initial value before the injection. This is also discussed in Section 5.9.

5.3.4. KARATE Calibration

Charged particles crossing an active silicon sensor volume deposit their energy via ionization. A minimum ionizing particle generates about 76 e^- per micrometer in a silicon sensor, see e. g. [Har17]. Therefore, the signal depends on the thickness and inclination angle of the particle's track. To emulate sensor signals with the KARATE system it is necessary to calibrate the system. The calibration measures the resulting signal amplitude on each CBC channel depending on the light pulse length of the LED. The duration for the pulse to reach its peak depends on its amplitude. Therefore, the calibration routine searches the pulse peak in a range of different phases to obtain the maximum amount of charge registered.

The step size of the signal amplitude depends on the bias voltage applied on the LEDs on the emitter board. This allows different modes to operate the system. With an increased bias voltage higher signal amplitudes can be generated. This enables the emulation of particles that generate very large signals in the silicon sensor. Those Highly Ionizing Particles can deposit

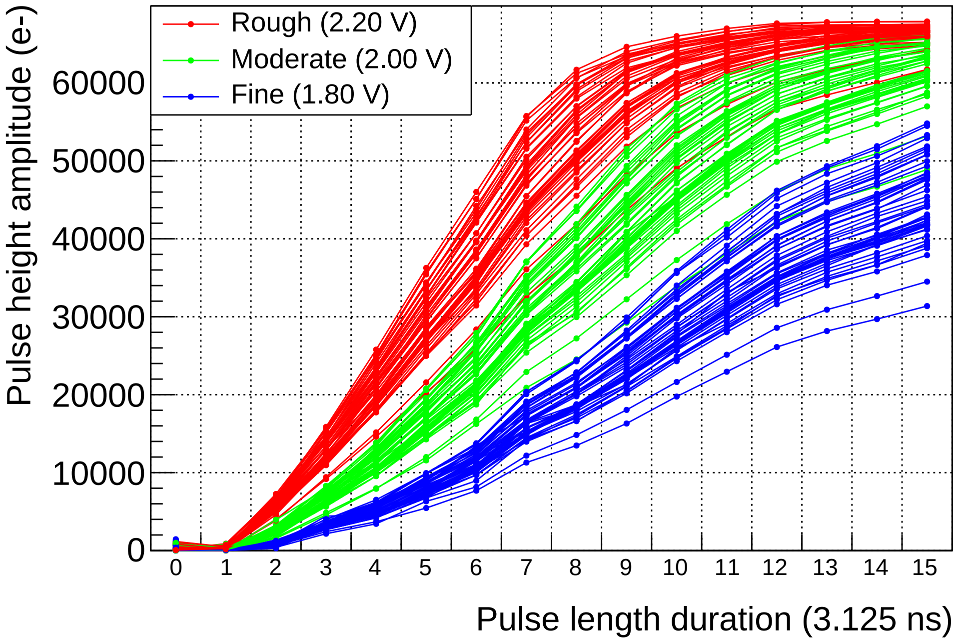

Figure 5.15.: Results of three calibration measurements with different LED bias voltages of the KARATE system. With small voltages (1.8 V, blue) the correlation between light pulse length and signal amplitude of the front-end is less steep than with a intermediate (2.0 V, green) or high LED bias voltage (2.2 V, red).

more than ten times more charge in silicon compared to Minimal Ionizing Particles, which drives the front-end pre-amplifier into saturation and the signal exceeds the threshold over multiple clock cycles.

Lower voltages result in a finer stepping of the signal amplitude and are suitable for studies emulating Landau-distributed signals typically generated in a silicon sensor. Figure 5.15 shows the calibration results for all 48 channels for three different biasing conditions for the LED. In case of a high bias voltage the signal amplitude steps increase and the saturation of the front-end appears above 60 000 e^-.

The correlation can be seen linear for pulse length durations of 1 to 12 for the fine e^--stepping, 1 to 10 for the moderate scenario and 1 to 7 for the rough e^--stepping setting.

5.4. Cross-Talk Measurements

The KARATE system has full control over 48 CBC channels. This gives the opportunity to perform a cross-talk measurement to evaluate the effect of an external pulse injection on the neighbouring channels. Using solely internal CBC test pulses would not involve the effects the hybrid and its signal lines have on the readout system.

The procedure to evaluate cross-talk effects are repeated on all attached channels. For each channel a pulse of constant height is injected at 400 kHz, which would also not be possible with internal test pulses. A 400 kHz injection is equivalent to a single channel occupancy of 1 %. The signal on the injection channel and the behaviour of the pedestal on its neighbours is reconstructed as explained in Section 5.3.3 in 5 ns steps. Once the reconstruction is completed the pulse amplitude is increased and the routine is repeated for 10 different signal amplitudes.

Figure 5.16.: Effect of a pulse injection on adjacent channels. The ratio between the injection amplitude and the difference of the maximum and minimum pedestal value of the resulting wiggle is defined as cross-talk.

This requires very fine steps in the signal amplitude and therefore is not realized with changing the light pulse length but with keeping it on a constant value and change the bias voltage of the LED.

The measurement is done for each instrumented channel resulting in more than 50 000 two-dimensional histograms which have to be analysed. As shown in Figure 5.16, the amplitude of the pulse injection is defined as the difference in the pedestal values before the pulse and at its maximum. The injection causes a wiggle on the neighbouring channels. The cross-talk between the injection channel and its neighbours is defined as the ratio between the wiggle's magnitude and the injection signal amplitude.

The results of the wiggle measurements of neighbouring channel for all ten different signal amplitudes are stored in a graph. With a linear fit the cross-talk is derived for each neighbour. The fit results are grouped by their distance to the injection channel. The mean values of these groups are shown in Figure 5.17 separated for top channel and bottom channel injections. As expected, the highest influence is seen in channels which are directly adjacent to the injection channel. In terms of channel numbers this translates to channels with a value ±2 due to the alternating counting of top and bottom channels in the CBC. The largest effect is seen with a bottom channel injection. The resulting cross-talk is about 2.1 % in the adjacent neighbours. The value is higher compared to a top channel injection where the cross-talk results to a maximum value of about 1.6 %. This is caused by the fold-over of the hybrid flex circuit routing the signal lines from the bottom side of the module to the CBC on the top side. The longer the signal lines the higher is the effect of a signal coupling into neighbouring channels.

This values are not seen to impair the detector readout. Even with very large signals of 100 000 e^- the resulting effect on the neighbours would be around 2000e^-. Having reasonable threshold settings of 4000 e^- to 5000 e^- the cross-talk will not impair the overall detection efficiency.

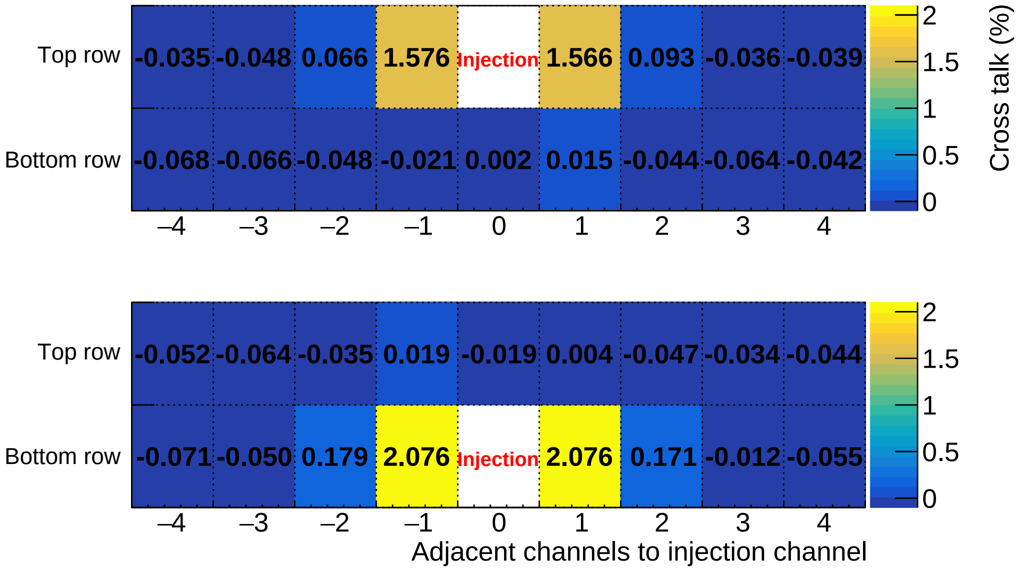

	−4	−3	−2	−1	0	1	2	3	4
Top row	-0.035	-0.048	0.066	1.576	Injection	1.566	0.093	-0.036	-0.039
Bottom row	-0.068	-0.066	-0.048	-0.021	0.002	0.015	-0.044	-0.064	-0.042

	−4	−3	−2	−1	0	1	2	3	4
Top row	-0.052	-0.064	-0.035	0.019	-0.019	0.004	-0.047	-0.034	-0.044
Bottom row	-0.071	-0.050	0.179	2.076	Injection	2.076	0.171	-0.012	-0.055

Figure 5.17.: Cross-talk between a CBC channel and its neighbours separated for injections in a bottom channel and a top channel.

5.5. Track-based Pattern Injection Model

Particles crossing a p_T-trigger module will generate a signal in both silicon layers in most cases. The KARATE system includes a model to emulate such track signals as realistically as possible within the constraints of KARATE. The pattern generator algorithm calculates the number of electrons that are expected on a readout channel depending on various input parameters. With the calibration introduced in Section 5.3.4 the best matching light pulse length for each channel and pattern is determined. Its parameters are tuned using real beam test data performed by the CMS collaboration in the end of 2018. Miniature prototype modules with 290 µm thick silicon strip sensors read out by CBC3s were used to detect 120 GeV protons [Upl19]. For a realistic emulation the model has to meet several requirements:

- Landau-distributed signal generation
- Variable track angles
- Consideration of charge sharing between two strips
- Variable track density

The input value of the track density is used to calculate the probability of a track to cross a channel per bunch crossing. This value is used to distribute tracks randomly on the 2×24 instrumented channels using uniformly distributed real numbers between 0 and 1. For the track generation another uniformly distributed real number between 0 and 72 gives the position where the track enters the bottom sensor layer, called seed position, in units of strips. To have a uniform track distribution even at higher track incidence angles the modelled cross section is three times wider than the instrumented area explaining the range to be 72 instead of 24. Inclined tracks can have a cluster signal on the first sensor outside the instrumented channels while the second is within. Only the information of the 2×24 channels within the instrumented area in the range 24 to 48 is further processed.

With the angle of the track as input the position where the track leaves the upper sensor layer, called correlated position, is calculated. The angle is not a fixed value. It is implemented

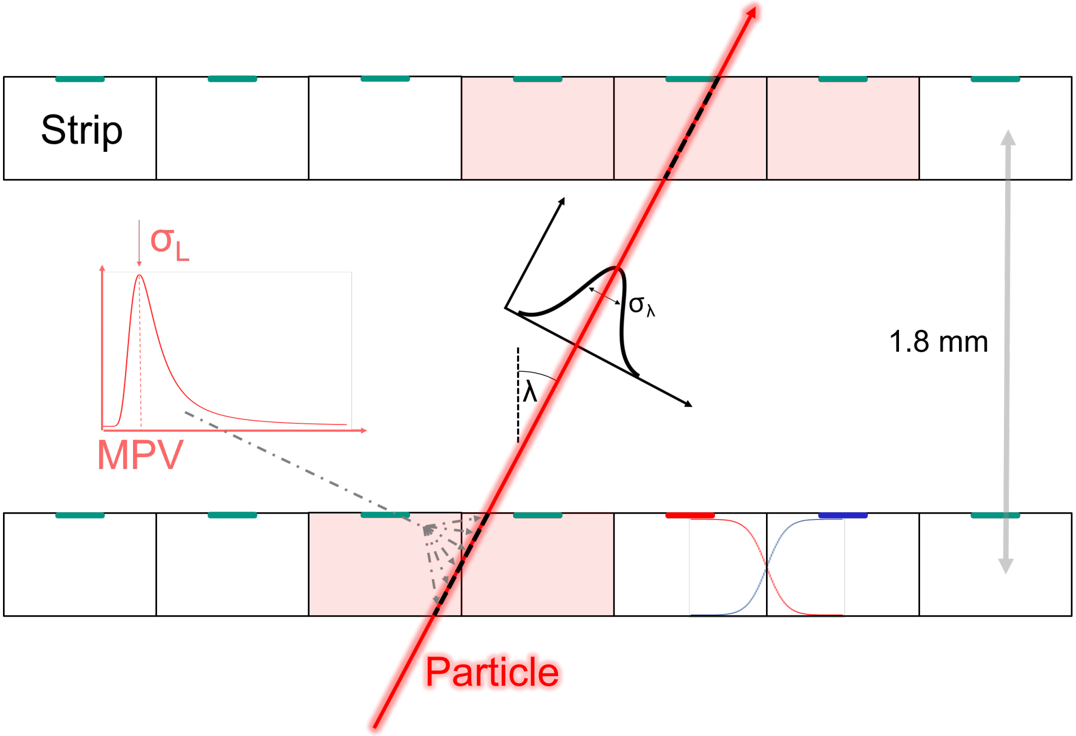

Figure 5.18.: Model developed to emulate signals of a silicon strip sensor. The track of a particle is inclined by an angle λ which is drawn from a Gaussian distribution with the width σ_λ. The trajectory within the silicon sensor is split in tracklets of 1 µm. A signal value generated by a random number following a Landau distribution is assigned to each tracklet. The signal value is split between the two neighbouring channels depending on the tracklets position. The model assumes a module with a sensor spacing of 1.8 mm.

with a Gaussian distribution having two parameters: The average angle λ and the width of the Gaussian distribution σ_λ. This is useful for emulating measurements with a point like source emitting particles in a wide range of angles or to fix the inclination angle for particles coming straight from one direction. Also the effects of multiple scattering in the lower sensor can be investigated. The model assumes a module with a sensor spacing of 1.8 mm.

As shown in Figure 5.18, the trajectory of the generated track inside the silicon volume is split in small track segments of one micrometer, called tracklets. With random numbers distributed according to Landau distribution, which is defined by parameters obtained in Section 5.5.1, an electron signal is derived and assigned to each tracklet. Each signal of a tracklet is split on the neighbouring channels depending on its position between two strips. All tracklet signal assignments of one channel are summed up.

With the KARATE calibration the electron signal for each channel and light pulse length is known. The sum of the electron signal of each channel required to generate the track is compared to the signal amplitudes of the KARATE calibration. The light pulse length whose resulting front-end signal amplitude is closest to the calculated electron signal is chosen as input and stored in the pattern.

The parameters of the Landau distribution have to be defined based on signal measurements on silicon strip sensors. The model for the implementation of the charge sharing is tuned with results obtained in a beam test by the CMS collaboration.

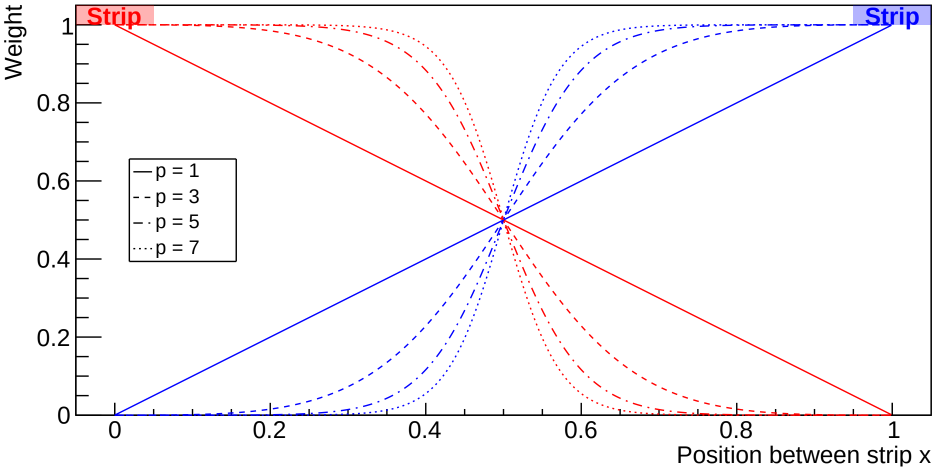

Figure 5.19.: Assignment ratio functions for signals generated between two strips of a silicon sensor. Depending on p the functions result in more or less distinct signal assignment to one strip. The centre of the strip implants are located at $x = 0$ and $x = 1$.

5.5.1. Landau Distribution

As stated e.g. in [Har17] a Landau distribution with an MPV of 76 e$^-$/µm and a mean value of 108 e$^-$/µm describes the energy deposition of minimal ionizing particles in silicon using an upper limit of 500 e$^-$/µm. For particles having a track orientation perpendicular to the sensor, this results in a most probable cluster signal of 22 000 e$^-$ in 290 µm thick silicon sensors. Appendix C.1 describes the Landau distribution used to generate the tracklet signals.

5.5.2. Charge Sharing Model

The charge deposited by traversing particles within a silicon sensor drifts according to the presence of the electric field to the nearest readout implants and the sensor backside. Particles that are crossing the sensor volume at an angle not perpendicular to the sensor surface have a longer trajectory inside the depleted silicon volume and thus deposit a larger signal spread among multiple strips. Therefore, the model considers the incident angle by dividing the track into tracklets. The assignment of each tracklet to the two adjacent channels is based on a model emulating the electric field effects between to strips using the two functions

$$W_L = \frac{(1-x)^p}{(1-x)^p + x^p} \quad \text{and} \quad W_R = \frac{x^p}{(1-x)^p + x^p}. \tag{5.1}$$

W_L and W_R describe the assignment ratio of a tracklet signal to the adjacent left (W_L) and right (W_R) channel depending on the fractional position between the two strips x. The parameter p is the exponent which has to be tuned. The higher p the more distinct is the charge separation between two strips. Figure 5.19 visualizes the resulting ratio functions for p between 1 and 7.

The parameter p is tuned by comparing the mean cluster sizes of KARATE measurements with data obtained in a beam test. The pattern list used for the KARATE measurement contains one filled pattern followed by 49 empty patterns. The filled patterns contain tracks creating cluster signals based on the Landau distribution obtained in Section 5.5.1 emulating minimal ionizing particles. For different values of p, the angle is varied between 0 ° and 22 °.

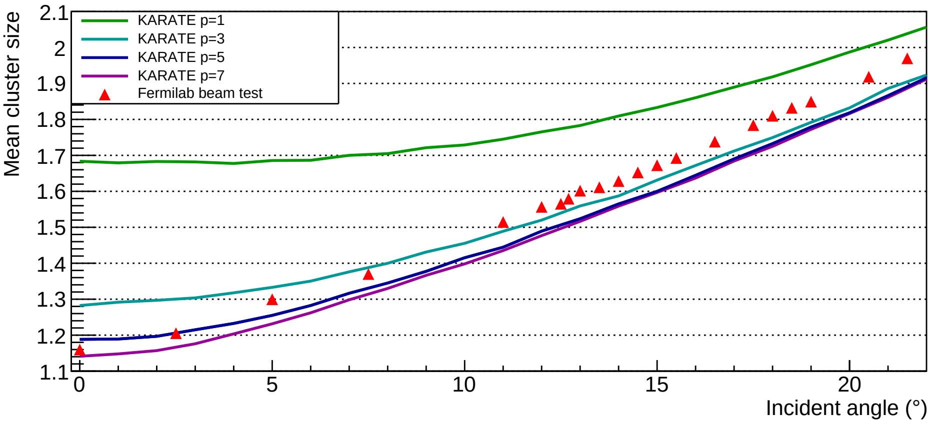

Figure 5.20.: Comparison of the mean cluster size measured with the KARATE system for different angles and p to data obtained in a beam test. With $p = 5$ the KARATE results match the test beam measurement quite well [Upl19]..

Figure 5.20 shows the result of the KARATE measurements compared to the data obtained in a beam test. The threshold of both measurements was set to about $4200\,\mathrm{e}^-$. The higher p, the smaller become the mean cluster sizes for perpendicular tracks. As expected the mean cluster sizes increase with angle due to the larger signal amplitudes resulting from the elongated trajectories.

The KARATE measurement with $p = 5$ matches the beam test data quite well, although having an offset in the cluster size of about 0.1 strips at angles above 10 °. This could be due to variations in the threshold settings and the fact that the model does not consider the full complexity of the electric field inside a silicon sensor. Nevertheless, this rather simple yet effective approach seems to be sufficient to emulate the induced signal inside a silicon strip sensor for the KARATE system.

To further validate the model, measurements of the cluster efficiency depending on the threshold are compared between a KARATE measurement and data obtained in the same beam test as used for the tuning of p. In the analysis of the KARATE measurement a recorded cluster is found to be valid if its centre of gravity is within ± 1.5 strips with respect to to the injection cluster. Invalid or non-existing clusters are assumed to be lost. The overall cluster efficiency in the KARATE system is defined as

$$\text{Cluster efficiency} = 1 - \frac{\text{Lost clusters}}{\text{Injected clusters}}. \tag{5.2}$$

This is analogous to the beam test analysis in which a cluster signal is valid if its centre of gravity is within $135\,\mu\mathrm{m}$ of the interpolated particle trajectory reconstructed by the telescope.

The measurement made with the KARATE system had a most probable cluster of $22\,000\,\mathrm{e}^-$ and a track density of $1\,\mathrm{MHz/cm^2}$ with perpendicular orientated tracks. Only the triggered events contain tracks to avoid an impairment of signals from previous bunch crossings to the clustering. The cluster efficiency was measured for increasing thresholds in steps of about $312\,\mathrm{e}^-$. Figure 5.21 shows the comparison of both measurements. Although the two measurements do not agree perfectly the similarity in their shapes is considered to be sufficient to demonstrate that the model emulates a sensor signal accurately.

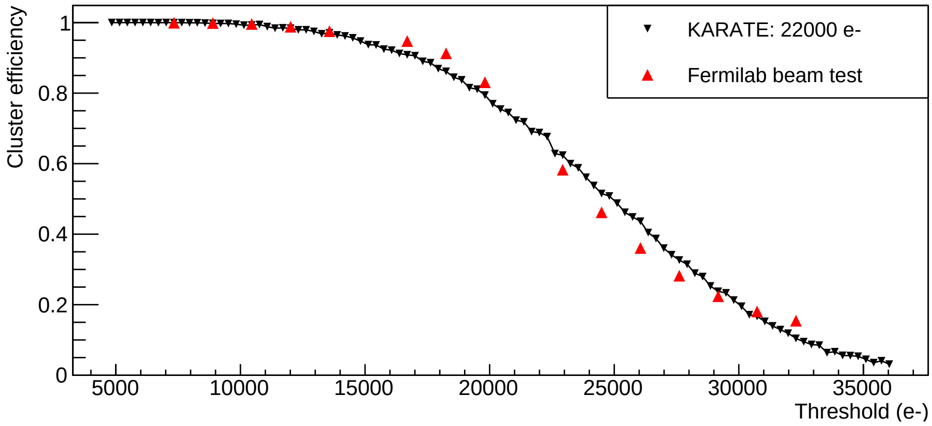

Figure 5.21.: Threshold scan to compare the cluster efficiency between a KARATE measurement and data obtained in a beam test. The beam test was performed with a CBC3 module reading out 290 µm thick silicon sensors at Fermilab [Upl19].. For the KARATE measurement a perpendicular track orientation and a cluster signal of 22 000 e$^-$ was set.

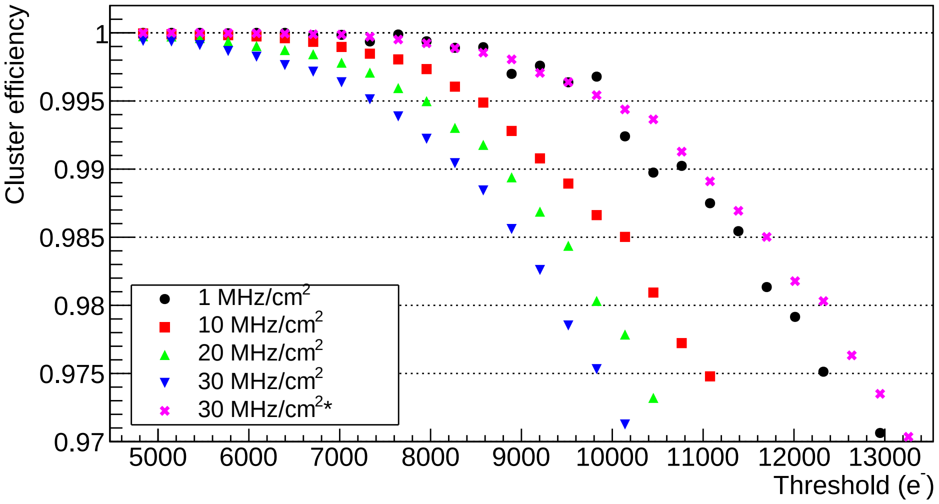

Figure 5.22.: Cluster efficiency depending on the threshold and track densities. The mean trigger rate is set to 750 kHz and the cluster signal to 22 000 e$^-$. As expected the cluster efficiency drops with increasing track densities and thresholds. An additional measurement, marked with an asterisk, has a track density of 30 MHz/cm^2 but the pattern list is empty except for the triggered pattern (pink).

5.6. Efficiencies Depending on Track Density and Threshold

The reconstruction of particle trajectories within a silicon tracker is based on the combination of close-by hits in adjacent detector layers. As shown in Figure 5.14, signals can be above the threshold for multiple clock cycles. This results in additional signals in triggered events which can arise from previous bunch crossings, which are in the following referred to as fake hits. In the running experiment these signals appear randomly in the tracker and should be excluded from a possible track as much as possible by the reconstruction algorithm. In the current strip tracker additional hits arise not just from large signals generated in previous bunch crossings but also from secondary vertices or backscattered particles. Therefore, these signals are called out-of-time pile-up signals. They contribute up to a third of the occupancy [Mal18].

Using the pattern injection at 40 MHz, the KARATE system is used to evaluate the effect of the track density and thus additional fake hits on the cluster efficiency. The threshold is increased while the cluster efficiency and the overall occupancy and the fake hit occupancy is measured. All tracks are oriented perpendicular to the sensor plane and the mean trigger rate is set to 750 kHz. The cluster signal is Landau-distributed according to Section 5.5.1 with an MPV of 22 000 e^-.

The fake hit occupancy can be reconstructed because the pattern injections in bunch crossings before the triggered event are known. A recorded but unexpected hit in a channel is marked as a fake hit if one of the two previous patterns also contained a hit on this channel. Unexpected hits that do not fulfil this criterion are considered to be caused by noise. These will be investigated in greater detail in Section 5.9. The overall occupancy is defined as

$$\text{Occupancy} = \frac{\text{Recorded hits}}{\text{Triggers} \times \text{Instrumented channels}} \tag{5.3}$$

and the fake hit occupancy as

$$\text{Fake hit occupancy} = \frac{\text{Recorded fake hits}}{\text{Triggers} \times \text{Instrumented channels}}. \tag{5.4}$$

Figure 5.22 shows the cluster efficiency depending on the applied threshold for different track densities between 1 and 30 MHz/cm^2. As expected, the cluster efficiency decreases with increasing threshold and track density, because additional adjacent fake hits can shift the centre of gravity of recorded clusters within a triggered event so that they become invalid according to the above criteria.

Looking at the reconstruction of a single pulse, as discussed in Section 5.3.3, the baseline of a front-end channel goes into an undershoot after the detection of a large signal. Small signals reaching the front-end in this particular time period will have a decreased probability to exceed the threshold. This can also cause a shift of the centre of gravity of a cluster or make the cluster disappear as a whole, resulting in additional inefficiencies.

An additional scenario is shown in which the track density is again set to 30 MHz/cm^2, but only the triggered events contain tracks whereas all patterns in between are empty. The resulting cluster efficiency curve almost follows the low occupancy measurement with a track density of 1 MHz/cm^2 demonstrating that mostly the fake hits and too high thresholds cause inefficiencies. Within reasonable thresholds of 3800 e^- to 6400 e^-, which refers to thresholds of 4 to 7 σ above the pedestal in widths of the noise distribution the effect is below 0.2 % and therefore negligible.

Additionally, Figure 5.23 summarizes the overall occupancy as well as the contribution of the fake hits to it for the same measurement. Fake hits make up nearly half of all detected hits.

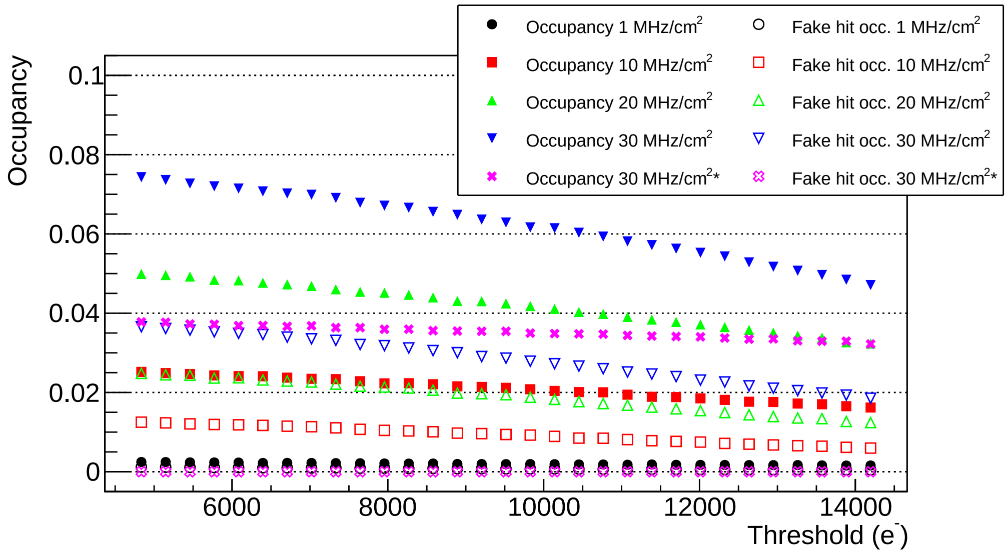

Figure 5.23.: The overall occupancy and the fake hit occupancy depending on the threshold and track density for the same measurement shown in Figure 5.22. Fake hits make up up to half of all recorded hits.

5.7. Efficiency Measurements depending on Trigger Rates

The possibility to freely distribute the trigger signals among the pattern list is used to investigate the readout behaviour for different trigger conditions with various measurements. A constant separation between trigger signals is used to evaluate possible resonance effects on the readout. In another measurement, the detector operation is emulated using trigger signals that are distributed according to a Poisson distribution. In addition to this, the behaviour during a buffer overflow of the chip is analysed with trigger rates above the CBC's design specifications.

5.7.1. Constant Trigger Rates

During the commissioning of the current strip tracker of the CMS experiment unexpected effects in the readout occurred. Depending on the trigger pattern at high rates the noise in certain channels of the readout chip increased. These High Rate Noise (HRN) effects resulted in special trigger rules that have to be applied during the tracker operation which exclude certain patterns to prevent a high occupancy output in single events [Cha+10].

The KARATE system evaluates the detection efficiency of the CBC3.1 at high trigger and hit rates. In addition to this it is used to search for effects similar to the HRN effect in the current tracker to occur in the readout data. With a full readout chain including the CIC, LpGBT and VTRx+ this will be even of more interest because the probability of some unexpected influence on the inter chip communication and front-end on the module increases.

The mean trigger rate in the Outer Tracker will vary between 500 kHz to up to 750 kHz, depending on the average pile-up. To test for possible effects in the readout depending on the trigger separation a list of patterns with triggers that have a constant separation is injected. The patterns represent perpendicularly oriented tracks with a density of 10 MHz/cm^2. The cluster signal is set to 22 000 e$^-$. The separation between the triggers is varied for each run in steps of one bunch crossing. The measurement range is between 100 and 38 bunch crossings, which corresponds to trigger rates of 400 kHz and 1.05 MHz, respectively. 38 bunch crossings is the lower limit in this measurement because it takes 38 bunch crossings for the CBC to output

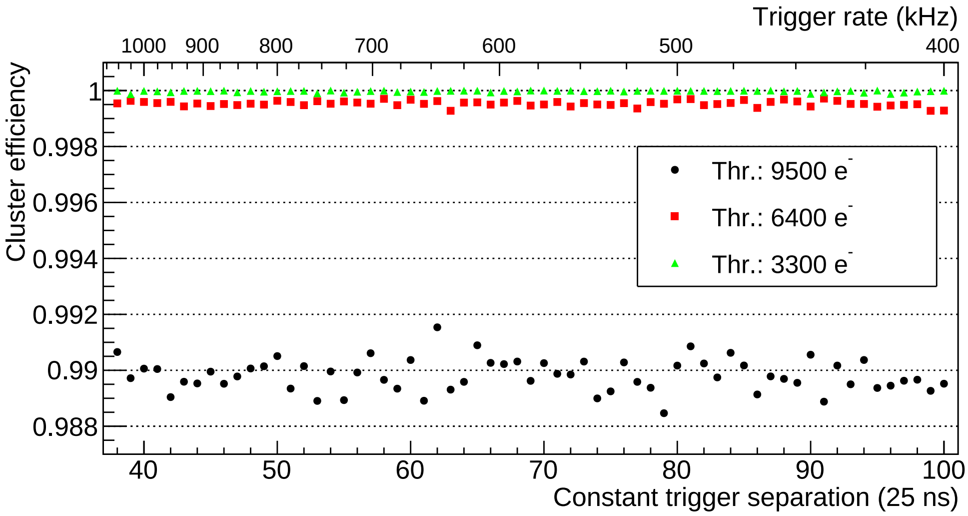

Figure 5.24.: Cluster efficiency measurement depending on constantly distributed trigger separations between 38 and 100 bunch crossings and varying thresholds. The cluster signal of the perpendicular oriented tracks is set to 22 000 e^-.

a triggered event. By increasing the trigger rate further an internal buffer of the CBC overflows and data loss is encountered as evaluated in Section 5.7.4. The measurement is repeated for various threshold settings of 3300, 6400 and 9500 e^-. These values are chosen to see possible effects on the noise and fake hit occupancy as well as on the cluster efficiency. The noise hit occupancy is defined as

$$\text{Noise hit occupancy} = \frac{\text{Unexpected hits (Excluding fake hits)}}{\text{Triggers} \times \text{Instrumented channels}}. \tag{5.5}$$

Figure 5.24 and Figure 5.25 show the results for the cluster efficiency as well as the fake and noise hit occupancy. For a lower threshold of 3300 e^- and 6400 e^- the efficiency is almost completely 1. The noise hit occupancy is 0 for thresholds above 6400 e^-. For 3300 e^- it is constant for all trigger separations having a value of about 1×10^{-3} being about five times above 2×10^{-4}, which would be the expected noise occupancy at this threshold assuming Gaussian distributed noise. Because this is still a very small fraction compared to the recorded fake hits it is not seen to impair the tracking efficiency. Nevertheless, the noise behaviour of the system under higher occupancy conditions is discussed in Section 5.9. The fake hits increase with lower thresholds but are also independent from the trigger separation.

For a constant trigger separation between 61 and 63 bunch crossings the noise hit occupancy shows a variation of about 3×10^{-4}. This occurs at trigger separations that are very close to the latency setting determined in Section 5.3.2, which supports the assumption that this behaviour is linked to the trigger signal. Additional measurements indeed show that the variation is correlated to the fast command trigger signal coming from the readout FC7 board. By increasing the trigger delay setting on the firmware the variation moves to higher values accordingly. This is shown in Figure 5.26, where a second measurement with an additional trigger delay of five bunch crossings shows identical behaviour for trigger separations around 66 and 68 bunch crossings. It is assumed that when the chip receives a trigger and starts the readout process, the baseline of the pre-amplifier is slightly affected resulting in more or fewer noise hits. This becomes visible when the previous event is read out at the same moment a new

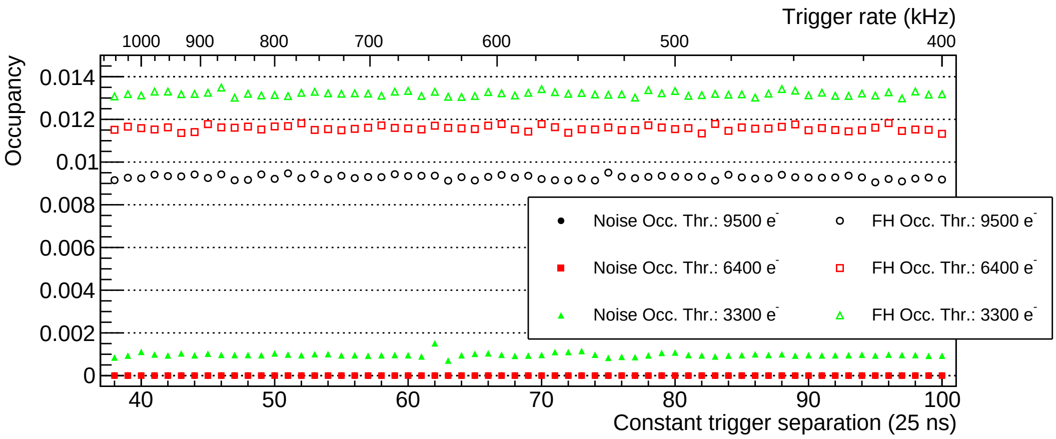

Figure 5.25.: Fake hit occupancy and noise hit occupancy for constant trigger separations and three different thresholds.

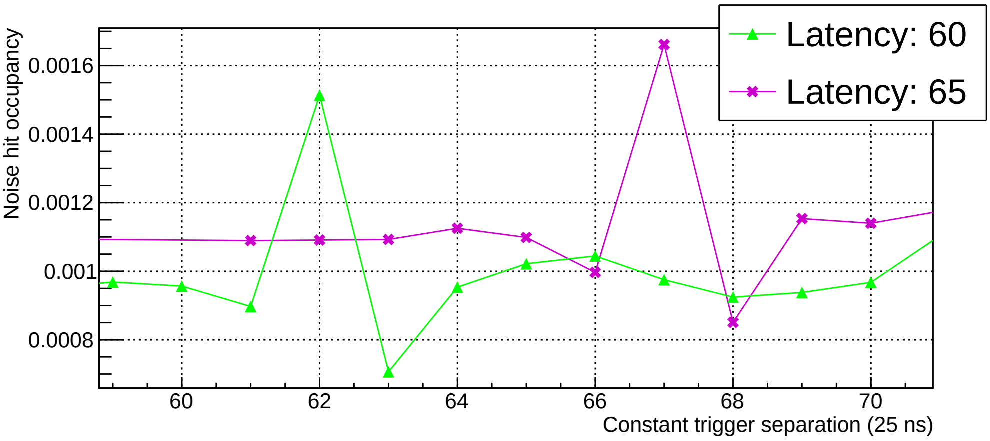

Figure 5.26.: Noise hit occupancy depending on trigger separation and latency settings.

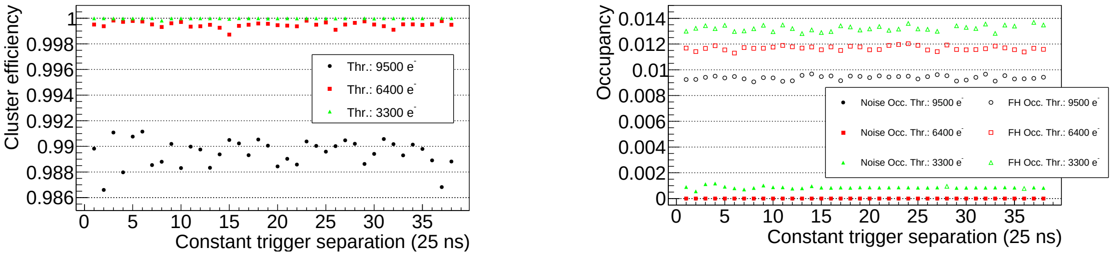

(a) Cluster efficiency **(b)** Fake and noise hit occupancy

Figure 5.27.: Cluster efficiency, fake hit occupancy and noise hit occupancy measurements depending on constant trigger separations below 38 bunch crossings and varying thresholds between 3300 e^- and 9500 e^-.

trigger signal is received. Nevertheless, the effect is marginal and does not impair the cluster readout as shown in Figure 5.24.

5.7.2. Semi-constant Trigger Rates above 1.05 MHz

The method shown in Section 5.7.1 cannot be used to evaluate effects of trigger separations below 38 bunch crossing because this would cause a buffer overflow on the CBC. To still be able to investigate possible effects caused by certain trigger separations below 38 bunch crossings only two consecutive trigger signals, followed by a larger gap, are send to the chip. This avoids a buffer overflow, since the mean trigger rate is below 1.05 MHz.

The pattern list contains a pair of two closely spaced triggers while each pair of triggers is separated by 600 bunch crossings. This results in a ring buffer state of the CBC that does not contain any triggered event before the next pair of triggers is sent. The gap within a pair is reduced from 38 to 1 bunch crossing. Again, the cluster efficiency, fake hit and noise hit occupancy are measured for the same three threshold settings as before. The results are shown in Figure 5.27. They do not show any dependence on the trigger separation.

5.7.3. Poisson-distributed Trigger Signals

While CMS is taking data, the probability of each bunch crossing to be triggered is identical. This leads to trigger signals following a Poisson distribution. To evaluate the CBC3.1 performance under conditions closer to the experiment the measurements done in Section 5.7.1 are repeated for pattern lists having Poisson-distributed trigger signals. Therefore, the distribution of the separation between two triggers follows an exponential distribution. The mean trigger separations are varied between 100 and 45 bunch crossings, which corresponds to mean trigger rates of 400 kHz to nearly 900 kHz. A value of 45 is chosen as the lower limit for the trigger separation to avoid possible buffer overflow on the chip having an over-average rate of trigger signals for a short amount of time as discussed in Section 5.7.4.

Figure 5.28 shows the cluster efficiency depending on the mean trigger separation and threshold setting. As expected, the efficiency decreases with increasing threshold. Again the noise and fake hit occupancy are also measured, which is shown in Figure 5.28b. Compared to the measurements with constant trigger separations, the measurement with trigger signals distributed with a Poisson distribution are closer to the later detector operation. Therefore, it is of most importance that the values are not affected by the mean trigger separation. This is confirmed with the constant behaviour shown in Figure 5.28 and Figure 5.28b. Together with

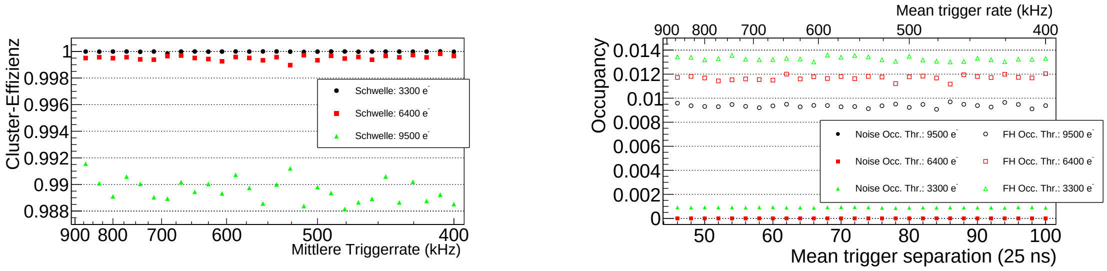

(a) Cluster efficiency.

(b) Fake and noise hit occupancy

Figure 5.28.: Cluster efficiency, fake hit occupancy and noise hit occupancy measurements depending on average trigger separations between 45 and 100 bunch crossings and varying thresholds between 3300 e^- and 9500 e^-.

the results obtained in Section 5.7.1 a flawless chip readout under high occupancy input at high trigger rates from 400 kHz to 1.05 MHz and in short time periods to up to 40 MHz is validated.

5.7.4. Poisson-distributed Trigger Rates above 1.05 MHz

So far the CBC was triggered with rates within its design specifications and showed no sign of inefficiency in the readout. This section covers a study that investigates what happens when the CBC is operated outside its design specifications.

Figure 5.29 shows the data handling between the memory blocks of the CBC. Once it receives a trigger, the event requested is copied from the 512 events deep ring buffer into a 32 events deep buffer where it is stored until it is sent out. This means that the CBC is able to cope with 32 consecutive triggers without any data loss occurring. It takes 38 bunch crossings for the CBC to send out the serialised hit data on one data line at 320 MHz. Therefore, as stated in Section 5.7.1, the CBC can be read out with a maximum constant trigger frequency of 1.05 MHz.

If the output memory is fully occupied and additional triggers are received, the next event will overwrite an event which has not yet been sent out. The write pointer for the event storage increments repeatedly from 0 to 31. E.g. by sending 34 consecutive trigger the following happens: Until the 32nd trigger the buffer is filled from the bottom row to the top row. The first event in the first row has already moved on to the serialiser for its output. Therefore, the first row is available to store the event from trigger number 33. But the event with trigger number 34 will overwrite event number 2 on the second row of the buffer. The output in terms of triggered event numbers results in 1, 34, 3, 4, 5, etc. and therefore event number 2 is lost, which is also indicated by an activated buffer overflow error flag.

Within the serialiser each event gets two header bits, two error flags and an event count, called Level 1 Accept (L1A) counter. The L1A counter is increased with each trigger signal received and iterates from 0 to 511. It can be reset with a fast command called Orbit Reset. This is sent each time the LHC beam has made a full revolution. This counter validates the synchronous readout of all chips within the tracker. A buffer overflow is indicated by the error flags in the event header.

Even with mean trigger rates of 750 kHz, buffer overflows can occur due to the fact that the trigger signals follows a Poisson distribution, which results in finite probabilities to have higher trigger rates on short term periods. Therefore, the buffer states have to be always monitored by tracking the number of triggers over time, and a trigger veto should be set if a trigger would cause a buffer overflow. In the current CMS tracker this was realised by the Trigger Throttling System [Tau+10].

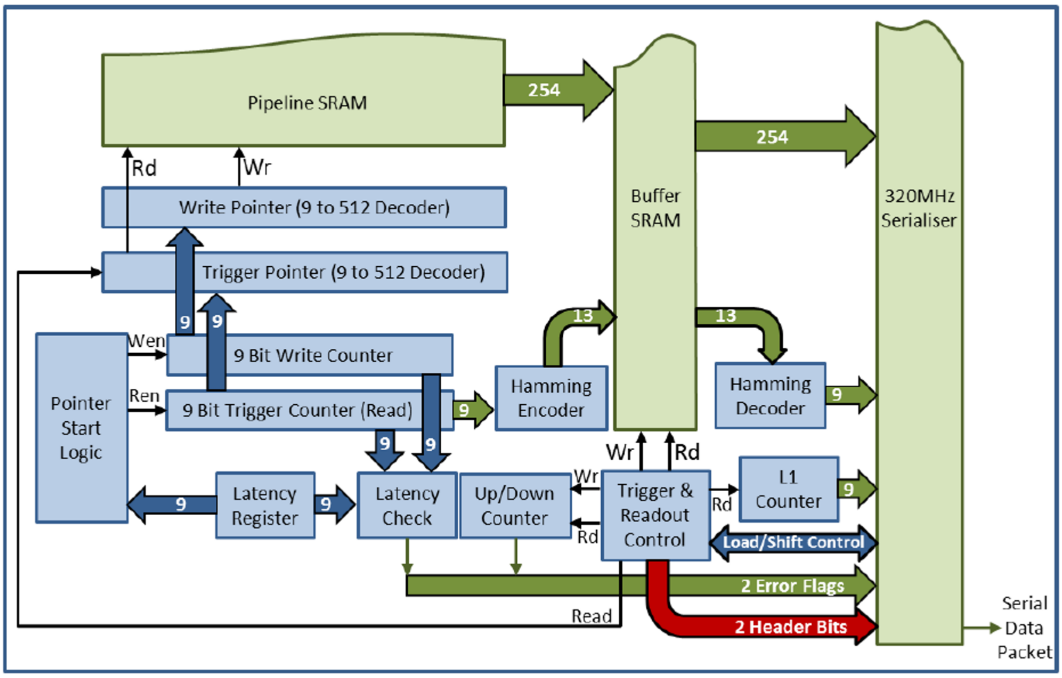

Figure 5.29.: CBC Memory block diagram. All events recorded are first stored in the 512 deep Pipeline SRAM. All triggered events are moved to a 32 event deep Buffer SRAM. Afterwards the event header is added and are serialised before they are sent out at 320 MHz [Pry19]

The explained behaviour result in an event output that is not sorted chronological but still each event has its own L1A count information. Therefore, this information could be used to reconstruct the correct sequence of events that are read out. In the analysis of the KARATE readout this is realised with a sorting algorithm putting the events in the right order and tagging the events lost. This makes it possible to still perform efficiency studies in case of a data loss caused by a buffer overflow. In addition to this, the buffer state is reconstructed using the chronology of trigger commands that is recovered using the information stored in the pattern list.

Figure 5.30 shows the buffer state for all triggered events. Because the trigger signals are distributed according to a Poisson distribution with a mean trigger rate of 1 MHz the buffer state fluctuates over time and at some point it exceeds a value of 32 causing a buffer overflow. Figure 5.30 also shows the event efficiency for the same measurement which is defined as 0 for events lost, meaning a skipped L1A count in the event vector after the sorting algorithm, and 1 for events available. It is visible that once a buffer overflow occurs, the event 32 bunch crossings earlier is overwritten and thus lost, as expected.

So far the sorting algorithm could be used to reconstruct the correct event order even in the state of a buffer overflow. Unfortunately, it is observed that the behaviour of the chip under such high trigger conditions is not stable. The efficiency to detect the hits for each event suddenly drops after several thousands of triggers. It seems that in this case the L1A count is not linked correctly to the corresponding event in the buffer. As a result the read out event is compared to the wrong injection pattern which yields in a reconstruction efficiency of almost 0.

By shifting the compared KARATE events and CBC events with respect to each other, the matching event comparison can be regained. But after several hundreds of events the L1A counter skips again and the efficiency drops to 0 again. This shows that the merging of the L1A count and the hit data is not stable when the CBC is operated beyond its technical

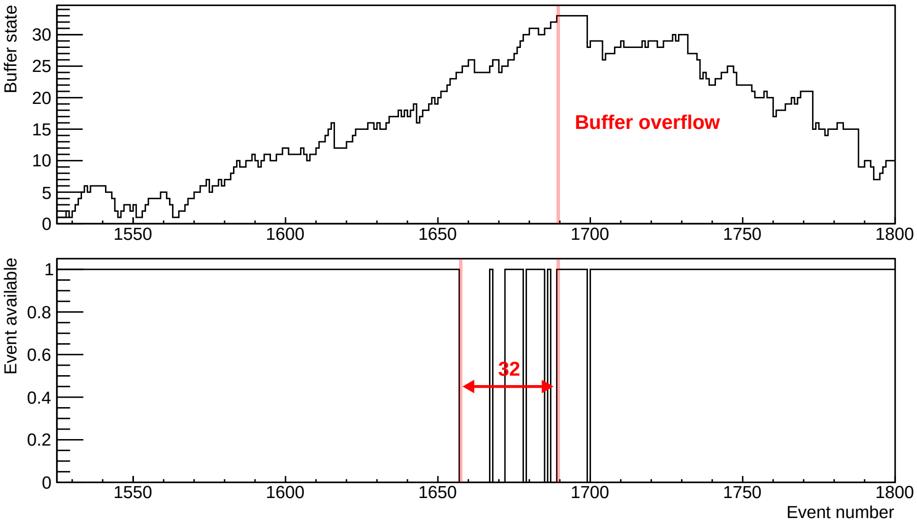

Figure 5.30.: The top figure shows the CBC buffer state during data taking with Poisson-distributed triggers with a mean rate of 1 MHz. On the bottom the available events are shown for the same measurements. Available events are indicated with 1 while lost events are tagged with 0. The buffer overflow is marked in red. The first event lost is located 32 events before the buffer overflow.

specifications under high trigger rates above 1.05 MHz. This affirms that a buffer overflow on the readout chip should be prevented at any time during the detector operation.

5.8. Track Inclination and Stubs

Key functionality of the CBC is the discrimination of passing particles based on their transverse momentum. Particles crossing the module generate a signal in both of the two sensors, called seed and correlation layer. The hit position in the seed layer together with the programmable window size and offset defines a window of channels in the correlation layer. If the signal in the correlation layer is within this window a stub is created on the chip, containing the seed position and the offset to the hit in the correlation layer, called bend. The window is adjustable to a size of up to ±7 channels. To compensate geometric effects of modules that are not oriented perpendicular towards the interaction point an additional offset of up to ±3 channels between the seed and the correlation window can be adjusted for four separate regions on the chip settings. In addition to the window and offset settings, an upper limit of the size of the clusters within a stub can be defined, because high cluster sizes hint to particles with high incident angles and thus low p_T particles. The step-size of the settings is in half channels, since this is the possible resolution in a binary readout system. The information of up to three stubs per CBC and bunch crossing is sent out at 320 MHz. Each chip shares signal lines with its neighbours to avoid stub inefficiencies in the inter chip region. The stub logic was proven to work in beam tests under low occupancy and trigger rates [Upl19]..

To evaluate the stub efficiency on high occupancy and trigger rates, patterns with varying angles, and thus resulting bends, are injected into the system. Further, two correlation windows, 3.5 and 7 channels, were chosen to verify the sensitivity on the differing bend values. The KARATE system is attached to 24 channels of the first and to 24 channels of the second CBC of an 8CBC3.1 hybrid. This enables to also test the inter-chip communication under these conditions.

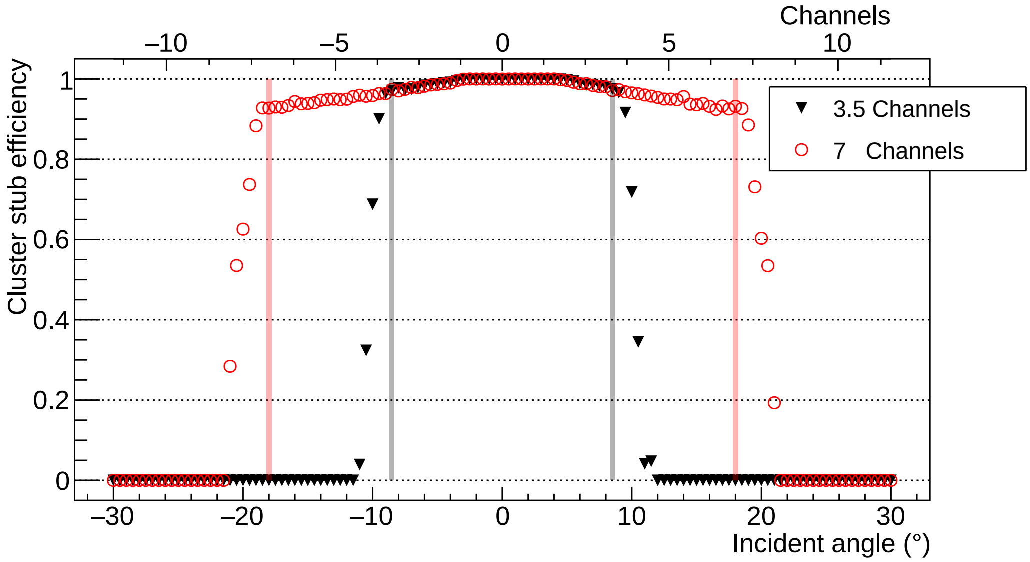

Figure 5.31.: Cluster stub efficiency depending on tracks with varying incident angles and a varying correlation window setting. Once the incident angle exceeds the geometric acceptance of the stub logic indicated by the grey and red lines the efficiency drops to zero.

The cluster signal is again set to 22 000 e^- for tracks crossing the sensors perpendicular and the mean trigger rate is set to 750 kHz. The cluster signal will increase with the inclination of the tracks due to the longer trajectory modelled inside the silicon sensor. The track density is set to 10 MHz/cm^2, which resembles an average probability of 0.27 for an event to contain a track in the instrumented area. An additional constraint is set only allowing a maximum of one track per event. This prevents the generation of additional stubs caused by two tracks which would not create a stub on their own because their inclination angle is too high. The analysis compares all injected stubs with the stub output in the event readout. A detected stub is valid if its seed position is within ±1.5 strips compared to the injected stub seed cluster. Additionally the bend value has to be within ±2.5 strips. The efficiency to reconstruct stubs is defined as

$$\text{Cluster stub efficiency} = 1 - \frac{\text{Invalid or lost stubs}}{\text{Injected stubs}}, \tag{5.6}$$

and is measured while the track inclination is increased from $-30\,°$ to $30\,°$ for two different correlation windows of 3.5 and 7 channels. Figure 5.31 shows the result of the measurement. As expected there is a distinct drop outside the geometric acceptance window of the stub logic which is, in case of a 1.8 mm module, reached by angles of $\pm 8.5\,°$ and $\pm 18\,°$.

For larger inclinations above $5\,°$ the efficiency plateau within the correlation window starts to decrease creating a shoulder. This results from fake hits impairing a correct reconstruction of the injected stubs. The larger the search window is the higher is the probability to detect a fake hit in it. Visualized in Figure 5.32, the stub logic prioritizes stubs with lower bends and thus the original injected ones might get lost.

Figure 5.33 shows all bend values of the stubs recorded depending on the incident angle of the injected signals. The larger the track inclination the higher is the probability to get stubs with a lower bend value due to fake hits, visible as the light green areas. The bend value reaches from 0 to 7 for positively inclined tracks and from 15 down to 9 for negatively inclined tracks. Therefore, the bend value 15 is adjacent to 0. The bend values arise from the default values stored in a look-up table on the chip which is used to translate the original 5-bit bend

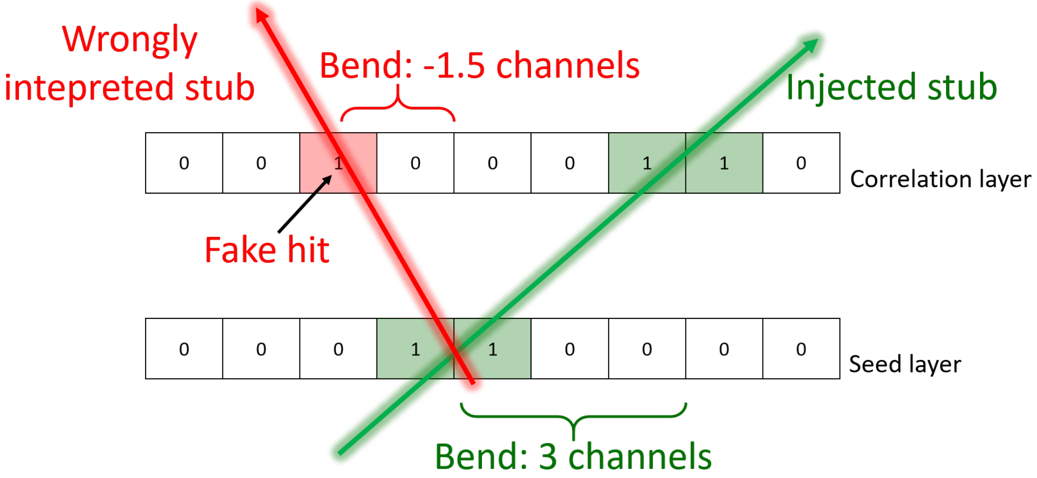

Figure 5.32.: Effect of fake hits on the stub detection. Fake hits occurring in the seed or correlation window which result in an altered bend value or seed position of a recorded stub decreasing the overall stub detection efficiency.

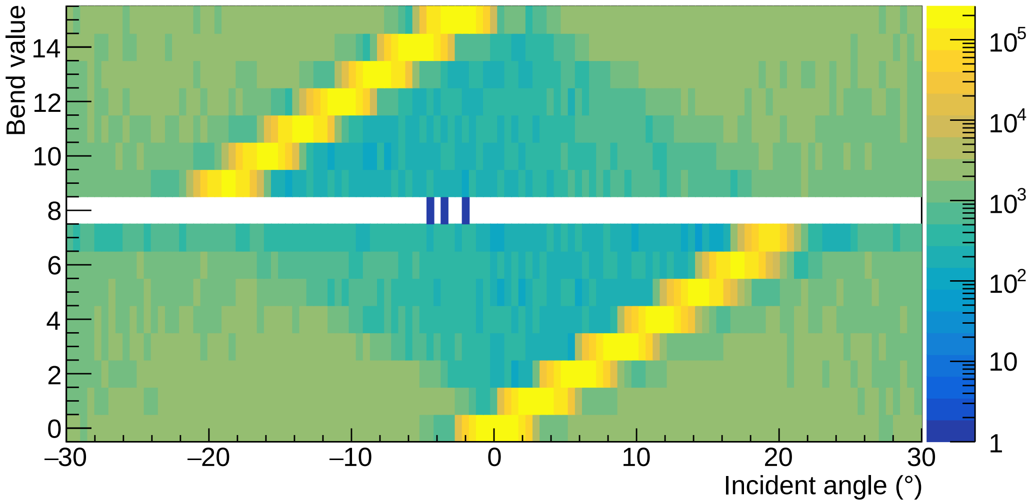

Figure 5.33.: Bend values of all recorded stubs for different track inclinations.

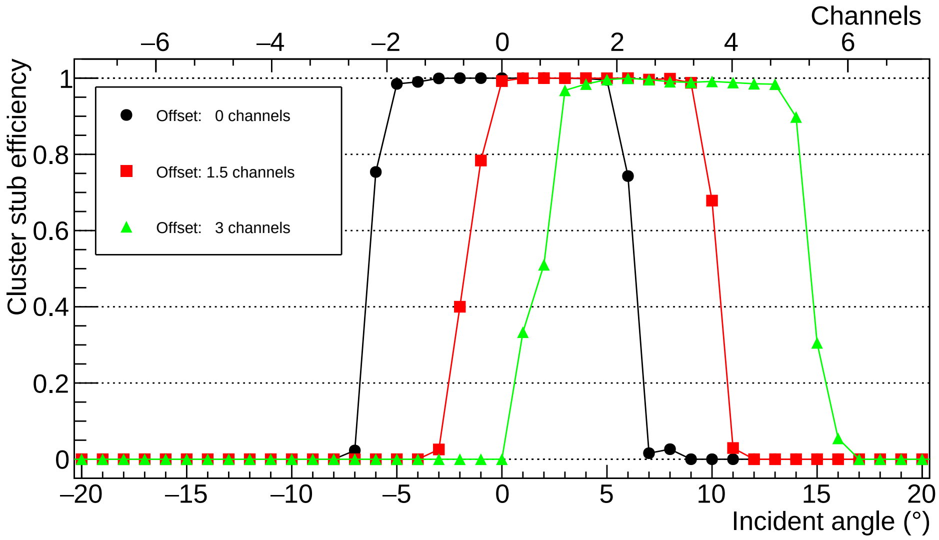

Figure 5.34.: Cluster stub efficiency with varying correlation window offset settings.

value to a 4-bit bend value reducing the data output. Bend value 8 is reserved to indicate faulty stub reconstructions in the logic. Within the correlation window the mean bend values match the expectation very well. Outside the correlation window the stubs are created randomly by fake hits.

Depending on the position of the module inside the tracker an offset between the seed and correlation layer can be added to the stub logic to compensate geometric effects. On a 1.8 mm module this refers to about ±12 °. Figure 5.34 shows a measurement with three different offset settings. Again the cluster signal was set to 22 000 e^- for perpendicular tracks, the threshold to 4700 e^- and the track density to 10 MHz/cm^2 constrained to one track per event.

As expected the efficiency plateau of the cluster stub finding shifts with the offset according to the geometric acceptance. The effect of decreased shoulders as seen in Figure 5.31 is not that imminent, because the correlation window was set to 3 channels.

The high rate studies on the cluster stub efficiency verify a valid functionality of the CBC also at high track densities and trigger rates. Also no problem in the inter-chip communication is observed.

5.9. Noise Studies at High Occupancies

The noise of the analogue front-end of a CBC channel is mainly driven by the thermal noise of the attached capacitance. The KARATE system is used to investigate in detail the noise behaviour of the CBC under a high occupancy input.

5.9.1. Comparison Between Idle and Occupied Front-end

As already shown in Section 4.9.2, the noise of a channels is derived by determining the width of the Gaussian shaped function which is the derivative of an occupancy threshold scan. It is assumed that the noise of an idle front-end underlies Gaussian statistics. To compare it with high occupancy measurements the threshold scan of an idle front-end is repeated with high statistics. As shown in Figure 5.35 it deviates from the theoretical expectation of an complementary Error function, which is expected by the measured noise in Section 5.3.1. The deviations show that the noise does not exactly follow Gaussian statistics but has an increased

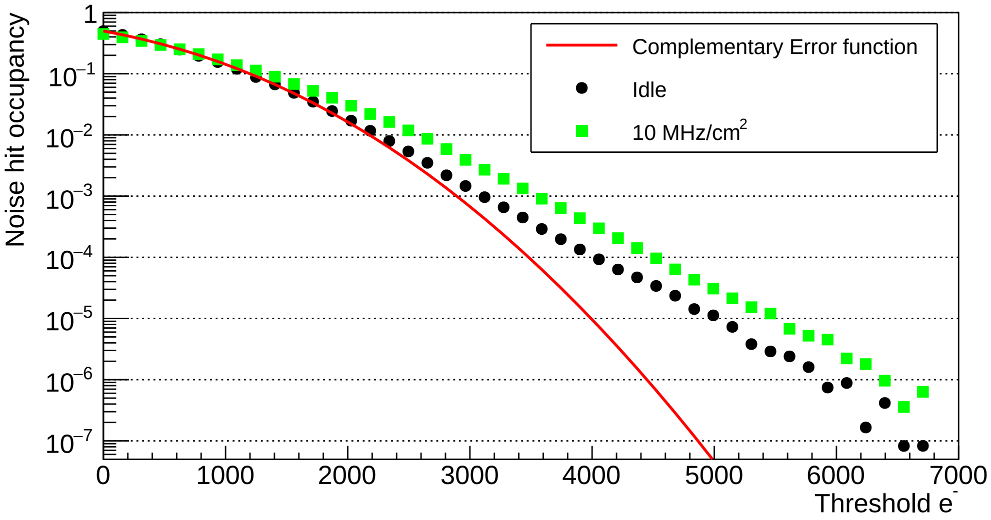

Figure 5.35.: Comparison between a noise occupancy measurement depending on the threshold for an idle and occupied front-end. The red curve shows the theoretical Error function for the noise measured during commissioning.

tail towards higher thresholds. Nevertheless, the deviations are small and thus do not impair the detection efficiency. Figure 5.35 also shows the noise hit occupancy measured in channels in which no signals is awaited while the systems detects hits with a track density of 10 MHz/cm². It seems that the charge injection affects the noise behaviour of the system. This is further evaluated in the following subsection.

5.9.2. Noise depending on the Track Density

As a next step the KARATE system is used to study the noise behaviour while the CBC detects hits. The noise hit occupancy is measured while the track density, and thus the occupancy, is increased for different threshold settings. The tracks injected are perpendicularly oriented and have a cluster signal of 22 000 e^-. The threshold is varied in steps of 312 e^- between 4840 e^- and 3280 e^- and the track density is varied from 0 to 30 MHz/cm². The trigger signals are again separated according to a Poisson distribution with an average trigger rate of 750 kHz.

The measurement at 0 MHz/cm² refers to the results obtained in Section 5.9.1 for an idle front-end. Once patterns containing tracks are injected, the noise hit occupancy increases. The results are shown in Figure 5.36 and reveal a steep increase between 0 and 1 MHz/cm². Above 1 MHz/cm² the correlation between the noise hit occupancy and the track density becomes linear. The higher the signal injection rate the higher is the possibility to detect noise hits. It is assumed that the permanent injection increases the overall baseline fluctuation resulting in a higher noise hit occupancy.

These results indicate that for the detector operation the threshold should not be solely determined by the noise measurement during commissioning. Depending on the targeted noise hit occupancy during detector operation the occupancy of the system has to be considered as well to adjust a suitable threshold. Nevertheless, the results also show that the noise hit occupancy does not reach a critical region as long as the threshold is set to reasonable levels, which should be around 4000 e^- to 5000 e^-.

Further studies should evaluate whether this behaviour scales with channels instrumented or if it only affects the channels locally.

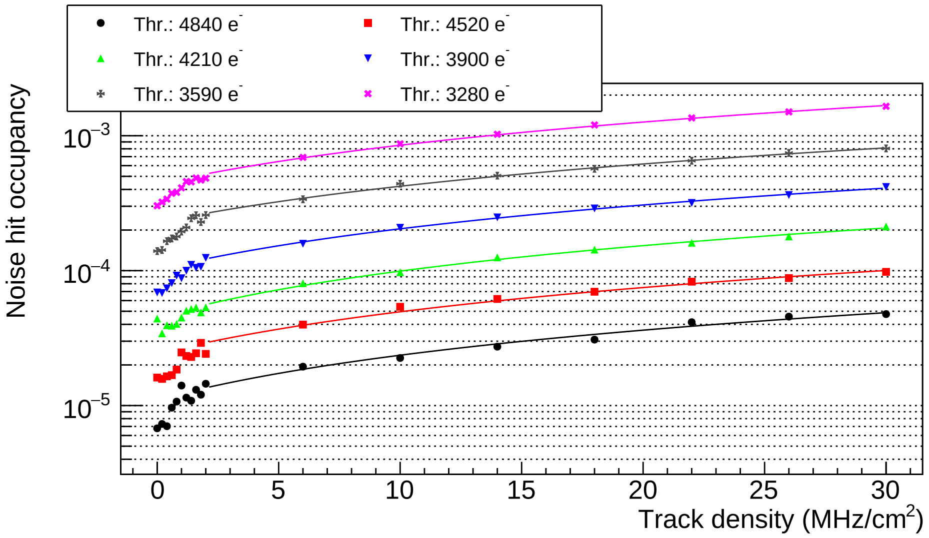

Figure 5.36.: Effect of increasing track densities on the front-end noise of the CBC for different thresholds. The cluster signal is set to 22 000 e⁻ and the tracks are orientated perpendicular. The mean trigger rate is 750 kHz.

5.9.3. Time Dependence

The measurement with the highest noise occupancy and lowest threshold obtained in Figure 5.36 is used to further investigate the noise behaviour of the system. Figure 5.37 shows three distributions: The red distribution shows the time distances in bunch crossings between two hits on a channel of the injection pattern list. As expected it follows an exponential distribution with a mean value of 20.8 bunch crossings, which refers to the injection occupancy of 0.048. The blue histogram shows all time distances between a noise hit on a channel and the preceding injection hit. The measured noise hit occupancy is 1.6×10^{-3}. The red histogram is scaled to the blue histogram with a factor of

$$\frac{\text{Noise hit occupancy}}{\text{Injection occupancy}} = \frac{1.6 \times 10^{-3}}{0.048}, \tag{5.7}$$

because there are more injection hits than noise hits. The green histogram also shows the distribution of time distances between two injected hits but it is normalised with a factor of $2.5 \times 10^{-3}/0.048$, to overlay the green distribution with the blue distribution for time distances above 20 bunch crossings.

Assuming that the probability of a noise hit to be detected is constant over time, the periods between a noise hit and a previous injection should also be distributed according to a exponential distribution with a mean value of 20.8 as they are for the red and green distribution. But for the noise hit - signal hit distribution this is not the case. It is visible that the probability of a noise hit to be detected decreases if a hit was injected within 15 bunch crossings before the triggered event.

As discussed for the reconstruction of a single pulse in Section 5.3.3, the undershoot of the baseline after a pulse injection can be more than 300 ns. During this, the pedestal is shifted and the probability of a noise hit to occur decreases. Figure 5.37 shows that it takes up to 20 bunch crossings, equivalent to 500 ns, to fully mitigate the effect of an injection on the noise hit probability.

Due to the influence of the undershoot on the effective noise hit probability, the noise hit - signal hit distribution can be separated in two regions before and after periods of 20 bunch

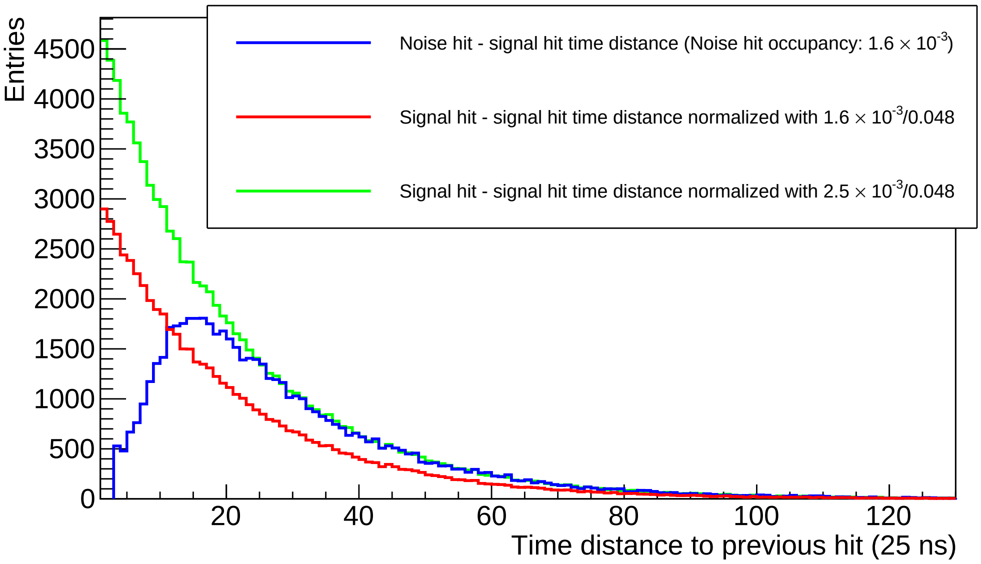

Figure 5.37.: Distribution of time distance in bunch crossings between two injected hits (red and green) and between noise hits and injected hits (blue).

crossings. Normalizing the signal hit - signal hit distribution to the noise hit - signal hit distribution in the range of 20 to 200 bunch crossings reveals that the noise hit occupancy without the undershoot effect is 2.5×10^{-3} instead of the measured effective noise hit occupancy of 1.6×10^{-3}. This is indicated by the green histogram.

This analysis shows that the noise is not a static condition of the system. In addition to the occupancy dependence described in Section 5.9.2, it also depends on the time since the last signal detection. The subsequent signal undershoot decreases the effective noise hit occupancy. For channels being idle for more than 500 ns the probability to detect a noise hit is higher than the measured noise hit occupancy.

5.10. Decreased Cluster Signals

In the previous measurements the cluster signal was set to be $22\,000\,\mathrm{e}^-$ for perpendicular oriented tracks. During the operation lifetime of the detector the charge collection efficiency of the silicon sensors degrade. By higher irradiation levels additional energy levels in the silicon lattice form and cause charge trapping. In a worst case scenario, which depends on various parameters, it is expected that the cluster signal decreases down to $17\,000\,\mathrm{e}^-$. This scenario only applies for a small number of 2S modules located on the TEDD most closely to the beam pipe.

The KARATE system is used to evaluate the hit reconstruction efficiency with varying cluster signals emulating different levels of irradiation. The range reaches from $22\,000\mathrm{e}^-$ down to $15\,000\mathrm{e}^-$. As before, the measurement is done for three threshold settings. The cluster efficiency measured is shown in Figure 5.38. As expected, it decreases with lower cluster signals. But even with a cluster signal of $15\,000\,\mathrm{e}^-$ which corresponds to a fluence of above $3 \times 10^{14}\,\frac{\mathrm{n_{eq}}}{\mathrm{cm}^2}$ [AAC10], the cluster efficiency is well above 99 %.

This measurement only gives an estimation of the detection efficiency and does not consider all effects prevalent in the silicon sensor caused by irradiation. For further studies the model

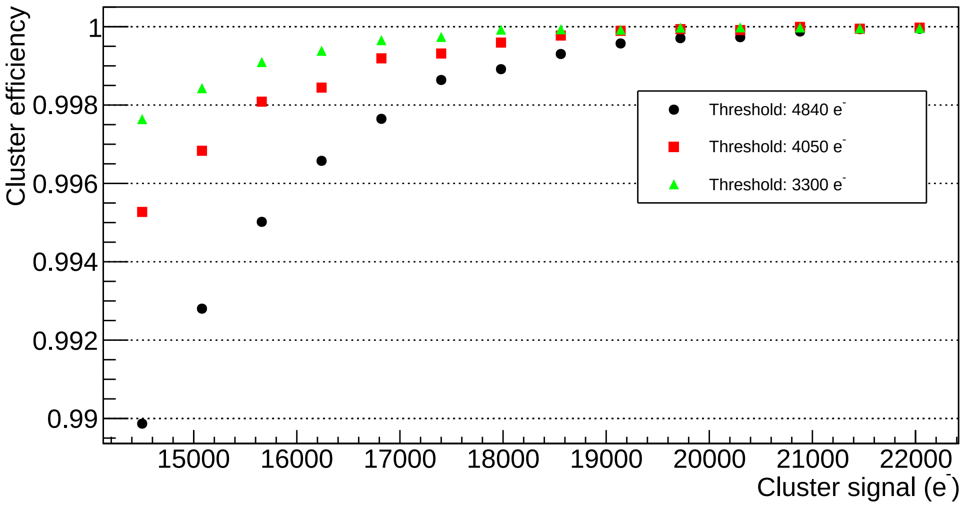

Figure 5.38.: Cluster efficiency depending on the cluster signal for perpendicularly oriented tracks.

developed in Section 5.5 has to be adapted and tuned to data obtained with irradiated silicon sensors.

5.11. Monte Carlo-based injection samples

So far the model used to generate the injection patterns for the KARATE system was based on tracks creating cluster signals in the two sensor layers. The parameters for realistic signal amplitude distribution were tuned with data obtained in a beam test, as described in Section 5.5.

Within the running experiment the particles crossing the tracker do not always originate from the interaction point. Low p_T particles can travel through the detector forced on loops. Also particles from secondary vertices inside the tracker or interactions in the ECAL do not always have a preferred direction. Therefore, the mean cluster size of the signals generated will not be constrained to a few channels as they are generated by the model introduced in Section 5.5.

To have a more realistic signal emulation a first attempt was made to inject Monte-Carlo based patterns. The complex environment within the detector can be simulated using the software package CMSSW [Col19a], which is developed for analyses and simulations for CMS. With CMSSW, events from proton-proton collisions can be simulated using Monte-Carlo event generators. The interaction of the emerging particles with the material in the detector volume is modelled with Geant [Ago+03] using the new tracker layout of the Phase 2 upgrade. The interactions happen in both, active and inactive detector volumes. Active volumes represent components in which the energy deposition causes a measurable signal such as within a silicon sensor. The subsequent digitization process converts this energy deposition to the binary hit information as it is sent out by p_T-trigger modules. The result of such a simulated event can be written in a text file containing all the hits and their location inside the tracker encoded with a module number.

The event samples used were provided by Sebastien Viret from CNRS Lyon and contained 48 events of inelastic proton-proton collisions with minimal requirement on detectability, called minimum-bias events. The events contain the whole hit information of all modules located on layer 8 of the future CMS Outer Tracker for a mean pile-up of 200 and 300. To gain statistics

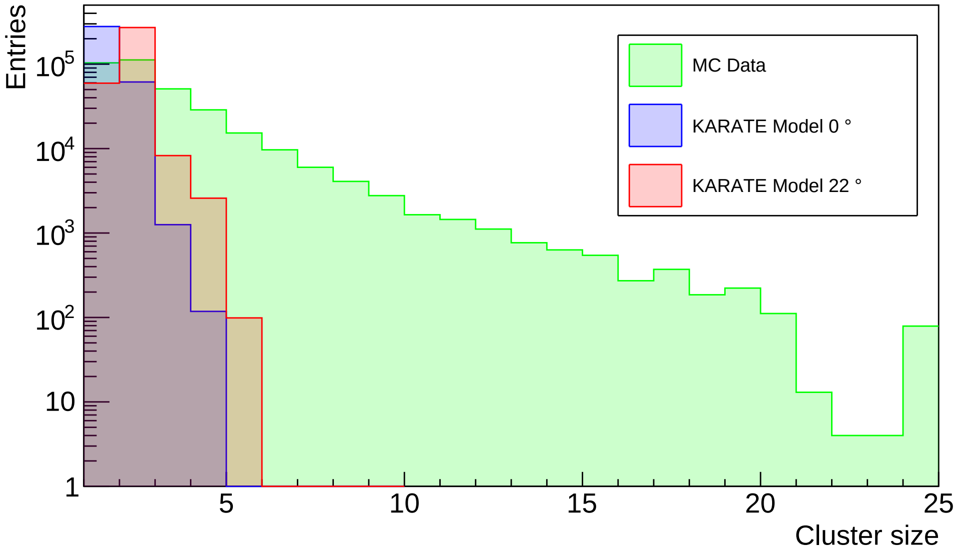

Figure 5.39.: Cluster size distribution for injection patterns obtained from Monte-Carlo-based events generated with the CMSSW software package compared to the distribution resulting from the track-based model introduced in Section 5.5 for two different track angles.

each module within each event was split in areas of 2 × 24 channels and each area is treated as an individual injection pattern. Therefore, the injection patterns do not reflect the real conditions of a module mounted at a certain position within the CMS detector but in minimum bias events no significant local excess hits, such as high-p_T jets, are expected. The digitization process has already translated the analogue signal information in binary hit information. Therefore, the pattern injection should be in such a way that each entry in the hit pattern generates a detectable hit in the CBC. For each entry in the hit pattern a signal of $22\,000\,e^-$ is injected into the corresponding channel. The trigger signals are distributed according to a Poisson distribution with a mean value of 53 among the generated events resulting in an average trigger frequency of 750 kHz. With a reasonable threshold setting of $5000\,e^-$ the hit efficiency is 1, meaning that not a single hit was missed. Of more interest is the distribution of cluster sizes. Shown in Figure 5.39, an exponential decrease in the cluster size is visible. With the KARATE system the largest clusters that can be detected have 24 channels. The overflow in the last bin shows that there would have been even higher cluster sizes, indicating particles that nearly cross the silicon sensor horizontally.

Figure 5.39 also shows the difference in the cluster size distribution between the model developed in Section 5.5 for two different track angles and the expected environment within the CMS tracker resulting from the Monte-Carlo generated events. The model introduced Section 5.5 does not consider secondary vertices or scattered particles and therefore the cluster size solely scales with the track inclination setting, as shown in Figure 5.20. It is advantageous to make statements about the high rate detection efficiency depending on the particles directions and the cluster signal heights as it is done in beam tests or lab measurements using ^{90}Sr sources. Testing the stub detection logic also requires are preferred track orientation. But for a future improvement beyond the scope of this thesis the Monte-Carlo-based injection samples should contain the energy deposition in the sensor volume. Additionally, the statistics has to be increased in such a way that the varying environments for modules sitting at different places inside the detector can be investigated.

5.12. Summary

The future Outer Tracker of the CMS detector will consist of p_T-trigger modules. The outermost region will be equipped with 2S modules. The readout chain of a 2S module consists of CBCs connected to CICs, which forward the hit and trigger information to the LpGBT. The LpGBT serialises the data and sends it to the back-end via an optical link.

This readout chain has to cope with average track densities of up to 15 MHz/cm^2 and average trigger rates of up to 750 kHz. A new test system, called KARATE, was developed in the scope of this thesis, because beam tests or measurements with radioactive sources do not meet these requirements. With a combination of LEDs and photodiodes, controlled signal patterns can be injected into the CBC's front-end at 40 MHz. Each pattern can be tagged with a trigger signal and each pulse injection can have 16 different amplitudes.

A model was developed to emulate the Landau-distributed signals as they are expected to be detected in a silicon strip sensor also considering charge sharing. The parameters of the model are tuned using data obtained in a beam test performed by the CMS collaboration in 2018.

The CBC is the only currently available part of the 2S module readout chain that can be tested within the KARATE system. Various measurements were performed to investigate the performance of the chip at high trigger and occupancy rates. These measurements include a study on the influence of the hybrid's signal routing on the cross-talk between adjacent channels. It was found that the cross-talk has a maximum value of 2.1 % for adjacent channels on the fold-over side of the hybrid, because of the longer signals lines.

High rate studies demonstrate the operability of the CBC under high occupancy and trigger rates. As expected, the cluster efficiency is slightly affected by the recorded track density due to the increased rate of fake hits. For reasonable thresholds and track densities the effect is negligible. A possible dependence of the cluster efficiency on the trigger rates was investigated. The results show flawless operability of the chip in reasonable threshold settings and trigger rates within the CBCs design specifications. Also the stub finding logic was validated under high track densities and trigger rates. Investigating the noise of an idle CBC with high statistics reveals that it deviates from Gaussian statistics at higher thresholds. In addition to this it was found that the noise hit occupancy depends on the track density. Due to the undershoot of a channel's baseline after detecting a signal the probability to detect a noise hit decreases in this period. The effect of decreased cluster signals due to increased radiation levels of silicon sensors were investigated. Even with the expected degraded cluster signal of 17 000 e^- after the operation life time of the detector the efficiency stays well above 99 %. A first attempt was made to inject Monte-Carlo-based patterns, to have a more realistic emulation of the environment of the future Outer Tracker.

Overall the KARATE system offers a wide range of possible measurements. Due to the synchronous injection and readout the behaviour of the system can be studied in great detail. Due to the large set of parameters the phase space for possible measurements is by far not exhausted with the results presented in this thesis. In addition to this, future upgrades of the system will include the CIC, LpGBT and VTRx+ to finalized the 2S module readout chain, with which further tests will be performed.

Part III.

Summary and Outlook

6

Summary and Outlook

By 2026 the HL-LHC will start to operate at five times higher luminosities compared to the design luminosity of the LHC. This results in higher particle rates inside the experiments. To cope with the new environment of the HL-LHC, the CMS detector will undergo major upgrades. Within the Phase 2 Upgrade the complete tracking detector will be replaced by a new enhanced version. The new tracker will be separated in an inner part consisting of silicon pixel modules and the outer region consisting of modules having silicon macro-pixel and strip sensors.

A key element of the future CMS detector is the contribution of tracking data to the first level trigger decision. For this, each module in the Outer Tracker discriminates crossing charged particles based on their transverse momentum, providing an on-module data filtering for high-p_T particles to reduce the readout bandwidth significantly by hinting to events of interest. The p_T-trigger modules consist of two closely spaced silicon sensors. The trajectory of a high-p_T particle is less bent in the magnetic field and therefore the signals in the two silicon sensors are tightly aligned in space. This correlation is detected as a so called stub by a dedicated logic on the readout chip which is connected to both sensors. The stub information of high-p_T particles will be sent out at 40 MHz.

The outermost region of the Outer Tracker will be equipped with 2S modules, which consist of two silicon strip sensors. The stub finding concept puts high requirements on the p_T-modules' assembly precision. The sensor strips have to be aligned with a maximum tilt angle of 400 µrad. This is realised using precise assembly jigs with alignment pins. In addition to this, the modules will be operated in a harsh radiation environment which requires the radiation hardness of the modules' components. The glue joints of a module have to be of a high quality to ensure a reliable operation at temperatures down to $-35\,^{\circ}\mathrm{C}$.

ETP pledged to build 2000 2S modules between 2021 and 2023. This results in an average module production of five modules per day. To compensate below average production periods ETP prepares for a peak production of eight modules per day. Therefore, the assembly of the modules has to be a well controlled and reliable process to keep the module quality high and the failure rate low.

ETP was the first production site to assemble a prototype 2S module outside the pilot center CERN. In the scope of this thesis several assembly and test stations were developed and commissioned for the use during the upcoming module production. A metrology station was set up to measure the parallelism between the sensors' dicing edge and strip implants using a five megapixel camera. All 2S sensors received from the manufacturer were within the specifications of 100 µrad. The metrology station also checks the alignment of the two silicon sensors within a bare-module with a laser-based distance measurement. All dummy and functional modules were within the specifications of 400 µrad. With a custom-made dispensing gantry a gluing procedure was developed to reliably attach the polyimide isolation to the sensor's backside, having almost perfect wetting, thin glue layer thicknesses down to 7 µm and no excess of glue. The development of a temperature-stabilized test station was supervised, with which it is possible to characterize the modules at temperatures down to $-20\,^{\circ}\mathrm{C}$ on the sensors and to validate the module quality during production. Irradiation studies of silicone-based wire-bond encapsulation material verify that it is suitable in the Outer Tracker at the expected fluence of $1 \times 10^{15}\,\frac{\mathrm{n_{eq}}}{\mathrm{cm}^2}$.

Two prototype 2S modules were built in 2018 and 2019. Both are within the assembly specifications and are fully functional. The low front-end noise is at the expected level of about $1000\,\mathrm{e}^-$, making it possible to detect particles emitted by a ^{90}Sr source.

Most of the components for the 2S module are still under development. Therefore, the adjustment of the assembly process will be ongoing as long as the components do not have their final design and functionalities. By the end of 2019, the production sites have been handed out the first functional versions of the service hybrid and front-end hybrids including the final version of the readout chip, the CBC3.1. In addition to this, an extension mezzanine containing the first version of the CIC can be attached to the front-end hybrids. This will result in the first prototype modules which resemble the same electric functionality of a final 2S module.

The CIC acts as data hub on the front-end hybrid concentrating the data coming from eight CBCs. The data stream of two CICs is forwarded to the LpGBT located on the service hybrid. The LpGBT serialises the data before it is sent out optically via the VTRx+ module. This readout chain has to cope with average track densities of up to $15\,\mathrm{MHz/cm^2}$ and trigger rates of up to 750 kHz. Beam tests or measurements with radioactive sources are not suitable to test the readout chain under those conditions. Within the scope of this thesis a new test system, called KARATE (KArlsruhe high RAte TEst), was developed at ETP. With a combination of LEDs and photodiodes, controlled signal patterns can be injected into the CBC's front-end at 40 MHz. Each pulse injection can have 16 different signal amplitudes and each pattern can be tagged with a trigger signal for the readout.

The system is able to emulate Landau-distributed signals as generated in a silicon strip sensor. A track-based signal generation model was developed, considering charge sharing between sensor strips. It was tuned with data obtained in a beam test performed by the CMS collaboration in 2018. The CBC is the only part of the 2S module readout chain currently available and was tested extensively within the KARATE system. Future upgrades will finalize the readout chain with the CIC, LpGBT and VTRx+ once the components become available.

Various measurements presented in this thesis validate the performance of the CBC at high occupancies and trigger rates. This includes a study on the influence of the hybrid's signal routing on the cross-talk between adjacent channels at a pulse injection rate of 400 kHz, mimicking a single channel occupancy of 1 %. For top channel injections the cross-talk on adjacent channels is 1.6 % with respect to the injection signal. On bottom channels this value is higher with 2.1 %, which is caused by the longer signal path lengths in the hybrids fold-over from the bottom to the top-side.

The CBCs detection efficiency is validated under various conditions such as track density, threshold, trigger rates and signal heights. The cluster detection efficiency is slightly impaired by hits from previous injections whose signal amplitudes stay above the threshold for multiple clock cycles. Nevertheless, the effect is negligible for thresholds and track densities as expected in the final experiment. Various measurements show no dependence of the efficiency on the trigger rate, as long as the trigger rate is not exceeding the CBC specifications. Also the stub finding logic was validated under high track densities and trigger rates.

The comparison of the noise behaviour of an idle CBC front-end to a scenario at high track densities shows an increase of the noise hit occupancy once the CBC detects hits. A linear correlation between the noise hit occupancy and track density has been observed. Additionally, it is shown that the probability of detecting a noise hit depends on the time since when the last hit was detected on the same channel. This effect is explained by the undershoot of the baseline after detecting a signal.

The effect on the cluster detection efficiency of decreased cluster signals due to increased radiation levels of silicon sensors is investigated. Even with the expected reduction of the cluster signal from $22\,000\,\mathrm{e}^-$ to $17\,000\,\mathrm{e}^-$, the efficiency stays well above $99\,\%$.

A first attempt was made to inject detector simulation-based hit patterns, to emulate the environment in the future CMS Outer tracker more realistically. The hit information is binary because the pattern output has already undergone a digitization process and therefore the model introduced in Section 5.5 cannot be used. As expected, the cluster size distribution between the Monte-Carlo generated hit patterns and the module introduced in Section 5.5 differs, because the track-based model does not consider secondary vertices or scattered particles. The track-based model is advantageous to make statements about the high rate detection efficiency depending on the particles directions and the cluster signal heights as it is done in beam tests or lab measurements using ^{90}Sr sources. For following implementations the patterns generated with the detector simulation should contain the analogue signal deposited in the active detector volume, which needs to be extracted before the digitization process of the signals in the CMSSW software package.

The KARATE system offers a wide range of possible measurements. Due to the synchronous injection and readout various aspects of the system performance can be studied in detail. Due to the large set of parameters the phase space for possible measurements is by far not exhausted with the results presented in this thesis. In addition to this, further measurements will follow as soon as the system is upgraded with the CIC, LpGBT and VTRx+ to finalize the 2S module readout chain to mimic the environment as close as possible to the expected environment in the Phase 2 CMS Outer Tracker and to be well-prepared for data taking in Run 4.

Part IV.

Appendix

A

Metrology station

The sensor dicing angle and bare module edge alignment are checked in a custom-made metrology station already introduced in Section 4.2 and shown in figure 4.2. The station uses a five mega-pixel camera mounted above a four-axis stage on which a PTFE jig fixates a 2S sensor or a bare module using vacuum. A laser-based distance measurement device is mounted next to the jig. The devices are operated with a custom LabView-based software environment. The measurement data is written to the hard drive as text files and then analysed and visualised with a dedicated Python script.

A.1. Software Architecture

As shown in Figure A.1 the developed software has a four-level architecture. The usage of several abstraction layers eases the maintainability and some parts can be processed simultaneously improving the performance of the measurement procedure. To avoid undefined hardware condition states the software is designed as a queued state machine (QSM) meaning that each task is defined as a certain machine state. The measurement program is executed by processing a list of machine states.

Starting from an input in the graphical user interface (GUI) a list of measurements steps is generated. Each measurement step has a certain type and a position. The main state of the QSM takes a measurement step and enqueues all necessary machine states, such as moving to a certain position or reading out a device. Some machine states can also enqueue other machine states on their own, e.g. the autofocus state calls the state to read out the camera and afterwards calls the motor movement state to move the stage up and down to acquire and image as sharp as possible. In this case the machine states are enqueued in front of the queue and not at the end. After completing the machine states of one measurement step the main state is called again to process the next measurement step. The results of a measurement step are pushed in a process queue.

Three different measurements are possible with the metrology station. The dicing angle is determined with images taken at several positions of the sensor edge (Mask distance). The bare module alignment can be determined with one of two different techniques using the laser-based distance measurement device (LScan or ZScan):

- **Mask distance**: As shown in Figure 4.3, within one image several distances between the aluminium fringe and dicing edge are determined with pattern recognition.
- **LScan**: The Line scan (LScan) method determines the sensor edge alignment by measuring the distance of the edge to the measurement device by focusing the laser spot on one edge and then moving it horizontally along the device. Doing this for the two sensor edges gives two data lists describing the orientation of each of the sensor edges to the measurement device. The Python analysis described in Appendix A.2 analyses the data to extract the bare module alignment information. This is the preferred baseline technique to evaluate the edge alignment because it is more precise and faster than the following method.

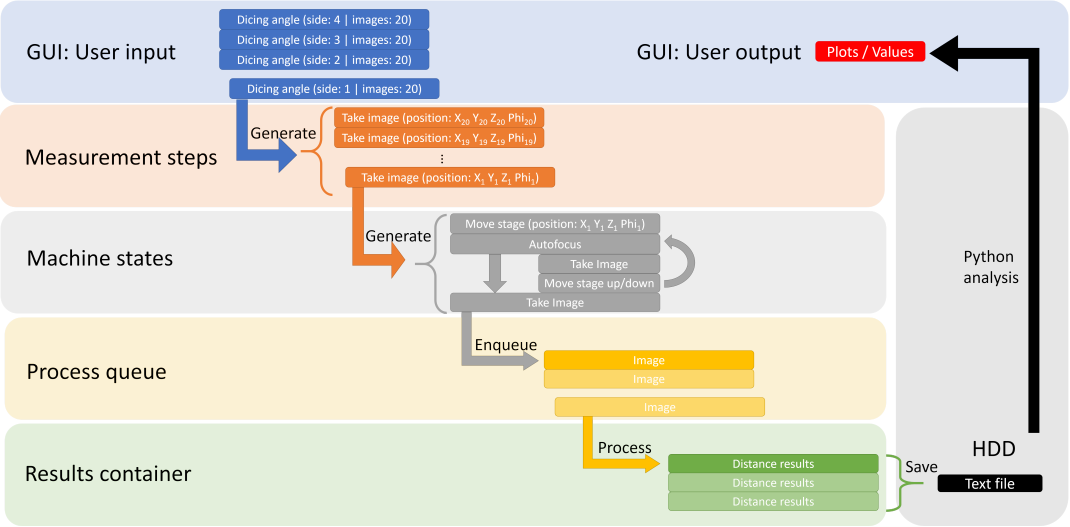

Figure A.1.: Structure of the custom-made LabView-based software environment for the metrology station.

- **ZScan**: The second measurement technique can be used to estimate the sensor bow within a bare module. By moving the bare module on multiple edge positions vertically along the measurement device the distance of both sensor edges to the measurement device can be extracted. The difference between the two edge distances again yields the distance between the two sensor edges. Having the multiple data points along one bare module side enables the calculation of the edge alignment as with the LScan but with less precision.

  In addition to this, each vertical measurement can be used to estimate the sensor bow within the bare module. While moving the module vertically the measurement device will not be focused on the sensor edge from the very beginning. The vertical positions at which the device starts or stops giving valid values can be used to estimate the vertical position of a silicon sensor. Having multiple measurements along a module side, the bow can be estimated, as shown in Figure A.2.

An independent loop in the software dequeues these results and processes the data such as measuring distances in images or handling the laser data. This way, the measurement can continue while the previously recorded data is processed. The results are stored in a container whose content is saved as a text file on the hard drive at the very end of the measurement program. Because it is rather inconvenient to further analyse the data with LabView, a Python script reads the result file and processes the data to perform the linear fits and create plots. For a convenient work flow the Python script can be started within the LabView software environment and the results are displayed in the graphical user interface.

For future improvements the data has to be uploaded into the measurement data-base, which requires some extensions in the current software and analysis.

A.2. Python Analysis

The Python script analyses the text files generated by the LabView software. For each result file a Module object is created. First the analysis scans through the data and extracts the number of measured module sides. For each side, a ModuleSide object is created. Within this

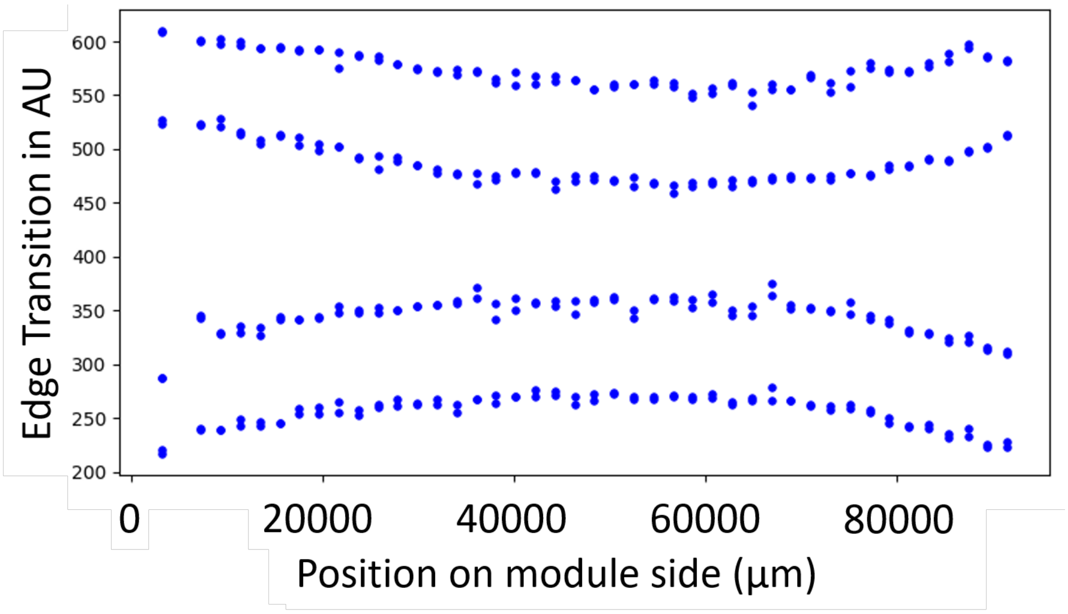

Figure A.2.: Bow measurement of a dummy bare module consisting of glass plates and aluminium bridges assembled at NISER India.

ModuleSide object measurement objects are stored, which are generated from the data file. There are three different measurement objects:

- **Distance Measurement**: Contains the values obtained by a distance measurement between the dicing edge and the aluminium fringe.
- **LScan**: Contains the distance values between the laser-based distance measurement device and a silicon sensor edge while it is moved horizontally among the device.
- **ZScan**: Contains the distance values between the laser-based distance measurement device and the bare module while it is moved vertically among the device.

With global settings stored in the script certain areas can be masked and the corresponding measurement points are ignored. This is necessary because at certain sensor edge positions the distance information retrieved from the laser measurement device is not trustworthy due to an impairment of the laser reflection by objects such as the module bridges. While the information of the distance measurement and LScan can be used directly for a the analysis of a ModuleSide, the ZScan object has to be analysed beforehand to extract the bow measurement points and relative sensor edge distances. The linear fit function of the ModuleSide object is used to extract the corresponding dicing angle or bare module alignment value. It uses an iterative fit method to exclude outliers. The values for this exclusion are also parameters.

The graphs are saved on the hard drive. In addition to this, a visualisation of the edge alignment is generated showing the position of the two sensors with respect to each other. An example of this output is shown in Figure A.3.

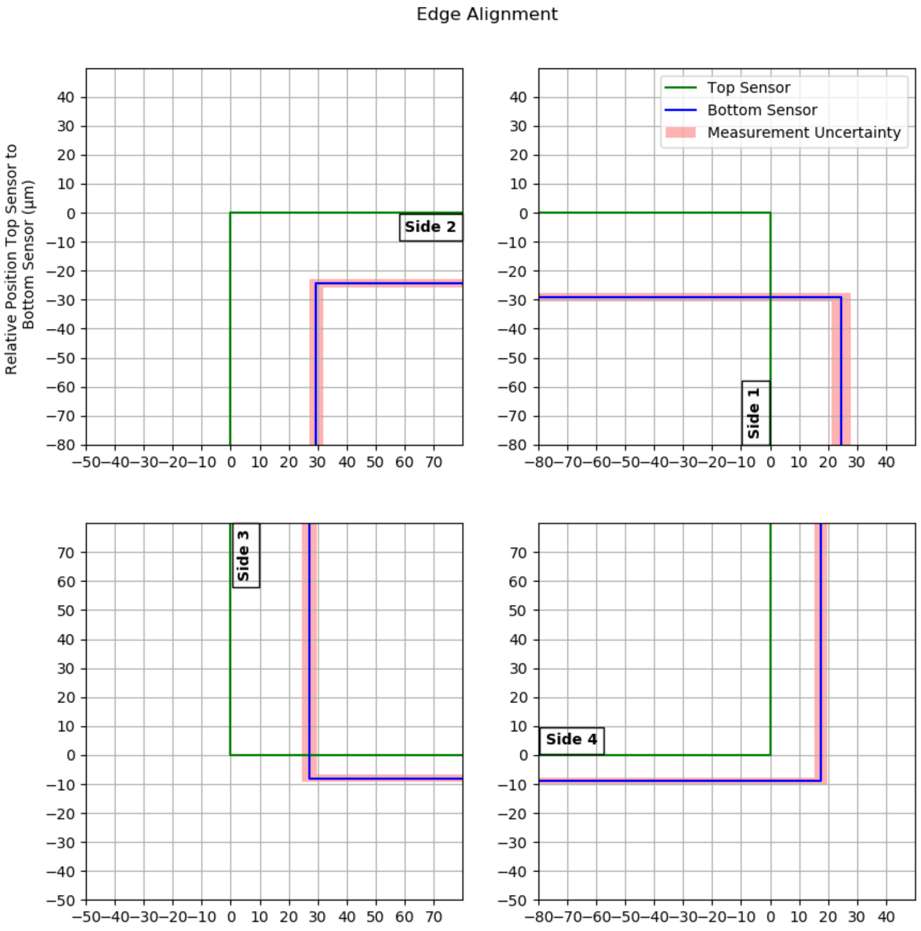

Figure A.3.: Visualisation of the edge alignment measurement of a dummy bare module consisting of glass plates and aluminium bridges assembled at NISER India.

B

Dispensing Gantry

The dispensing gantry was designed and programmed to apply glue and encapsulation material on components of 2S modules in a well-controlled way. With the volumetric dispenser fine lines of glue can applied on the backside of silicon sensors for the attachment of the polyimide isolation strips. The gantry is also used to apply the wire-bond encapsulation material on the readout wire-bond rows. Tne gantry was designed to handle four sensors or modules at once. It has a dispensing gun controlled by a volumetric dispenser mounted on an XYZ-gantry. The station is controlled by custom LabView-based software.

B.1. Alignment Procedure

Each time the cartridge containing the dispensing material is mounted in the dispensing gantry the position of the tip has to be aligned. This is necessary because the tip itself is screwed on the cartridge which is a hardly reproducible process, resulting in varying tip heights. In addition to this, the PTFE tips, used to apply the Polytec EP 601 LV, tend to be slightly bent, which results in offsets in the XY plane.

The alignment procedure is performed separately for the height Z and the XY position in the plane. The Z calibration is made with a forked light barrier. The barrier detects whether an object is in-between the fork disturbing the light barrier. The reproducibility is 7 µm. Because the XY position is not precisely known at this time the tip is moved forth and back through the light barrier. The procedure is shown in Figure B.1a. The tip is moved forth and back with decreasing heights until the light barrier is crossed. Once crossed, the step size is divided by two and the tip moves back and forth with increasing height until it stops crossing the light barrier. Afterwards the step size is again cut in half and the procedure is repeated until a step size of below 5 µm is reached.

Once the Z height of the tip is aligned it is moved downwards to the bottom of the forked light barrier. A camera is mounted behind the dispensing cartridge directed to the dispensing tip. As shown in Figure B.1b, four alignment marks are identified using a pattern recognition algorithm to determine the XY distance between the centre of gravity of the pattern and the very end of the tip. The determined offset is used to correct the position of the dispensing tip in the global coordinate system. The whole alignment procedure takes about two minutes.

B.2. Software Architecture

The software is designed as a queued state machine (QSM), similar to the metrology station as described in Appendix A. It is possible to program, save and load dispensing routines with the software. The routines are stored as text files on the hard drive. After a routine is written or loaded, the QSM generates machine states to process the dispensing routine. A dispensing routine contains the dispensing patterns of up to four modules or sensors. A dispensing pattern of such a module contains

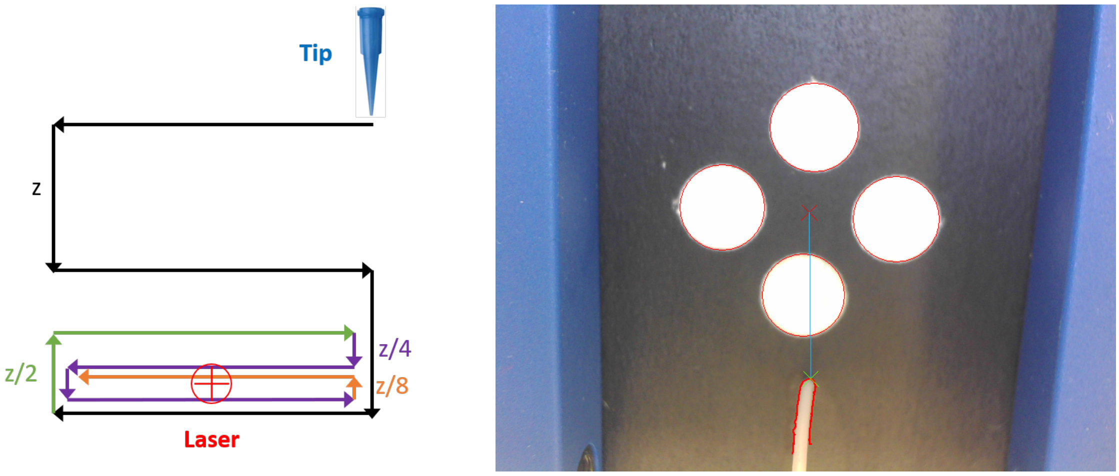

(a) Dispensing tip Z alignment using a forked light barrier, which is crossed by the dispensing tip.

(b) Dispensing tip XY alignment using pattern recognition by detecting the distance between the alignment marks and the tip.

Figure B.1.: Two-staged dispensing tip alignment procedure.

- The X,Y coordinate of the top left corner and the size of the module. The first one should be a well-adjustable reference point, such as the sensor corner. The position is given in the global coordinate system of the gantry.
- The absolute height of the object. This is the reference point for the tip height adjustment.
- A color to make the modules distinguishable on the GUI.
- A list of dispensing commands to apply dots or lines. Each command contains:
  - Relative X,Y coordinates within the module of the start of a dispensing line or a dot.
  - Relative X,Y coordinates within the module of the end of a dispensing line. If they are 0,0 a dot and not a line is applied.
  - The tip height Z during application relative to the module height.
  - The amount of glue to be applied in units of ml/mm for lines, ml for dots.
  - At the very end of dispensing a glue line, the material output can be stopped while the gantry finishes the line. This improves the homogeneity of the glue line.

The amount of glue to be applied in a glue line is controlled with the velocity of the gantry, because the volume flow is constant once the dispensing is activated. For dots the glue amount is controlled with the time period during which the dispensing is turned on.

B.3. Filling and Mounting of the Cartridge

B.3.1. Polytec EP 601 - LV

The epoxy resin Polytec EP 601 - LV is a low-viscosity, two-component resin which has to be mixed with a ratio of 100:35 (part A : part B). Because the glue components are hazardous, protective clothes and glasses should be worn. The pot life is 6 hours leaving the operator enough time for convenient dispensing. At least 3 g of glue should be prepared to be able to fill the cartridge with a reasonable amount of material. The glue mixing can be done manually with a scale precise enough to weigh 1 mg. The mixing of the glue should be done with proper illumination, e.g. below a lamp, because streaks are visible as long as the glue is not properly mixed. After two minutes of mixing the streaks should vanish and the glue can be filled in the cartridge. The cartridge can be mounted with a clamp to be able to fill the glue with a spatula into the 5 ccm large cartridge. Before filling a plug can be used to shut the dispensing opening of the cartridge preventing the glue to flow immediately out of it. After filling, the piston drop can be pushed carefully into the cartridge. It should not be pushed downwards immediately. To get rid of the excess air between the glue and the piston drop the cartridge can be turned over, resulting in the glue to flow towards the piston drop enabling the excess air to escape through the dispensing hole, by slowly pushing it upwards. During this step the cartridge should be covered by a sheet preventing any glue to splash out of the cartridge. After all excess air is pushed out, the dispensing tip can be mounted on the cartridge.

B.3.2. Sylgard 186

Sylgard 186 is a two-part silicone elastomere. The mixing ratio is 10:1 (part A : part B) and it has a pot life of 90 minutes. Figure B.2 shows a measurement of the time dependent viscosity of Sylgard mixtures relative to the initial viscosity right after the mixing. The relative viscosity is determined by measuring the material flow out of the cartridge at a constant pressure. With increasing viscosity the material flow decreases. The measurement shows that the viscosity increases by a factor of two within 60 minutes. Therefore, it should be used within 30 minutes to guarantee a reproducible application.

Once the parts are mixed the material can be poured into the cartridge. This should happen under a slight angle so the material does not entrap air at the bottom of the cartridge. If filled the plunge can be pushed in the cartridge. This will entrap an air bubble between plunge and encapsulation material. Therefore, the cartridge should be turned resulting that the air bubble slowly moves upwards towards the dispensing opening. This can be accelerated by carefully hitting the cartridge on the table. Once the air is removed the dispensing tip can be attached.

B.4. Glue Pattern

The dispensing pattern developed to attach the polyimide strips and the HV tail to the aluminium backside of 2S sensors for top sensors and bottom sensors is shown in Figure B.3 and Figure B.4. Table B.1 and Table B.2 contain the corresponding coordinates marked in the figures. Before material is applied on the sensor backsides a test line is placed besides the silicon sensor on the PTFE jig, comparable to a first test bond in a wire-bonding program. The precise application requires that the dispensing tip is completely filled with glue. In addition to this a tiny glue drop should stick at the very end of the tip. This way the glue has an immediate adhesion to the silicon back plane which is necessary to have an homogeneous glue line. For the long polyimide strips the amount of glue is 0.06 ml/mm. This is enough glue to completely wet the gluing joint without having excess on the strips' fringe. The amount of glue is controlled by the velocity of the gantry. The material flow is kept constant. By varying the velocity the amount of glue per line segment can be adjusted. At the very end of the line the dispensing is turned of and the dispensing tip moves to the end point. This stretches the last drop of glue, improving the homogeneity of the glue line. The pattern to glue the HV tails and the polyimide strip for the stump bridge consist of multiple dots having 0.1 ml of glue.

The height of the tip to the sensor backside should be about 50 ± 20 µm. This ensures immediate adhesion of the material once it is pushed out by the dispensing gun.

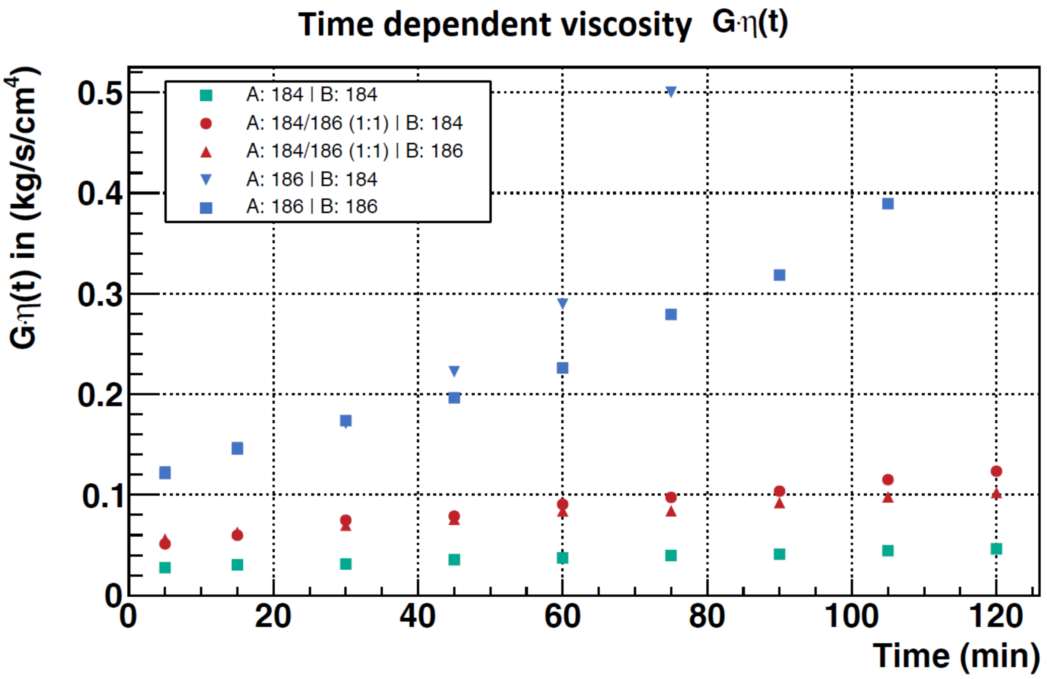

Figure B.2.: Viscosity measurement of wire-bond encapsulation material depending on time after mixing.

Table B.1.: Bottom sensor glue dispensing pattern.

Point	X (µm)	Y (µm)	Z (µm)
1	−10 000	5500	−1150
2	−10 000	100 000	−1150
3	5600	7500	45
4	5600	6000	45
5	5600	79 183	45
6	5600	88 183	45
7	51 300	88 183	45
8	51 300	86 250	45
9	51 300	8480	45
10	51 300	83 750	45
11	51 300	81 983	45
12	70 543	88 000	45
13	70 543	85 000	45
14	70 543	82 000	45
15	70 543	6000	45
16	97 200	87 183	45
17	97 200	15 000	45
18	97 200	6000	45

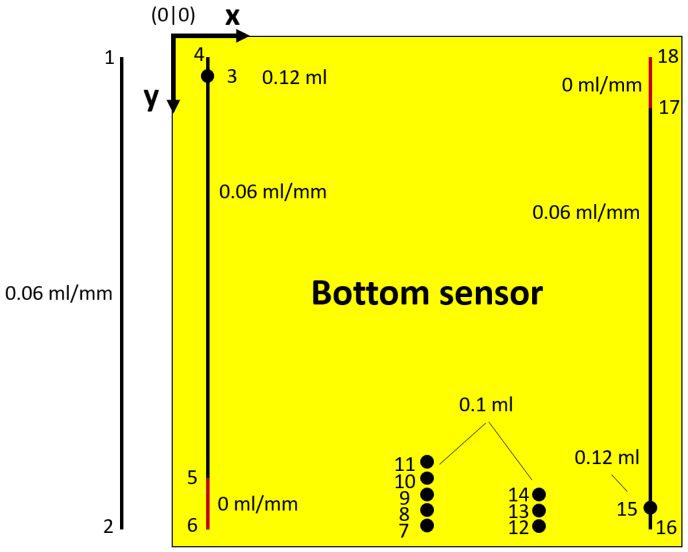

Figure B.3.: Bottom sensor dispensing pattern.

Table B.2.: Top sensor glue dispensing pattern.

Point	X (µm)	Y (µm)	Z (µm)
1	−10 000	5500	−1150
2	−10 000	10 0000	−1150
3	5600	7500	45
4	5600	6000	45
5	5600	79 183	45
6	5600	88 183	45
7	22 000	88 183	45
8	22 000	85 000	45
9	22 000	82 000	45
10	24 500	82 000	45
11	27 000	82 000	45
12	27 000	85 000	45
13	27 000	88 183	45
14	51 300	88 183	45
15	51 300	86 250	45
16	51 300	84 800	45
17	51 300	83 750	45
18	51 300	81 983	45
19	97 200	87 183	45
20	97 200	88 183	45
21	97 200	6000	45

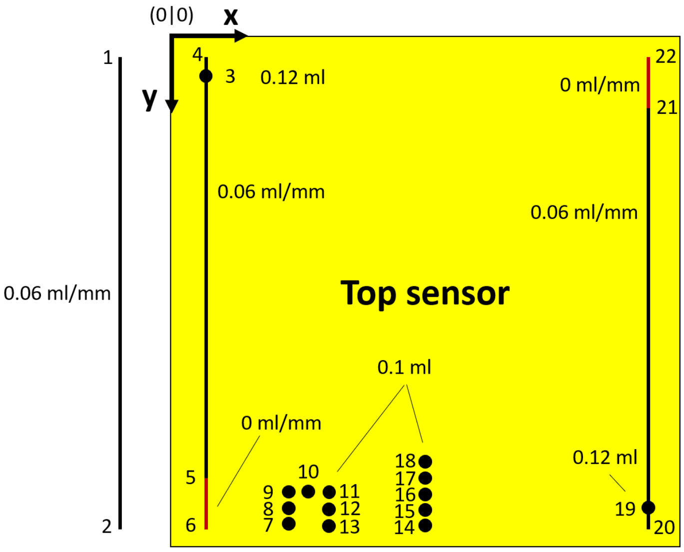

Figure B.4.: Top sensor dispensing pattern.

B.5. Wire-bond Encapsulation Pattern

The application of the wire-bond encapsulation material is done in three steps. The procedure is shown in Figure B.5. First the wire-bond feet are encapsulated using two lines of 2 ml/mm of silicone. The material needs about 5 to 10 minutes to completely flow between and beneath the wire-bonds. It then stops at the sensor edge or hybrid fold-over leaving the top of the wire-bond loop uncovered. For this, a third line of 3 ml/mm is applied. This line merges with the previous two, forming a homogeneous protection layer.

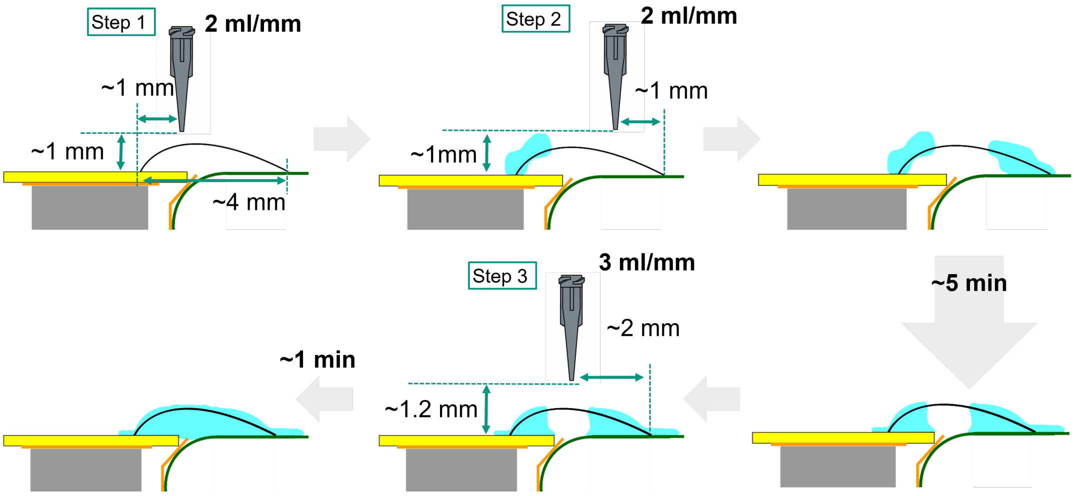

Figure B.5.: Wire-bond encapsulation procedure in three steps.

C

KARATE

C.1. Landau Distribution

The Landau distribution is an asymmetric probability density function describing the energy deposition of minimum ionizing particles in thin layers of matter. It peaks at its most probable value (MPV) and has a long upper tail resulting from a small fraction of individual collisions in which a comparatively large amount of energy is deposited. Therefore, its integral diverges and the determination of a mean value is not possible, unless an upper limit for the energy deposition is introduced.

The Landau distribution should have an MPV of 76 e$^-$/µm and a mean value of 108 e$^-$/µm to describe the energy deposition of minimum ionizing particles in silicon having an upper limit of 500 e$^-$/µm, as described in e.g. [Har17]. The model developed for the KARATE system uses the ROOT [Ant+09] libraries to generate random Landau-distributed signal values. The Landau distribution implemented in ROOT has two parameters: The MPV x_0 and a scaling factor σ_L. The probability density function is given as

$$p(x) = \frac{1}{\sigma_L}\Phi(\lambda) \quad \text{where} \quad \lambda = (x - x_0)/\sigma_L \tag{C.1}$$

and

$$\Phi(\lambda) = \frac{1}{2\pi i}\int_{c-i\infty}^{c+i\infty} e^{\lambda s + s\log s}\, ds. \tag{C.2}$$

While the MPV x_0 describes the position of the peak, σ_L affects the height and width of the distribution and thus the mean value, which is shown in Figure C.1. Having an upper limit the mean value is correlated to the scaling factor σ_L due to the asymmetric shape of the Landau distribution. Figure C.2 shows the mean values of a range of random numbers distributed according to a Landau distribution having 10^6 entries each with varying σ_L. The upper limit is 500 e$^-$/µm and the MPV is 76 e$^-$/µm. To get a distribution with a mean value of 108 e$^-$/µm the corresponding scaling factor is $\sigma_L = 10$.

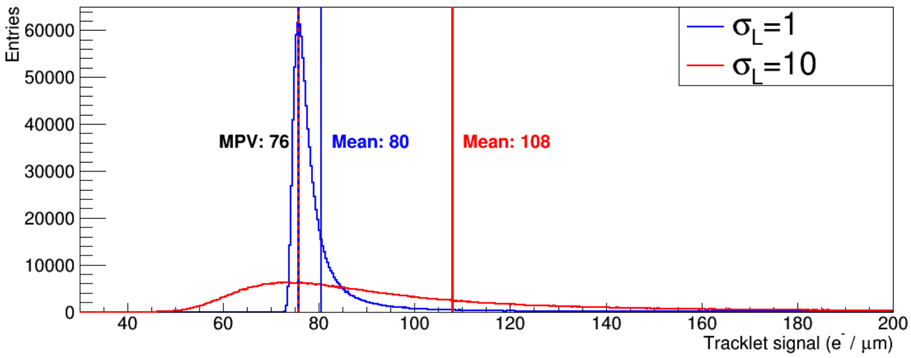

Figure C.1.: Landau distributions generated with ROOT with an MPV of 76 (vertical dotted blue and red line) and two scaling factors $\sigma_l = 1$ and $\sigma_l = 10$. The vertical blue and red lines indicate the mean value of the corresponding distribution. By decreasing the height and increasing the width the mean value shifts to higher values.

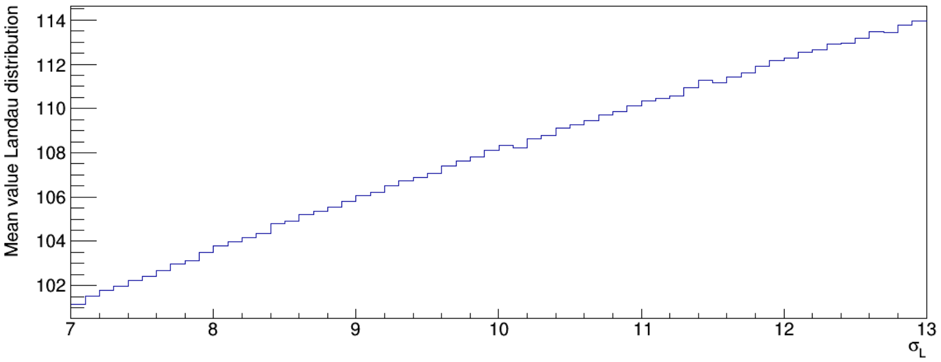

Figure C.2.: The mean values of Landau distributions with an MPV of 76 and varying σ_L. Due to the upper limit of 500 the mean value of each distribution can be determined and is correlated to σ_L. The distribution needed has a mean value of 108, which is achieved with $\sigma_L = 10$.

C.2. KARATE Settings File

The KARATE settings file contains all adjustable parameters of the KARATE system. Values which are also present in the Ph2_ACF hardware description file are overwritten by values from the KARATE settings file. It is split into two sections. The first input are observables. They determine what is displayed on the results plots. There are different types of results. Mostly used are observables (*observable*) which are single values that are displayed in graphs. In addition to this some observables can be related to single channels (*Cobservable*). Another type are the two-dimensional results which give a histogram of values for each measurement point (*TDobservable*). Statistical observables contain results accumulated over all measurement points (*Sobservable*).

The second section contains the variables. Two variables have three values $a; b; s$, which defined a measurement range from a to b with the step size s. All other values are fixed for all measurement runs. The measurement matrix is performed step by step by the KARATE data acquisition framework. An example settings file is given in the following:

```
KarateTriggers:                observable
Triggers:                      observable
KarateHits:                    observable
RecordedHits:                  observable
Efficiency:                    observable
KarateClusters:                observable
RecordedClusters:              observable
ClusterEfficiency:             observable
MeanClusterSize:               observable
MeanClusterSignal:             observable
KarateStubs:                   observable
Stubs:                         observable
StubEfficiency:                observable
ClusterStubEfficiency:         observable
Occupancy:                     observable
KarateOccupancy:               observable
NoiseHits:                     observable
NoiseHitsOccupancy:            observable
FakeHits:                      observable
FakeHitsOccupancy:             observable
Losses:                        observable
LossesProbability:             observable
DippedLosses:                  observable
DippedLossesProbability:       observable
TriggerDistribution:           Sobservable
NoiseHitDistance:              Sobservable
StubDistribution:              Sobservable
KarateStubDistribution:        Sobservable
HitDistribution:               Sobservable
NoiseHitsPerChannel:           Cobservable
FakeHitsPerChannel:            Cobservable
LossesPerChannel:              Cobservable
DippedLossesPerChannel:        Cobservable
ChannelEfficiency:             Cobservable
LossesProbPC:                  Cobservable
DippedLossesProbPC:            Cobservable
NoiseHitsOccPC:                Cobservable
FakeHitsOccPC:                 Cobservable
ClusterSize:                   TDobservable
Bend:                          TDobservable
```

```
PulseHeights:                TDobservable
ClusterPulseHeights:         TDobservable
TriggerDistributionTD:       TDobservable
NoiseHitDistanceTD:          TDobservable
HitDistributionTD:           TDobservable
StubDistributionTD:          TDobservable
KarateStubDistributionTD:    TDobservable
Pause:                       0
Repetitions:                 1
Voltage:                     1.8
Latency:                     60
DLL:                         8
ListLength:                  40000
Debug:                       0
Iterations:                  10
TriggerWidth:                6
MTSTracks:                   50;60;1
PatternMode:                 3
VCTH:                        530;570;20
StartEmptyHitPattern:        1
RangeEmptyHitPattern:        0
TrackDensity:                10
Angle:                       0
AngleSigma:                  1
Signal:                      76
SignalSigma:                 10
Power:                       5
StubClusterWidth:            4
StubPtWidth:                 14
StubLayerSwap:               0
StubOffset1:                 0
StubOffset2:                 0
StubOffset3:                 0
StubOffset4:                 0
#
Comment section
```

C.3. KARATE Emitter FC7 Firmware

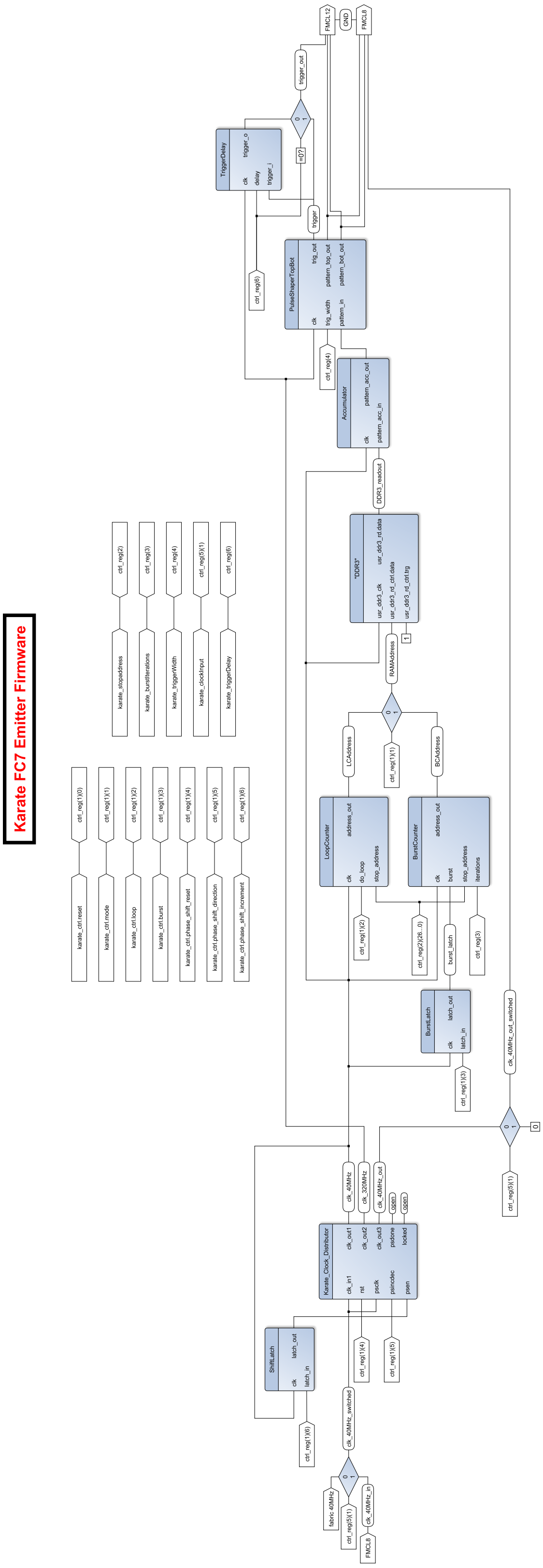

Figure C.3.: Detailed schematic of the KARATE firmware.

List of Figures

List of Tables

Bibliography

[AAC10] A. Affolder, P. Allport, and G. Casse. *Charge collection efficiencies of planar silicon detectors after reactor neutron and proton doses up to 1.6×1016neqcm-2.* In: Nuclear Instruments and Methods in Physics Research Section A: Accelerators, Spectrometers, Detectors and Associated Equipment 612.3 (2010), pp. 470–473. ISSN: 0168-9002. DOI: `10.1016/j.nima.2009.08.005` (cited on p. 87).

[Ada+17] W. Adam et al. *P-Type Silicon Strip Sensors for the new CMS Tracker at HL-LHC.* In: Journal of Instrumentation 12.06 (2017), P06018–P06018. DOI: `10.1088/1748-0221/12/06/p06018` (cited on p. 16).

[Agg+17] R. Aggleton et al. *An FPGA based track finder for the L1 trigger of the CMS experiment at the High Luminosity LHC.* In: Journal of Instrumentation 12.12 (Dec. 2017), P12019–P12019. DOI: `10.1088/1748-0221/12/12/P12019` (cited on p. 14).

[Ago+03] S. Agostinelli et al. *Geant4—a simulation toolkit.* In: Nuclear Instruments and Methods in Physics Research Section A: Accelerators, Spectrometers, Detectors and Associated Equipment 506.3 (2003), pp. 250–303. ISSN: 0168-9002. DOI: `10.1016/S0168-9002(03)01368-8` (cited on p. 88).

[Ant+09] I. Antcheva et al. *ROOT — A C++ framework for petabyte data storage, statistical analysis and visualization.* In: Computer Physics Communications 180.12 (2009). 40 YEARS OF CPC: A celebratory issue focused on quality software for high performance, grid and novel computing architectures, pp. 2499–2512. ISSN: 0010-4655. DOI: `10.1016/j.cpc.2009.08.005` (cited on p. 109).

[Apo+17] G. Apollinari et al. *High Luminosity Large Hadron Collider HL-LHC.* Tech. rep. CERN, May 24, 2017. DOI: `10.5170/CERN-2015-005.1` (cited on p. 13).

[ATL12] ATLAS Collaboration. *Observation of a new particle in the search for the Standard Model Higgs boson with the ATLAS detector at the LHC.* In: Physics Letters B 716.1 (Sept. 2012), pp. 1–29. DOI: `10.1016/j.physletb.2012.08.020` (cited on p. 3).

[Axe19] M. Axer. *Development of a test system for the quality assurance of silicon microstrip detectors for the inner tracking system of the CMS experiment.* In: (Oct. 2019) (cited on p. 7).

[Bol+03] G. Bolla et al. *Wire-bonds failures Induced by resonant vibrations in the CDF silicon detector.* In: vol. 3. Nov. 2003, 1641–1645 Vol.3. ISBN: 0-7803-8257-9. DOI: `10.1109/NSSMIC.2003.1352193` (cited on p. 38).

[Cap+18] L. Caponetto et al. *CIC1 technical specification.* Tech. rep. CERN, 2018. URL: `https://espace.cern.ch/Tracker-Upgrade/Electronics/CIC/default.aspx` (cited on p. 22).

[CER17] CERN. *LHC Guide.* 2017. URL: `http://cds.cern.ch/record/2255762` (cited on p. 5).

[CER18] CERN. *Accelerator Performance and Statistics.* Oct. 1, 2018. URL: `http://acc-stats.web.cern.ch/acc-stats/#lhc/` (cited on p. 6).

[CER19] CERN. *The HL-LHC project.* June 16, 2019. URL: `https://hilumilhcds.web.cern.ch/about/hl-lhc-project` (cited on pp. 13, 14).

[Cha+10] M. Chan et al. *Updated Studies of the CMS Tracker at High Trigger Rate*. Tech. rep. CMS-NOTE-2010-011. Geneva: CERN, Apr. 2010. URL: `http://cds.cern.ch/record/1278159` (cited on p. 75).

[CMS08] CMS Collaboration. *The CMS experiment at the CERN LHC*. In: Journal of Instrumentation 3.08 (Aug. 14, 2008), S08004–S08004. DOI: `10.1088/1748-0221/3/08/S08004` (cited on pp. 7–9).

[CMS12a] CMS Collaboration. *CMS Technical Design Report for the Pixel Detector Upgrade*. Tech. rep. CERN-LHCC-2012-016. CMS-TDR-11. CERN, 2012. URL: `https://cds.cern.ch/record/1481838` (cited on p. 8).

[CMS12b] CMS Collaboration. *Observation of a new boson at a mass of 125 GeV with the CMS experiment at the LHC*. In: Physics Letters B 716.1 (2012), pp. 30–61. DOI: `10.1016/j.physletb.2012.08.021` (cited on p. 3).

[CMS17a] CMS Collaboration. *Particle-flow reconstruction and global event description with the CMS detector*. In: Journal of Instrumentation 12.10 (Oct. 2017), P10003–P10003. DOI: `10.1088/1748-0221/12/10/P10003` (cited on p. 9).

[CMS17b] CMS Collaboration. *The CMS trigger system*. In: Journal of Instrumentation 12.01 (2017), P01020. DOI: `10.1088/1748-0221/12/01/p01020` (cited on p. 10).

[CMS17c] CMS Collaboration. *The Phase-2 Upgrade of the CMS L1 Trigger Interim Technical Design Report*. Tech. rep. CERN-LHCC-2017-013. CMS-TDR-017. Geneva: CERN, 2017. URL: `https://cds.cern.ch/record/2283192` (cited on pp. 3, 14).

[CMS18] CMS Collaboration. *The Phase-2 Upgrade of the CMS Tracker*. Tech. rep. CERN-LHCC-2017-009. CMS-TDR-014. CERN, Apr. 16, 2018. URL: `https://cds.cern.ch/record/2272264` (cited on pp. 13, 15–17, 19, 21, 22, 24, 53, 54).

[CMS19a] CMS. *CMS Tracker Phase2 Acquisition & Control Framework*. Oct. 2019. URL: `https://gitlab.cern.ch/cms_tk_ph2/Ph2_ACF` (cited on pp. 45, 58).

[CMS19b] CMS Collaboration. *People statistics*. June 16, 2019. URL: `http://cms.cern/collaboration/people-statistics` (cited on p. 7).

[CMS19c] CMS Collaboration. *Public CMS Luminosity Information*. June 16, 2019. URL: `https://twiki.cern.ch/twiki/bin/view/CMSPublic/LumiPublicResults` (cited on p. 6).

[CMS97a] CMS Collaboration. *The CMS hadron calorimeter project: Technical Design Report*. Tech. rep. 1997. URL: `http://cds.cern.ch/record/357153` (cited on p. 9).

[CMS97b] CMS Collaboration. *The CMS muon project: Technical Design Report*. Tech. rep. Geneva, 1997. URL: `http://cds.cern.ch/record/343814` (cited on p. 9).

[Col19a] C. Collaboration. *CMS Software - CMSSW*. Oct. 2019. URL: `https://cms-sw.github.io/` (cited on p. 88).

[Col19b] I. College. *CBC3.1 User Manual v.4*. Oct. 2019. URL: `http://www.hep.ph.ic.ac.uk/ASIC/cbc3.1/CBC3p1_User_Manual_V1p4.pdf` (cited on p. 19).

[Col97] C. Collaboration. *The CMS electromagnetic calorimeter project: Technical Design Report*. Technical Design Report CMS. Geneva: CERN, 1997. URL: `http://cds.cern.ch/record/349375` (cited on p. 8).

[Con+15] D. Contardo et al. *Technical Proposal for the Phase-II Upgrade of the CMS Detector*. Tech. rep. CERN-LHCC-2015-010. LHCC-P-008. CMS-TDR-15-02. Geneva: CERN, 2015. URL: `https://cds.cern.ch/record/2020886` (cited on p. 15).

[Cor19] D. Corning. *Datasheet Sylgard 186*. Sep. 2019. URL: `https://www.dow.com/documents/en-us/productdatasheet/11/11-12/11-1253-sylgard-186-silicone-elastomer.pdf?iframe=true` (cited on pp. 32, 38).

[Dav16] S. R. Davis. *Interactive Slice of the CMS detector*. In: (2016). URL: `https://cds.cern.ch/record/2205172` (cited on p. 10).

[Dee17] N. Deelen. *Calibration of a minimodule*. Phase 2 Outer Tracker System Test and DAQ Meeting during Phase2 Days. Mar. 2017. URL: `https://indico.cern.ch/event/614309` (cited on p. 47).

[Deu19] Deutsches Elektronen-Synchrotron DESY. *Test Beams at DESY*. 2019. URL: `http://testbeam.desy.de` (visited on 09/09/2018) (cited on p. 55).

[EB08] L. Evans and P. Bryant. *LHC Machine*. In: Journal of Instrumentation 3.08 (2008), S08001–S08001. DOI: `10.1088/1748-0221/3/08/s08001` (cited on pp. 5, 6).

[Eng19] Engineering Department (CERN). *Beam lines at PS and SPS*. 2019. URL: `http://sba.web.cern.ch/sba/BeamsAndAreas/ExpList.asp` (cited on p. 55).

[Fel+18] L. Feld et al. *Service Hybrids for the Silicon Strip Modules of the CMS Phase-2 Outer Tracker Upgrade*. Tech. rep. CMS-CR-2018-271. Geneva: CERN, Oct. 2018. URL: `http://cds.cern.ch/record/2644448` (cited on p. 19).

[Fer19] Fermilab Test Beam Facility. *Beam Overview*. 2019. URL: `http://ftbf.fnal.gov/beam-overview/` (visited on 09/21/2018) (cited on p. 55).

[Fib19] I. Fiberoptics. *Datasheet LED IFD99B*. Sep. 2019. URL: `https://i-fiberoptics.com/pdf/if-e99bdatasheet.pdf` (cited on p. 56).

[Gad+18] T. Gadek et al. *Front-end hybrids for the strip-strip modules of the CMS Outer Tracker Upgrade*. Tech. rep. CMS-CR-2018-295. Geneva: CERN, Oct. 2018. URL: `https://cds.cern.ch/record/2658201` (cited on p. 19).

[Ham19] Hamamatsu. *Stealth Dicing Process vs. Ordinary Dicing Methods*. Sep. 2019. URL: `https://sd.hamamatsu.com/jp/en/SD_outline/SD_comparison.html` (cited on p. 27).

[Har17] F. Hartmann. *Evolution of Silicon Sensor Technology in Particle Physics*. 2nd ed. Springer, Nov. 3, 2017. ISBN: 978-3-319-64434-9. DOI: `10.1007/978-3-319-64436-3` (cited on pp. 18, 66, 71, 109).

[HM06] W. Herr and B. Muratori. *Concept of luminosity*. In: (2006). DOI: `10.5170/CERN-2006-002.361` (cited on p. 6).

[Kar+97] V. Karimäki et al. *The CMS tracker system project: Technical Design Report*. Technical Design Report CMS. Geneva: CERN, 1997. URL: `http://cds.cern.ch/record/368412` (cited on p. 8).

[Kop18] R. Koppenhöfer. *Conception and validation of test stations to electrically qualify silicon strip modules for the CMS Phase II Upgrade*. Master's thesis. Karlsruhe Institute fof Technology - Institute of Experimental Particle Physics, 2018 (cited on p. 42).

[Mal18] P. K. Mal. *Effect of Pile-Up events on Strip Tracker*. Aug 2018. URL: `https://indico.cern.ch/event/744852/contributions/3113776/attachments/1704570/2746181/IndiaCMSMeeting_Aug242018.pdf` (cited on p. 74).

[Mob16] E. Mobs. *The CERN accelerator complex. Complexe des accélérateurs du CERN*. July 8, 2016. URL: `http://cds.cern.ch/record/2197559/files/?docname=CCC-v2017&version=all&ln=de` (cited on p. 6).

[Mol99] M. Moll. *Radiation damage in silicon particle detectors: Microscopic defects and macroscopic properties*. Ph.D. Thesis (Advisor: G. Lindstrom); Universität Hamburg, Diss., 1999. Dr. Universität Hamburg, 1999, p. 251. URL: `http://bib-pubdb1.desy.de/record/300958` (cited on p. 19).

[Nod+18] B. Nodari et al. *A 65 nm Data Concentration ASIC for the CMS Outer Tracker Detector Upgrade at HL-LHC*. Tech. rep. CMS-CR-2018-278. Geneva: CERN, Oct. 2018. URL: `https://cds.cern.ch/record/2650712` (cited on pp. 19, 22).

[Pes+15] M. Pesaresi et al. *The FC7 AMC for generic DAQ & control applications in CMS*. In: JINST 10.03 (2015), p. C03036. DOI: `10.1088/1748-0221/10/03/C03036` (cited on p. 45).

[Pes+19] M. Pesaresi et al. *The FC7 Project*. Sep. 2019. URL: `https://espace.cern.ch/project-FC7/SitePages/Home.aspx` (cited on p. 61).

[PH10] M. Pesaresi and G. Hall. *Simulating the performance of a p_T tracking trigger for CMS*. In: Journal of Instrumentation 5.08 (2010), pp. C08003–C08003. DOI: `10.1088/1748-0221/5/08/c08003` (cited on p. 16).

[Pol19a] Polytec. *Datasheet Polytec EP 601*. Sep. 2019. URL: `https://www.polytec-pt.com/fileadmin/user_uploads_Polytec-PT/home/documents/Polytec_Klebstoffe_DEU/Polytec_EP_601_D.pdf` (cited on p. 30).

[Pol19b] Polytec. *Datasheet Polytec TC 437*. Sep. 2019. URL: `https://www.polytec-pt.com/fileadmin/user_uploads_Polytec-PT/home/documents/Polytec_Klebstoffe_ENG/Polytec_TC_437_engl.pdf` (cited on p. 34).

[Pry19] M. Prydderch. *CBC3.1User Manual*. Ed. by I. College. Oct. 2019. URL: `http://www.hep.ph.ic.ac.uk/ASIC/cbc3.1/CBC3p1_User_Manual_V1p4.pdf` (cited on pp. 66, 80).

[Sei19] S. Seif-El-Nasr Storey. *Conversion factor VCth to electrons*. personal communication. Oct. 6, 2019 (cited on p. 62).

[Tau+10] A. Taurok et al. *The Central Trigger Control System of the CMS Experiment at CERN*. Tech. rep. CMS-NOTE-2010-017. Geneva: CERN, May 2010. URL: `https://cds.cern.ch/record/1319359` (cited on p. 79).

[Tea18] T. L. Team. *LpGBT Specifications*. Ed. by P. Moreira. 2018. URL: `https://espace.cern.ch/GBT-Project/LpGBT/Specifications/LpGbtxSpecifications.pdf` (cited on p. 22).

[Tho19] Thorlabs. *Datasheed Photodiode FDS015*. Sep. 2019. URL: `https://www.thorlabs.com/drawings/f077f2137053eb98-76AD6468-9DD1-1B13-31CBE1C9959FAA59/FDS015-SpecSheet.pdf` (cited on p. 57).

[Tro+17] J. Troska et al. *The VTRx+, an optical link module for data transmission at HL-LHC*. In: PoS TWEPP-17 (2017), 048. 5 p. DOI: `10.22323/1.313.0048` (cited on p. 22).

[Uch+18] K. Uchida et al. *The CBC3 readout ASIC for CMS 2S-modules*. Tech. rep. CMS-CR-2018-017. Geneva: CERN, 2018. URL: `https://cds.cern.ch/record/2312215` (cited on pp. 19–21).

[Upl19] L. Uplegger. *FNAL TestBeam Analysis of Full Irradiated CBC3-2 Minimodule*. 2019. URL: `https://indico.cern.ch/event/807298/contributions/3359843/attachments/1816077/2968191/2019March21_Nabin_FNAL_TestBeam_Irr.pdf` (cited on pp. 69, 72, 73, 81).

[Zie19] J. F. Ziegler. *SRIM - The Stopping and Range of Ions in Matter*. 2019. URL: `http://www.srim.org/` (cited on p. 39).

Acknowledgments – Danksagung

Abschließend möchte ich all denjenigen danken, die mich während der Promotion unterstützt haben.

Zuerst möchte ich Herrn Prof. Dr. Ulrich Husemann für die Betreuung meiner Promotion und jeglichen Rat danken. Prof. Dr. Thomas Müller danke ich für die Übernahme des Korreferats und der Möglichkeit am ETP zu promovieren.

Der Landesgraduiertenförderung des Landes Baden-Württemberg und der Karlsruhe School of Elementary Particle and Astroparticle Physics: Science and Technology (KSETA) möchte ich für die Unterstützung während der Promotion danken.

Dr. Alexander Dierlamm danke ich für die exzellente Betreuung in allen Belangen. Dies beinhaltet die vielen fachlichen Diskussionen und Vorschläge sowie das Korrekturlesen der Dissertation.

Dr. Andreas Nürnberg danke ich für jeden hilfreichen Tipp sowie das sorgfältige Korrekturlesen der Dissertation.

Felix Bögelspacher, Anita Weddigen, Pia Steck und Marius Neufeld danke ich für die (elektro-)technische Unterstützung. Hervorzuheben ist die Zusammenarbeit mit Tobias Barvich. Vielen Dank für alle technischen Tipps, Anregungen und Hilfen innerhalb der letzten drei Jahre.

Roland Koppenhöfer, Jan-Ole Gosewisch, Gregor Vollmer, Dr. Simon Kudella, Dr. Daniel Schell und Marius Metzler - also allen Zugehörigen des Competence Rooms - danke ich für die geniale Arbeitsatmosphäre in unserem Büro.

Zuletzt möchte ich meinen Eltern Gabi und Wolfgang Maier danken. Ohne ihre Unterstützung wäre das Studium und die anschließende Promotion nicht möglich gewesen.

Declaration

I declare that the work in this dissertation was carried out in accordance with the requirements of the University's Regulations and that it has not been submitted for any other academic award. Except where indicated by specific reference in the text, the work is the candidate's own work. Work done in collaboration with, or with the assistance of, others is indicated as such.

Karlsruhe, November 2019

Stefan Maier